Cavity QED with Multilevel Atoms: Generation of Nonclassical States

Caspar Groiseau

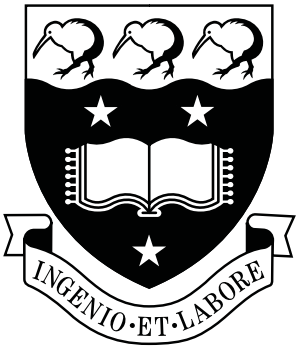

A thesis submitted in fulfilment of the requirements
for the degree of Doctor of Philosophy in Physics

Main supervisor: Assoc. Prof. Scott Parkins
Co-supervisor: Prof. Howard Carmichael

The University of Auckland
2021

Part I

Front Matter

Abstract

The currently ongoing dawn of quantum technologies, such as quantum information and quantum metrology, leaves some to speak of a quantum revolution. The development of the required physical "hardware" goes hand-in-hand with quantum state engineering, i.e., the design of quantum protocols that prepare the quantum states required as resources for these technologies. Concentrated efforts have produced a plethora of potential schemes for this purpose. However, trying to improve on and optimise these is vital and thus a main drive of the field. The topic of this thesis is precisely that, the search for novel generation schemes that are potentially easier, more high yield or more "quantum". Common issues within this topic are the susceptibility of these states to fall victim to decoherence, and the probabilistic nature of certain techniques. The "hardware" considered here are cavity quantum electrodynamics systems, i.e., optical cavities in which atom-light interactions are enhanced. The parameter regimes made accessible by state-of-the-art optical cavities open up new roads for investigations when it comes to protocols, and a variety of them are therefore considered here. A central aspect of this thesis is also further inspection of the recently experimentally-implemented Dicke model in integer-spin atoms. Even though it is one of the fundamental models of quantum optics, it does not arise naturally and can thus only be studied in engineered systems like this one. The quantum states we target to engineer within this thesis are, firstly, light pulses containing Fock states, $0N$-states, binomial-code-states, and Greenberger-Horne-Zeilinger states. Additionally, we also aim to produce two-mode (or two-colour) light with quantum-correlated photon statistics. Secondly, in ensembles of atoms, we propose to create entangled spin states such as Schrödinger's cat states and Dicke states. Among these, the states of light

would mainly find application and lead to further developments in quantum information, while the atomic states would find a use in quantum metrology.

Acknowledgements

First and foremost, I would like to thank my supervisor Scott Parkins for giving me the opportunity to join his team here in Auckland and for his guidance at all stages of the PhD. This certainly allowed me to deepen my understanding Quantum Optics and grow as a scientist.
In the same vein, I would like to thank the Dodd-Walls Centre for Photonic and Quantum Technologies for making this possible by sponsoring me and letting me be part of the wider New Zealand Optics community.
I would also like to thank the people who helped me tread my path in physics without which I would not be here today, such as Luis Roa Oppliger for introducing me to Quantum Optics and Information, and Sandro Wimberger for being a valuable mentor for many years now. Similarly, I also thank Messieurs Clément, Harms et Moudat from the FG Berlin for giving me the motivation to pursue sciences.
I would like to thank the Theoretical Quantum Optics group as a whole for maintaining such a pleasant working environment. Special thanks go out to Nikki (and by extension Peter) for taking me on all these amazing hikes, to Stuart for aiding me getting started on the project and to Alex for helping me a great deal to get a better understanding of Quantum Tomography.
A great many thanks go to Adrián Ortiz Cervantes for all the meals and discussions that we have shared over the last couple of years. I am also very grateful for being able to go through the PhD experience with the other Janis: Ayomikun, Mohammad, Nicola, Qaisar, Santhosh and Sina who, with their banter, made sure that our office never got too quiet.
I would also like to thank the University of Auckland Maths club (Polygon), especially Ben, Brendan and Phelisia for all the board game sessions that gave me something to look forward to at the end of each week.
I also thank Peter Reimitz for proofreading parts of my thesis.
Finally, I thank Reni and Olsen for always believing in me.

This work makes use of the Quantum Toolbox in Python (QuTiP) [1, 2].
I also acknowledge the contribution of NeSI high-performance computing facilities to the results of this research. New Zealand's national facilities are provided by the New Zealand eScience Infrastructure and funded jointly by NeSI's collaborator institutions and through the Ministry of Business, Innovation and Employment's Research Infrastructure program.

Contents

Chapter 1

Introduction

In this thesis, we would like to explore two main themes with very different aims, but which nevertheless are complementary to each other:

The first theme is **Single- or few-atom cavity quantum electrodynamics systems for production of nonclassical light**: Recent experiments with trapped atoms and fibre-integrated, optical micro- and nanocavities have pushed the field of cavity quantum electrodynamics (cavity QED) into a new realm of single-atom–photon coupling strengths, corresponding to unprecedentedly large single-atom cooperativities [3–8], while also offering the possibility of integrated quantum networks for quantum communication or simulation of quantum many-body systems [9–15]. A further, well-known capability provided by such large coupling strength is the generation of single photons with high fidelity through cavity-enhanced atomic spontaneous emission. Efficient single-photon sources are central to many efforts to realise optical quantum computation and communication. Some interdisciplinary applications are also on the horizon as recently their distinctive quantumness (photon statistics) has led to their use in studies of quantum biology, e.g., for biological photoreceptors such as those in the retina [16–19]. Beyond this, there is the even greater, and still outstanding challenge to realise an equally efficient source of pulses of *exactly* N (≥ 2) optical photons. Highly nonclassical states of light such as these are of fundamental interest to quantum optics and represent a starting point for the engineering of yet more complex quantum states.

They are also essential for new, more resource-efficient photonic architectures for universal quantum computation and quantum error correction using individual, higher-dimensional systems [20–22] (*cf.* multiple two-state systems), as well as for optimal capacity of a quantum communication channel [23, 24], and Heisenberg-limited interferometry [25–31].

The second theme is **Many-body quantum dynamics with spin-F atoms in cavities**. Bose-Einstein condensates of ultracold atoms with an internal spin degree of freedom are a useful tool to investigate many-body quantum dynamics. Recent experiments have realised Bose-Einstein condensates in which all magnetic sublevels of a hyperfine state are condensed [32, 33]. The tunability of these systems is limited, since some parameters are fixed by the choice of the atomic species. In such systems, the dynamics are governed by spin collisions and magnetic field shifts. The small energy scales herein lead to long time scales for the dynamics. We emulate and extend these spin dynamics of Bose-Einstein condensates with an engineered cavity QED system, in which we have more flexibility with regard to choosing the values of the parameters and typical time scales that are orders of magnitude faster. Another important difference is that the system is now an open system, i.e., photons are leaving the system, and that we can monitor this escaping light field via a variety of measurements. Indeed, there has been a growing experimental interest in cavity QED-mediated interactions of spin-F atoms, atoms that in contrast to most studies in the field have a spin $F > \frac{1}{2}$, in recent times [34, 35]. This could be used to study quantum phase transitions [36, 37], but here we shall look at producing exotic spin states, of potential use in quantum metrology or in quantum information. The reason for this is that these spin states display multipartite entanglement and can offer quantum-enhanced precision [38].

This thesis is organised as follows:

Chapter 2 aims to give the basic tools needed for the description of open quantum systems. We start with some basics such as the quantum harmonic oscillator and its number state representation. We introduce the two main ways to simulate open quantum systems: the master equation and quantum trajectories. Finally, we explain quantum regression, which is crucial for the computation of correlation functions.

A major part of the research in the fields of atomic and optical physics arguably concentrates on the alkali atoms because of their relative simplicity and their relatively high mass, which makes them easier to cool and thereby to use in experiments. Similarly, in this thesis, we mostly employ Rubidium (^{87}Rb) and Caesium (^{133}Cs) as atomic species. Therefore we shall give a brief description of their main optical properties in Chapter 3, such as their energy level structure and their interaction with electromagnetic fields.

In Chapter 4 we give an introduction to cavity quantum electrodynamics. We start with the quantisation of the electromagnetic field, followed by an introduction to optical cavities. Then we treat the interaction of light in said cavities with the environment and atoms. Finally we discuss basic photon statistics.

In Chapter 5 we shall setup the derivations of the engineered Dicke model for integer spin systems that will be the basis for Chapters 7 and 10. The chapter also contains an extension for including spontaneous emission and the engineering of spin collision dynamics.

Chapter 6 is about the various methods that will be used to perform quantum state tomography, i.e., the reconstruction of the quantum state of a light pulse that will be used extensively in the Chapters 7 and 8, which are part of the first theme and focus on the generation of exotic optical quantum states.

In Chapter 7 we propose a single-atom, cavity quantum electrodynamics system, compatible with recently demonstrated, fibre-integrated micro- and nano-cavity setups, for the on-demand production of optical number-state, $0N$-state, and binomial-code-state pulses. The scheme makes use of Raman transitions within an entire atomic ground-state hyperfine level and operates with laser and cavity fields detuned from the atomic transition by much more than the excited-state hyperfine splitting. This enables reduction of the dynamics to that of a simple, cavity-damped Tavis-Cummings model with the collective spin determined by the total angular momentum of the ground hyperfine level.

In Chapter 8 we extend Chapter 7 to resonance, which allows us to consider a wider range of optical cavities. The possibilities offered remain much the same, but now they also feature the generation of entangled photonic states.

In Chapter 9 we explore a novel variation of the one-atom laser made possible by state-of-the-art nanofibre cavities, which allow for the simultaneous strong coupling of the atom to two cavity modes. The output light of the system shows, on top of sub-Poissonian photon statistics and antibunching of the individual modes, a series of other quantum signatures in the correlations between the two modes.

In Chapter 10 we examine trajectories of collective atomic spin states of an effective Dicke model. When the strengths of the co-rotating and counter-rotating couplings are set to be equal to each other we obtain one-axis twisting dynamics, which enables the system to evolve to a spin cat state, conditioned upon there being no jumps (with jumps corresponding to photon emissions from the cavity). If there is a jump, however, the system evolves probabilistically into one of a finite number of entangled-state cycles, where the system then undergoes a persistent sequence of jumps between two Dicke state superpositions in a rotated basis.

Finally, we close this thesis with our conclusions and outlook in Chapter 11.

Part II

Preliminaries

Chapter 2

Open Quantum Systems

2.1 Quantum Harmonic Oscillator

Harmonic oscillators are ubiquitous in quantum mechanics; a lot of systems can be boiled down to them and in this thesis alone they will serve to describe the dynamics of two very distinct subsystems: the electromagnetic field and the centre-of-mass motion of trapped particles. The Hamiltonian of a classical harmonic oscillator is made up of a kinetic and a potential part. Quantising the momentum and the position brings us to the quantum analogue ($m = \hbar = 1$)

$$\hat{H} = \frac{\hat{p}^2}{2} + \frac{\omega^2 \hat{x}^2}{2}. \tag{2.1}$$

A more useful picture can be gained by introducing the ladder operators, i.e., the annihilation and creation operators

$$\begin{aligned} \hat{a} &= \sqrt{\frac{1}{2\omega}}(\omega\hat{x} + i\hat{p}), \\ \hat{a}^\dagger &= \sqrt{\frac{1}{2\omega}}(\omega\hat{x} - i\hat{p}), \end{aligned} \tag{2.2}$$

which allow us to bring the Hamiltonian into the form that will be most prevalent in this thesis,

$$\hat{H} = \omega\left(\hat{a}^\dagger\hat{a}+\frac{1}{2}\right). \tag{2.3}$$

The ladder operators satisfy the canonical commutation relations

$$\begin{aligned}[\hat{a},\hat{a}^\dagger] &= 1,\\ [\hat{a},\hat{a}] &= [\hat{a}^\dagger,\hat{a}^\dagger] = 0.\end{aligned} \tag{2.4}$$

Since the ladder operators are not Hermitian ($\hat{a} \neq \hat{a}^\dagger$), they are not observables. For this reason the two orthogonal observables of the phase space from the initial form of the harmonic oscillator: the position quadrature,

$$\hat{x} = \sqrt{\frac{1}{2\omega}}(\hat{a}+\hat{a}^\dagger), \tag{2.5}$$

and the momentum quadrature

$$\hat{p} = -i\sqrt{\frac{\omega}{2}}(\hat{a}-\hat{a}^\dagger), \tag{2.6}$$

still retain importance as quantities that are actually measurable through experiment.

In this thesis we are interested in engineering and, for verification purposes, recognising specific (optical) quantum states. To this end, we are interested in a way to unambiguously represent said states in (optical) phase space. The Wigner quasiprobability distribution, a function which for an arbitrary state

$\hat{\rho}$, mixed or pure, provides this, is defined through

$$W(x,p) = \frac{1}{\pi}\int_{-\infty}^{\infty}\langle x+y|\hat{\rho}|x-y\rangle e^{2ipy}dy. \tag{2.7}$$

The Wigner function is normalised but can become negative, in which case it is a sign for the "quantumness" of $\hat{\rho}$ [39, 40]. An example for this behaviour are Fock states, which will be introduced in the next Section and whose Wigner functions we will encounter several times in the Chapters 7 and 8. The marginals, or probability distributions for the quadratures, can be obtained by integrating over one of x or y, e.g., for the position distribution

$$\int_{-\infty}^{\infty} W(x,p)dp = \langle x|\hat{\rho}|x\rangle, \tag{2.8}$$

which is exactly what we will be measuring later in our modelling of homodyne detection.

2.2 Number State Representation

The number state representation arises naturally from forming a basis from the eigenstates $|n\rangle$ of the harmonic oscillator or equivalently the number operator

$$\hat{n} = \hat{a}^{\dagger}\hat{a}. \tag{2.9}$$

These eigenstates $|n\rangle$ are called Fock or number states and stand for a quantum field excited by n quanta of energy. As such this is the most common way to

describe quantum states of light but can be used for any bosonic mode, with

$$\begin{aligned} \hat{a}^\dagger \hat{a}|n\rangle &= n|n\rangle, \\ \hat{a}|n\rangle &= \sqrt{n}|n-1\rangle, \\ \hat{a}^\dagger|n\rangle &= \sqrt{n+1}|n+1\rangle. \end{aligned} \tag{2.10}$$

Other important states can be readily expressed in terms of the number states. One such example are coherent states,

$$|\alpha\rangle = e^{-\frac{|\alpha|^2}{2}} \sum_{n=0}^{\infty} \frac{\alpha^n}{\sqrt{n!}}|n\rangle, \tag{2.11}$$

which are defined through being eigenstates of the annihilation operator,

$$\begin{aligned} \hat{a}|\alpha\rangle &= \alpha|\alpha\rangle, \\ \langle\alpha|\hat{a}^\dagger &= \langle\alpha|\alpha^*. \end{aligned} \tag{2.12}$$

Coherent states satisfy the minimum uncertainty of the Heisenberg inequality,

$$\Delta\hat{x}\Delta\hat{p} = \frac{\hbar}{2}, \tag{2.13}$$

where $\hat{x}$ is the amplitude quadrature and $\hat{p}$ the phase quadrature of the light field. This means that these are the states that behave the most "classical" and are therefore usually used to represent classical fields such as a laser, with α taking the role of the classical field amplitude.

Another class of very important exemplary states is the thermal state [41]. Thermal states are used when the light field or any other field for that matter is described as a thermodynamic system in contact with a bath at temperature

T. Contrary to the number and coherent states, it is a mixed state represented by the density operator

$$\hat{\rho} = \sum_{n=0}^{\infty} \frac{\bar{n}^n}{(\bar{n}+1)^{n+1}} |n\rangle\langle n|, \tag{2.14}$$

where

$$\bar{n} = \frac{e^{-\beta\hbar\omega}}{1-e^{-\beta\hbar\omega}} \tag{2.15}$$

is the average number of photons with $\beta = \frac{1}{k_B T}$.

2.3 Master Equation

A major tool for the description of open quantum systems in quantum optics is the master equation [42, 43]. The idea here is to describe the total system as a combination of two coupled subsystems: one being the "system" subsystem S that is actually studied (in our case atoms and cavities) and the other one being the environment (or reservoir) E. The total dynamics are described by the Hamiltonian

$$\hat{H} = \hat{H}_S + \hat{H}_E + \hat{H}_{SE}, \tag{2.16}$$

where the first two terms describe the S and E subsystems and the last one the interaction between these subsystems.

The total system evolves according to the von Neumann equation

$$\dot{\hat{\rho}} = -i\Big[\hat{H}, \hat{\rho}\Big], \tag{2.17}$$

and is fully coherent and time reversible. We, however, are generally only

interested in and/or can only keep track of the dynamics of the system alone, as described by the reduced density operator

$$\hat{\rho}_S(t) = \mathrm{Tr}_E(\hat{\rho}(t)), \tag{2.18}$$

where the environment has been traced out. This gives rise to incoherent and irreversible dynamics for $\hat{\rho}_S$. In the interaction picture we have

$$\dot{\hat{\rho}}(t) = -i\Big[\hat{V}(t), \hat{\rho}(t)\Big] \tag{2.19}$$

where we have the interaction Hamiltonian

$$\hat{V}(t) = e^{\frac{i}{\hbar}(\hat{H}_S+\hat{H}_E)t}\hat{H}e^{-\frac{i}{\hbar}(\hat{H}_S+\hat{H}_E)t} \tag{2.20}$$

and

$$\hat{\rho}(t) = e^{\frac{i}{\hbar}(\hat{H}_S+\hat{H}_E)t}\hat{\rho}e^{-\frac{i}{\hbar}(H_S+H_E)t}. \tag{2.21}$$

We integrate formally which yields

$$\hat{\rho}(t) = \hat{\rho}(t_0) - \frac{i}{\hbar}\int_{t_0}^{t}\Big[\hat{V}(t'), \hat{\rho}(t')\Big]dt'. \tag{2.22}$$

By plugging Eq. (2.22) into Eq. (2.19) we create a Born series from perturbation theory,

$$\dot{\hat{\rho}}(t) = \frac{1}{i\hbar}\Big[\hat{V}(t), \hat{\rho}(t_0)\Big] - \frac{1}{\hbar^2}\int_{t_0}^{t}\Big[\hat{V}(t), [V(t'), \hat{\rho}(t')]\Big]dt'. \tag{2.23}$$

At this stage we use the Born approximation, saying that the coupling to the environment is weak and therefore we can write the density matrix as the factorised density matrix without coupling plus higher order terms which are neglected,

$$\hat{\rho}(t) = \hat{\rho}_S(t) \otimes \hat{\rho}_E(t_0) + \mathcal{O}(\hat{V}), \tag{2.24}$$

where we also posited that the environment is in equilibrium. We trace out the environment and obtain

$$\begin{aligned} \dot{\hat{\rho}}_S(t) = &-i\mathrm{Tr}_E(\Big[\hat{V}(t), \hat{\rho}_S(t_0) \otimes \hat{\rho}_E(t_0)\Big]) \\ &-\mathrm{Tr}_E(\int_{t_0}^{t} \Big[\hat{V}(t), \Big[\hat{V}(t'), \hat{\rho}_S(t') \otimes \hat{\rho}_E(t_0)\Big]\Big] dt'). \end{aligned} \tag{2.25}$$

Now we perform the Markov approximation, which starts by realising that our expression is made up by terms like

$$C(t'-t) = \mathrm{Tr}_E(\hat{V}(t)\hat{V}(t')\hat{\rho}_E(t_0)), \tag{2.26}$$

which are bath correlation functions. In the systems we will be considering in this thesis the bath correlation time scale (optical frequencies of the order of THz) is much faster than the relaxation time of S (life time of atomic and cavity excitations of the order of MHz), so we can take $C(t'-t) = 0$ for all $t' \neq t$ and hence we replace $\rho_S(t')$ by $\rho_S(t)$,

$$\begin{aligned} \dot{\hat{\rho}}_S(t) = &-\mathrm{Tr}_E(\Big[\hat{V}(t), \hat{\rho}_S(t_0) \otimes \hat{\rho}_E(t_0)\Big]) \\ &-\mathrm{Tr}_E(\frac{1}{\hbar^2} \int_{t_0}^{t} \Big[\hat{V}(t), \Big[\hat{V}(t'), \hat{\rho}_S(t) \otimes \hat{\rho}_E(t_0)\Big]\Big] dt'). \end{aligned} \tag{2.27}$$

Our environment is considered to be a bunch of harmonic oscillators with

frequencies ω and annihilation operator $\hat{b}(\omega)$

$$\hat{H}_E = \int_{-\infty}^{\infty} d\omega \omega \hat{b}^\dagger(\omega)\hat{b}(\omega). \tag{2.28}$$

Typical assumptions about the interaction between the system and the bath are that it is linear in the bath operators, independent of frequency, and no terms proportional to $\hat{b}\hat{c}$ and $\hat{b}^\dagger\hat{c}^\dagger$, e.g.,

$$\hat{V} \propto \hat{b}\hat{c}^\dagger + \hat{b}^\dagger\hat{c}. \tag{2.29}$$

If the various modes of the bath are assumed to be in thermal states, all with average occupation number $\bar{n}$, we can explicitly evaluate the correlation functions,

$$\begin{aligned} \mathrm{Tr}_E\left[\hat{b}\hat{\rho}_E(t')\right] &= 0, \\ \mathrm{Tr}_E\left[\hat{b}^\dagger\hat{\rho}_E(t')\right] &= 0, \\ \mathrm{Tr}_E\left[\hat{b}^\dagger\hat{b}\hat{\rho}_E(t')\right] &= \bar{n}, \\ \mathrm{Tr}_E\left[\hat{b}\hat{b}^\dagger\hat{\rho}_E(t')\right] &= (\bar{n}+1), \end{aligned} \tag{2.30}$$

which leads us to the Master equation in Lindblad form,

$$\frac{\partial}{\partial t}\hat{\rho}_S(t) = \frac{\gamma}{2}(\bar{n}+1)\mathcal{D}[\hat{c}]\hat{\rho}_S + \frac{\gamma}{2}\bar{n}\mathcal{D}[\hat{c}^\dagger]\hat{\rho}_S \tag{2.31}$$

where the integration and prefactors have been integrated into γ, which represents the rate at which the interaction dampens the system dynamics. Ad-

ditionally, we have defined the Lindblad superoperator

$$\mathcal{D}[\hat{O}]\hat{\rho} = 2\hat{O}\hat{\rho}\hat{O}^\dagger - \hat{\rho}\hat{O}^\dagger\hat{O} - \hat{O}^\dagger\hat{O}\hat{\rho}. \tag{2.32}$$

Back in the Schrödinger picture we have

$$\dot{\hat{\rho}}_S = -i\Big[\hat{H}_S, \hat{\rho}_S\Big] + \frac{\gamma}{2}(2\bar{n}+1)\mathcal{D}[\hat{O}]\hat{\rho}_S + \frac{\gamma}{2}\bar{n}\mathcal{D}[\hat{O}]\hat{\rho}_S = \mathcal{L}\hat{\rho}_S, \tag{2.33}$$

where we introduce the Liouville superoperator $\mathcal{L}$ that combines the free evolution and damping from being an open system.

2.4 Quantum Trajectories

Quantum trajectories (or Monte Carlo Wave Function) [43–45] represent a different approach to solving the open system problem, that is nonetheless completely equivalent to the master equation. A trajectory corresponds to the path that a wave function follows subject to the probabilistic evolution prescribed by the Master equation. The density matrix solution from the Master equation is obtained by averaging over the ensemble of wave functions obtained from different trajectories,

$$\hat{\rho}(t) = \overline{|\psi(t)\rangle\langle\psi(t)|}. \tag{2.34}$$

Quantum trajectories can be a useful analytical tool if one wants to quickly gauge what is happening in a given system, but also a potent numerical one, if the dimension of the problem d is large and it becomes computationally less demanding to simulate a vector of size d than a $d\times d$ matrix. The trade-off being, that usually a high number of trajectories is required for the average to converge.

Given a quantum system described by the following Master equation

$$\dot{\hat{\rho}} = -i\Big[\hat{H}, \hat{\rho}\Big] - \big(\hat{c}^\dagger \hat{c}\hat{\rho} + \hat{\rho}\hat{c}^\dagger \hat{c}\big) + 2\hat{c}^\dagger \hat{\rho}\hat{c}, \tag{2.35}$$

with the Lindblad operator $\hat{c}$, we construct the non-Hermitian effective Hamiltonian

$$\hat{H}_{\mathrm{NH}} = \hat{H} - ic^\dagger c, \tag{2.36}$$

which, if plugged into the von Neumann equation, yields almost the whole of Eq. (2.35) except for the last term going with $\hat{c}^\dagger \hat{\rho}\hat{c}$, which corresponds to quantum jumps.

Let us assume without loss of generality that we start at a time t in the state $|\psi(t)\rangle$. During an infinitesimal time step, the quantum state evolves according to

$$|\psi(t+\delta t)\rangle = e^{-i\hat{H}_{\mathrm{NH}}t}|\psi(t)\rangle = \Big(1 - i\hat{H}_{\mathrm{NH}}\delta t\Big)|\psi(t)\rangle \tag{2.37}$$

where we truncated the Taylor expansion to first order, assuming that $\hat{H}_{\mathrm{NH}}\delta t$ is small. The non-Hermiticity makes it so that the norm of this new wave function is no longer equal to one,

$$\langle\psi(t+\delta t)|\psi(t+\delta t)\rangle = 1 - \delta p + \mathcal{O}(\delta t^2), \tag{2.38}$$

but rather has dropped by an amount

$$\delta p = 2\delta t \langle\psi(t)|\hat{c}^\dagger \hat{c}|\psi(t)\rangle, \tag{2.39}$$

which represents the probability for a jump to happen. It is at this stage that

the missing quantum jump part from the Master equation is reintroduced. A random number η is drawn from a uniform distribution between 0 and 1. If $\eta < \delta p$, a jump is deemed to have occurred, i.e., the jump operator is applied to the quantum state. Otherwise, $|\psi(t+\delta t)\rangle$ is just kept, but no matter what the outcome the result needs to renormalised:

$$|\psi(t+\delta t)\rangle = \begin{cases} \frac{|\psi(t+\delta t)\rangle}{\sqrt{\langle\psi(t+\delta t)|\psi(t+\delta t)\rangle}} & \text{no jump} \\ \frac{\hat{c}|\psi(t)\rangle}{\sqrt{\langle\psi(t)|\hat{c}^\dagger\hat{c}|\psi(t)\rangle}} & \text{jump} \end{cases}, \tag{2.40}$$

after which the whole process is repeated until the desired time is reached. The average density operator at time $t+\delta t$ is the sum of these two possible outcomes, weighted by their respective probabilities

$$\begin{aligned} \overline{\hat{\rho}(t+\delta t)} &= (1-\delta p)\frac{|\psi(t+\delta t)\rangle\langle\psi(t+\delta t)|}{\langle\psi(t+\delta t)|\psi(t+\delta t)\rangle} + \delta p\frac{\hat{c}|\psi(t)\rangle\langle\psi(t)|\hat{c}^\dagger}{\langle\psi(t)|\hat{c}^\dagger\hat{c}|\psi(t)\rangle} \\ &= \hat{\rho}(t) - i\delta t\left[\hat{H}_{\mathrm{NH}}, \hat{\rho}(t)\right] + 2\delta t\hat{c}\hat{\rho}(t)\hat{c}^\dagger. \end{aligned} \tag{2.41}$$

By averaging over the possible states at time t and still assuming δt to be infinitesimally small, we can write

$$\dot{\overline{\hat{\rho}}} = -i\left[\hat{H}, \overline{\hat{\rho}}\right] + \mathcal{D}[\hat{c}]\overline{\hat{\rho}}, \tag{2.42}$$

which is equivalent to Eq. (2.35) and proves that quantum trajectories reproduce the master equation.

2.5 Quantum Regression

The quantum regression theorem [43, 46] is a helpful tool when it comes to calculating two-time averages such as correlation functions from the master equation.

For a density operator $\hat{\rho}$, the product average of three system operators $\hat{O}_1$, $\hat{O}_2$ and $\hat{O}_3$ is given by the following total trace

$$\langle \hat{O}_1(t)\hat{O}_2(t+\tau)\hat{O}_3(t)\rangle = \mathrm{Tr}\{\hat{\rho}(0)\hat{O}_1(t)\hat{O}_2(t+\tau)\hat{O}_3(t)\}. \tag{2.43}$$

We substitute the formal solutions to the Heisenberg equation for the system and density operators

$$\begin{aligned} \hat{O}_j(t) &= e^{i\hat{H}t}\hat{O}_j(0)e^{-i\hat{H}t} \\ \hat{\rho}(0) &= e^{i\hat{H}t}\hat{\rho}(t)e^{-i\hat{H}t}, \end{aligned} \tag{2.44}$$

which yields

$$\langle \hat{O}_1(t)\hat{O}_2(t+\tau)\hat{O}_3(t)\rangle = \mathrm{Tr}\{e^{i\hat{H}t}\hat{\rho}(t)\hat{O}_1(0)e^{i\hat{H}\tau}\hat{O}_2(0)e^{-i\hat{H}\tau}\hat{O}_3(0)e^{-i\hat{H}t}\}. \tag{2.45}$$

Next, we use the fact that the trace is unchanged under a cyclic permutation and that $\hat{O}_2$ is only acting on the system and not the reservoir, so

$$\langle \hat{O}_1(t)\hat{O}_2(t+\tau)\hat{O}_3(t)\rangle = \mathrm{Tr}_S\{\hat{O}_2(0)\mathrm{Tr}_E\{e^{-i\hat{H}\tau}\hat{O}_3(0)\hat{\rho}(t)\hat{O}_1(0)e^{i\hat{H}\tau}\}\}. \tag{2.46}$$

The remaining $e^{\pm i\hat{H}\tau}$ terms in the trace mean that $\hat{O}_3(0)\hat{\rho}_S(t)\hat{O}_1(0)$ gets evolved an additional time τ with the reduced system dynamics,

$$\mathrm{Tr}_E\{e^{-i\hat{H}\tau}\hat{O}_3(0)\hat{\rho}(t)\hat{O}_1(0)e^{i\hat{H}\tau}\} = e^{\mathcal{L}\tau}\mathrm{Tr}_E\{\hat{O}_3(0)\hat{\rho}(t)\hat{O}_1(0)\}, \tag{2.47}$$

where $\mathcal{L}$ is the Liouvillian describing the reduced system dynamics, i.e., $\dot{\hat{\rho}}_S = \mathcal{L}\hat{\rho}_S$. Since the $\hat{O}_j$ are system operators, evaluating the trace over the environment just replaces the full density matrix with the reduced system density

matrix $\hat{\rho}_S$,

$$\mathrm{Tr}_E\{\hat{O}_3(0)\hat{\rho}(t)\hat{O}_1(0)\} = \hat{O}_3(0)\hat{\rho}_S(t)\hat{O}_1(0), \tag{2.48}$$

which leaves us with the final result

$$\langle\hat{O}_1(t)\hat{O}_2(t+\tau)\hat{O}_3(t)\rangle = \mathrm{Tr}_S\{\hat{O}_2(0)e^{\mathcal{L}\tau}[\hat{O}_3(0)\hat{\rho}_S(t)\hat{O}_1(0)]\}. \tag{2.49}$$

In the case where our system tends towards a steady state, we can set $t \to \infty$ and replace the density operator with the steady state $\hat{\rho}_{SS}$, i.e.,

$$\langle\hat{O}_1(0)\hat{O}_2(\tau)\hat{O}_3(0)\rangle = \mathrm{Tr}\{\hat{O}_2(0)e^{\mathcal{L}\tau}[\hat{O}_3(0)\hat{\rho}_{SS}\hat{O}_1(0)]\}. \tag{2.50}$$

Chapter 3

Atomic Physics of Alkali Metals

3.1 Energy Level Structure of Alkali Atoms

Alkali atoms are similar to the hydrogen atom and are called "hydrogenic" atoms at times, in the sense that all the electronic subshells are filled and a single electron is in the outermost shell. The electrons between the outermost valence electron and the nucleus shield that electron from the nucleus, such that we can view the nucleus-subshell electrons compound as a compound point charge of charge +1. Indeed, the gross electronic structure of an alkali atom has basically the same formula as that of a hydrogen atom [47],

$$E(n,l) = -\frac{hcR_\infty}{(n-\delta_l)^2}, \tag{3.1}$$

except that the principal quantum number n has been replaced by an effective principal quantum number,

$$n^* = n-\delta_l, \tag{3.2}$$

which is smaller by a value δ_l, called the quantum defect. Depending on the orbital angular momentum l of the electron, the electronic wave function might penetrate inside the core region and experience less shielding, a higher nuclear

charge, and thus a larger quantum defect. The quantum defect is maximal for $l = 0$ and drops off quickly for larger l as the shielding becomes complete.

Similarly to the hydrogen atom, each of these levels will split up into a fine structure doublet from the spin-orbit coupling, resulting in the new quantum number, the total electron angular momentum,

$$\mathbf{J} = \mathbf{L}+\mathbf{S}, \quad |L-S| < J < L+S. \tag{3.3}$$

After that comes the coupling of the total angular momentum with the nuclear spin, resulting in the total atomic angular momentum

$$\mathbf{F} = \mathbf{J}+\mathbf{I}, \quad |J-I| < F < J+I. \tag{3.4}$$

The additional energy shift due to this hyperfine splitting is given by [48]

$$E(F,J,I) = \frac{1}{2}AK + B\frac{\frac{3}{2}K(K+1)-2I(I+1)J(J+1)}{2I(2I-1)J(2J-1)}, \tag{3.5}$$

where $K = F(F+1)-I(I+1)-J(J+1)$, A is the magnetic dipole constant, and B is the electric quadrupole constant. Figs. 3.1-3.2 shows a schematic representation of the resulting energy level structure for a selection of atoms and transitions used later on.

3.2 Static Magnetic Fields

The $2F+1$ hyperfine sublevels $|F, m_F\rangle$ with $-F \leq m_F \leq F$ are degenerate. In the presence of an external magnetic field, said degeneracy is lost due to their different magnetic moments. Assuming a weak magnetic field, the sublevels experience a linear energy shift [49, 50],

$$\hat{H} = m_F \mu_B g_F B |F, m_F\rangle\langle F, m_F|, \tag{3.6}$$

where μ_B is the Bohr magneton, g_F the hyperfine Landé g-factor and B the magnetic field strength. This is called the Zeeman effect and the different $|F, m_F\rangle$ will throughout the text also be referred to as Zeeman or magnetic sublevels. Lifting the degeneracy in such a way can be used to isolate specific transitions, e.g. the ground states have g_F of opposite sign and thus their Zeeman level shift away from each other at one end of the Zeeman ladder.

At higher magnetic field strengths, the splitting stops being linear, and the levels start to rearrange according to their m_J, M_I; this is referred to as the Paschen-Back effect.

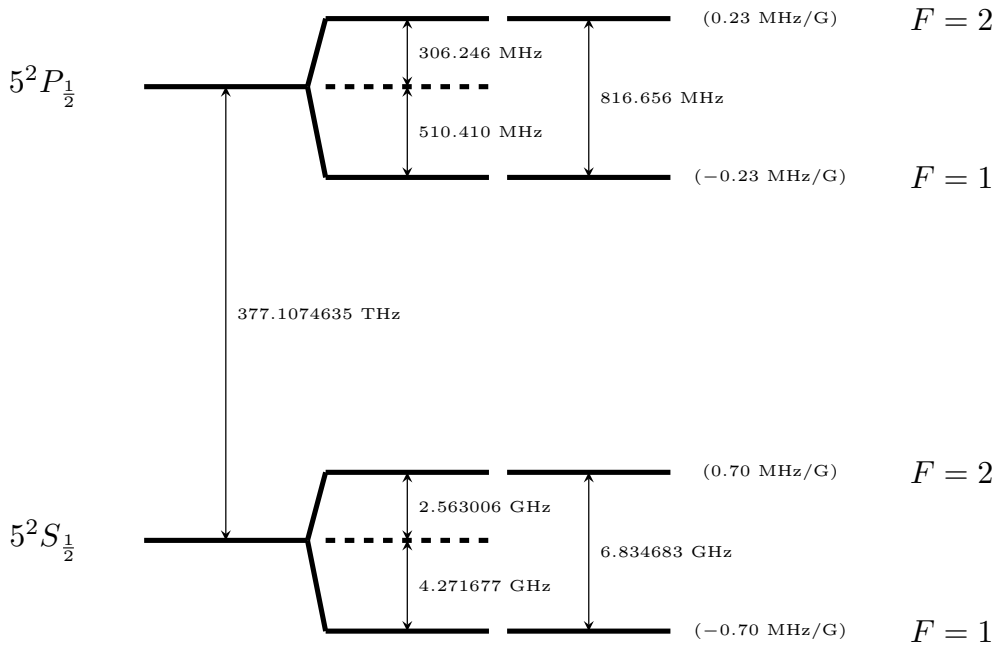

(a) D_1 line ^{87}Rb

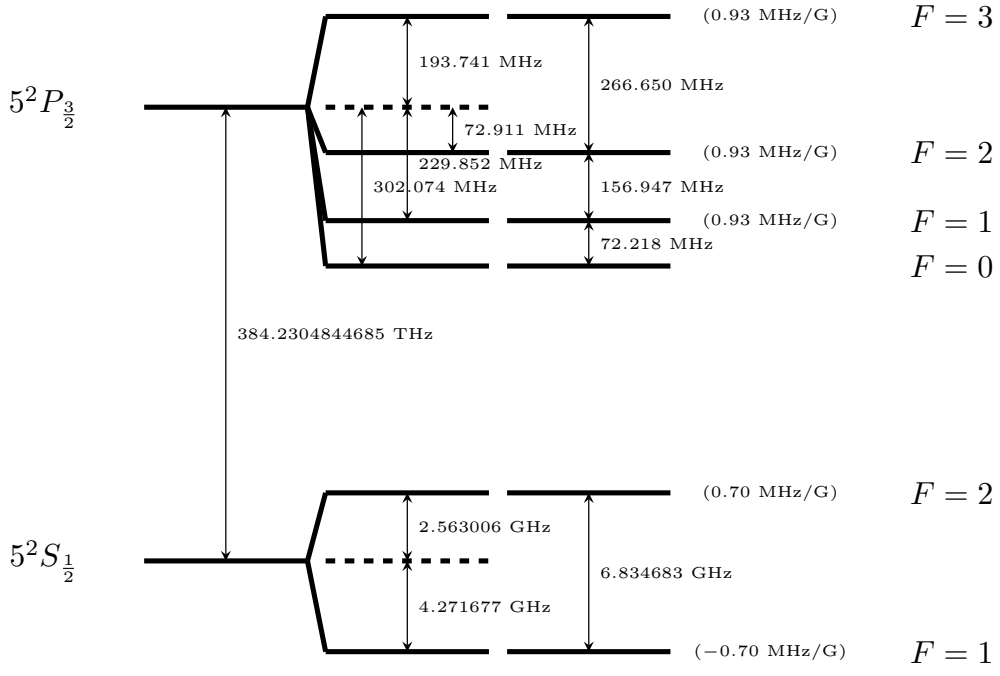

(b) D_2 line ^{87}Rb

Figure 3.1: Energy level diagrams of the D_1 and D_2 lines of ^{87}Rb [49].

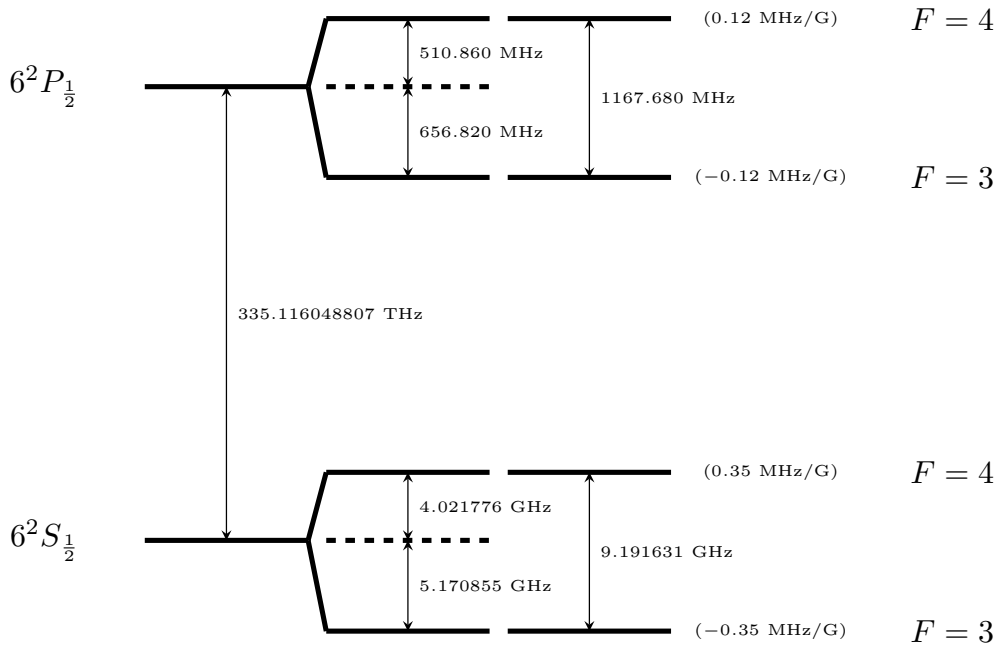

(a) D_1 line ^{133}Cs

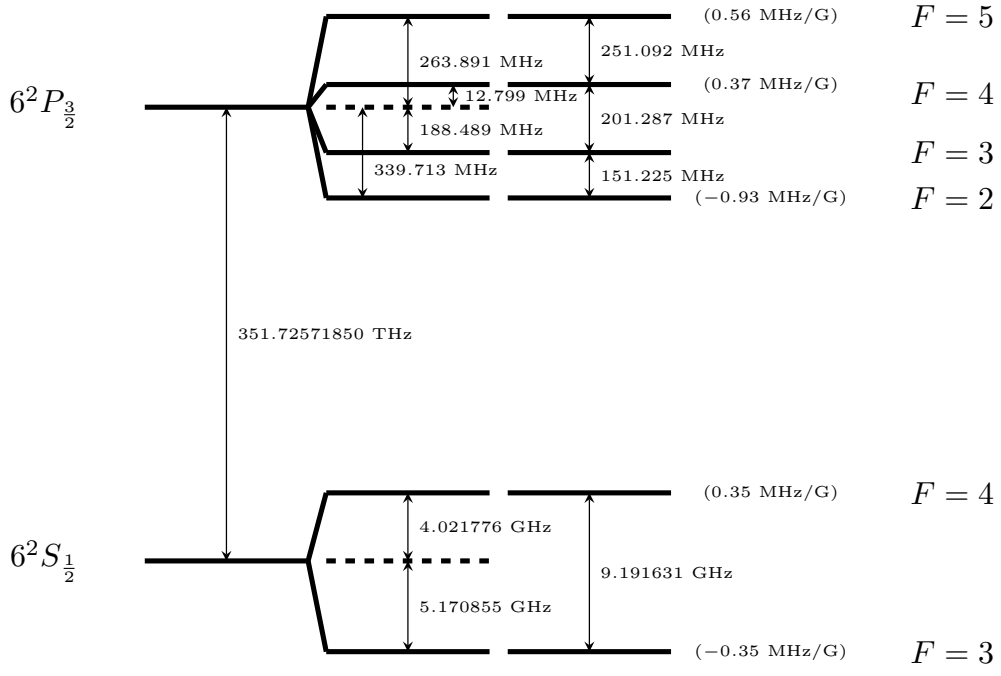

(b) D_2 line ^{133}Cs

Figure 3.2: Energy level diagrams of the D_1 and D_2 lines of ^{133}Cs [50].

3.3 Spinor Systems

In this thesis we will be working a lot with spinors particles, i.e., particles with intrinsic spin degrees of freedom, and therefore we shall introduce the language that we will be using to describe these systems. Let us remind ourselves of the Pauli spin matrices:

$$\begin{aligned}\hat{\boldsymbol{\sigma}} &= \hat{\boldsymbol{x}}\hat{\sigma}_x + \hat{\boldsymbol{y}}\hat{\sigma}_y + \hat{\boldsymbol{z}}\hat{\sigma}_z,\\ \hat{\sigma}_x &= \begin{pmatrix} 0 & 1 \\ 1 & 0 \end{pmatrix},\\ \hat{\sigma}_y &= \begin{pmatrix} 0 & i \\ i & 0 \end{pmatrix},\\ \hat{\sigma}_z &= \begin{pmatrix} 1 & 0 \\ 0 & -1 \end{pmatrix},\end{aligned} \tag{3.7}$$

and the associated ladder operators $\hat{\sigma}_\pm = \hat{\sigma}_x \pm i\hat{\sigma}_y$. The corresponding spin operators for a spin-$\frac{1}{2}$ particle $\hat{\mathbf{S}}$, $\hat{S}_x$, $\hat{S}_y$, $\hat{S}_z$, $\hat{S}_+$ and $\hat{S}_-$ are obtained by multiplying these by a factor $\frac{1}{2}$.

If we were to consider now an ensemble of N of these spin-$\frac{1}{2}$ particles we can construct the collective spin operators by summing up the spin operators for every spinor,

$$\begin{aligned}\hat{J}_p &= \frac{1}{2}\sum_i^N \hat{\sigma}_p^{(i)} = \frac{1}{2}\left(\sigma_p^{(1)} \otimes \mathbb{1}^{\otimes N-1} + \mathbb{1} \otimes \sigma_p^{(2)} \otimes \mathbb{1}^{\otimes N-2} + \dots\right)\\ &= \bigoplus_{S=0 \text{ or } \frac{1}{2}}^{\frac{N}{2}} \hat{S}_p^{(S)},\end{aligned} \tag{3.8}$$

where in the second row we have used that in the appropriate frame the collective operator can be written as a direct sum of spin matrices $\hat{S}_p^{(S)}$ of spin S whose subspace correspond to the multiplets obtained from spin additions.

The direct summation goes over all the integers (including 0) or all the half-integers, depending on whether $\frac{N}{2}$ is an integer or half-integer. This new frame gets spanned by the so-called Dicke states $|S,m\rangle$ for all spins S and magnetic quantum number $-S \leq m \leq S$, which are the eigenstates of the collective spin operators $\hat{\mathbf{J}}^2$ and the $\hat{J}_z$. Consequently, in each subspace of spin S, the corresponding Dicke states of the same spin are also the eigenstates of the spin operators $\hat{\mathbf{S}}^2$ and $\hat{S}_z$ and get acted on as follows:

$$\begin{aligned}
\hat{\mathbf{J}}^2|S,m\rangle &= \hat{\mathbf{S}}^2|S,m\rangle = S(S{+}1)|S,m\rangle, \\
\hat{J}_z|S,m\rangle &= \hat{S}_z|S,m\rangle = m|S,m\rangle, \\
\hat{J}_\pm|S,m\rangle &= \hat{S}_\pm|S,m\rangle = \sqrt{S(S{+}1){-}m(m{\pm}1)}|S,m{\pm}1\rangle.
\end{aligned} \tag{3.9}$$

The form of these operators just depends on the total spin S and will be used to describe spinors of spin S, so that for the collective operators it does not matter what kind of spinors one is adding up, but just their maximal spin sum, i.e., the collective operators for two spin-1 or four spin-$\frac{1}{2}$ are exactly the same. The spin matrices, and by extension their collective counterparts, fulfill the following commutation relationships

$$\begin{aligned}
\left[\hat{S}_y, \hat{S}_z\right] &= i\hat{S}_x, \\
\left[\hat{S}_z, \hat{S}_x\right] &= i\hat{S}_y, \\
\left[\hat{S}_y, \hat{S}_z\right] &= i\hat{S}_z,
\end{aligned} \tag{3.10}$$

and

$$\begin{aligned}
\left[\hat{S}_z, \hat{S}_+\right] &= \hat{S}_+, \\
\left[\hat{S}_z, \hat{S}_-\right] &= -\hat{S}_-, \\
\left[\hat{S}_+, \hat{S}_-\right] &= 2\hat{S}_z,
\end{aligned} \tag{3.11}$$

for the raising and lowering operators.

3.4 Atoms interacting with Classical Fields

Throughout this thesis, the light fields considered will always have optical wave lengths, i.e., typically 780 nm (^{87}Rb) or 852 nm (^{133}Cs). This is about four orders of magnitude larger than the size of an atom. We can therefore assume the field to vary slowly, or to be constant in space, from the perspective of the atom. For minimal coupling this leads to the interaction Hamiltonian in, the dipole approximation,

$$\hat{H}_I = -q_e \mathbf{p}\cdot\mathbf{A}(\mathbf{r}_0, t) + \frac{q_e^2}{2m}\mathbf{A}^2(\mathbf{r}_0, t), \tag{3.12}$$

where the second term is usually small enough to be ignored. By performing the gauge transformation $\psi \rightarrow e^{iq_e\mathbf{A}(\mathbf{r}_0,t)}\psi$ we can express the interaction in terms of the gauge-independent $\mathbf{E}$,

$$\hat{H}_I = -q_e \mathbf{E}(\mathbf{r}_0, t)\cdot\mathbf{r}, \tag{3.13}$$

where q_e is the elemental charge, $\mathbf{r}$ the position of the atom and $\mathbf{E}$ the electric field inducing the interaction. Let us assume that the atom is interacting with a laser field of frequency ν, i.e.

$$\mathbf{E} = \hat{\epsilon}(\mathcal{E}e^{-i\nu t} + \mathcal{E}^* e^{i\nu t}) \tag{3.14}$$

and that the atom is a two-level system with a ground state $|g\rangle$ and an excited state $|e\rangle$. Using the completeness relationship $\mathbb{1} = |e\rangle\langle e| + |g\rangle\langle g|$, we have

$$\mathbb{1}\hat{H}_I\mathbb{1} = -\hat{\epsilon}\mathcal{E}(\mathbf{d}|e\rangle\langle g|e^{-i\nu t} + \mathbf{d}^*|g\rangle\langle e|e^{-i\nu t} + \mathbf{d}|e\rangle\langle g|e^{i\nu t} + \mathbf{d}^*|g\rangle\langle e|e^{i\nu t}), \tag{3.15}$$

where we have defined the dipole transition element

$$\mathbf{d} = q_e\langle e|\mathbf{r}|g\rangle = q_e\langle g|\mathbf{r}|e\rangle^* \tag{3.16}$$

and the terms proportional to $|g\rangle\langle g|$ and $|e\rangle\langle e|$ drop out for parity reasons. We transform the full Hamiltonian

$$\hat{H} = \omega_g|g\rangle\langle g| + \omega_e|e\rangle\langle e| + \hat{H}_I \tag{3.17}$$

with the unitary transformation defined by the transformation Hamiltonian

$$\hat{H}_T = \omega_g|g\rangle\langle g| + (\omega_g + \nu)|e\rangle\langle e| \tag{3.18}$$

to obtain the interaction picture Hamiltonian

$$\hat{V} = e^{i\hat{H}_T t}(\hat{H} - \hat{H}_T)e^{-i\hat{H}_T t} = -\Delta|e\rangle\langle e| + \frac{\Omega}{2}(|e\rangle\langle g| + |g\rangle\langle e|), \tag{3.19}$$

where we have omitted two terms proportional to $|g\rangle\langle e|e^{-2i\nu t}$ and $|e\rangle\langle g|e^{2i\nu t}$ since they average out due to their rapid oscillating nature (rotating wave approximation). Here,

$$\Delta = \nu - \omega_e + \omega_g \tag{3.20}$$

is the detuning and

$$\Omega = -2\mathcal{E}\hat{\epsilon}\mathbf{d} \tag{3.21}$$

is the Rabi frequency.

The general solution for the state amplitudes depends on the generalised Rabi frequency

$$\Omega_G = \sqrt{\Delta^2+\Omega^2}. \tag{3.22}$$

In the case of a far off-resonant laser ($\Delta \gg \Omega$), there is effectively no evolution; the amplitudes of the states remain the same and only incur a phase shift. This serves as a justification for our few-level approximation that we will often use to discard atomic levels that are far-detuned and thus not immediately involved. Otherwise, if the detuning is not much bigger than the Rabi frequency, the population inversion (the difference in state population) is proportional to [42]

$$-\frac{\Delta^2}{\Omega_G^2}-\frac{\Omega^2}{\Omega_G^2}\cos(\Omega_G t). \tag{3.23}$$

Finally, on resonance ($\Delta = 0$) the population transfer between the ground and the excited state is complete and happens periodically at a rate Ω.

3.5 Spontaneous Emission

Excited states of the atom tend to relax over time via spontaneous emission, which can be considered as stimulated emission through the vacuum fluctuations. Still considering a two-level atom, but now interacting with the infinite ensemble of modes of the free electromagnetic field, we have

$$\hat{H}_{SE} = \sum_{\mathbf{k}} \left(g_{\mathbf{k}}\hat{\sigma}_+ e^{i\Delta_{\mathbf{k}}t}+g_{\mathbf{k}}^*\hat{\sigma}_- e^{-i\Delta_{\mathbf{k}}t}\right), \tag{3.24}$$

where $\hat{\sigma}_+ = |e\rangle\langle g|$ and $\hat{\sigma}_- = |g\rangle\langle e|$. Following the standard derivation of the Master equation we end up with the Lindblad form

$$\dot{\hat{\rho}} = \frac{\gamma}{2}\mathcal{D}[\hat{\sigma}_-]\hat{\rho}, \tag{3.25}$$

where

$$\gamma = 2\int_0^t dt' \sum_{\mathbf{k}} |g_{\mathbf{k}}|^2 e^{-i\Delta_{\mathbf{k}}(t-t')}, \tag{3.26}$$

with

$$|g_{\mathbf{k}}|^2 = \frac{|\mathbf{d}|^2\nu_{\mathbf{k}}}{2\epsilon_0\mathcal{V}}\cos^2\theta. \tag{3.27}$$

Firstly, the full field forms a continuum, so we replace the discrete summation over the modes by an integral and add the mode density as a prefactor,

$$\sum_{\mathbf{k}} = 2\frac{\mathcal{V}}{(2\pi)^3}\int d\phi \int d\theta \sin\theta \int d\nu_{\mathbf{k}} \frac{\nu_{\mathbf{k}}^2}{c^3}. \tag{3.28}$$

Next up we perform the Wigner-Weisskopf approximation [51]: the frequency integral only contributes when $\nu_{\mathbf{k}} \approx \omega$ due to the exponential shape:

$$\int_0^\infty d\nu_{\mathbf{k}}\nu_{\mathbf{k}}^3 \to \int_{-\infty}^\infty d\nu_{\mathbf{k}}\omega^3 \tag{3.29}$$

The frequency integral can then be evaluated to be a delta distribution centred around t,

$$\int_{-\infty}^\infty d\nu_{\mathbf{k}} e^{i(\omega-\nu_{\mathbf{k}})(t-t')} = 2\pi\delta(t-t'), \tag{3.30}$$

and the integral up to the centre of a delta distribution is simply a half,

$$\int_0^t dt' \delta(t-t') = \frac{1}{2}. \tag{3.31}$$

Altogether this yields the final result for the spontaneous emission rate, the Einstein A coefficient

$$\gamma = \frac{|\mathbf{d}|^2 \omega_0^3}{3\pi\epsilon_0 \hbar c^3}. \tag{3.32}$$

Chapter 4

Cavity Quantum Electrodynamics

4.1 Quantisation of the Electromagnetic Field

From classical electrodynamics we recall that the total energy of the electromagnetic field is given by

$$H = \frac{1}{2}\int d^3r(\epsilon_0|\mathbf{E}|^2+\frac{1}{\mu_0}|\mathbf{B}|^2), \tag{4.1}$$

where $\mathbf{E}$ is the electric field, $\mathbf{B}$ is the magnetic field, ϵ_0 the electric constant, and μ_0 the magnetic permeability. Assuming we are in vacuum, i.e., no charges or currents, the Maxwell equations are given by

$$\begin{aligned} \nabla\cdot\mathbf{E} &= 0, \\ \nabla\times\mathbf{E} &= -\frac{\partial\mathbf{B}}{\partial t}, \\ \nabla\cdot\mathbf{B} &= 0, \\ \nabla\times\mathbf{B} &= \frac{1}{c}\frac{\partial\mathbf{E}}{\partial t}, \end{aligned} \tag{4.2}$$

where both $\mathbf{E}$ and $\mathbf{B}$ depend on the vector potential $\mathbf{A}$ according to

$$\begin{aligned} \mathbf{E} &= -\frac{\partial \mathbf{A}}{\partial t}, \\ \mathbf{B} &= \nabla \times \mathbf{A}. \end{aligned} \tag{4.3}$$

In the Coulomb gauge, i.e., $\nabla \cdot \mathbf{A} = 0$, and using the Maxwell equations it can be shown that $\mathbf{E}$, $\mathbf{B}$ and $\mathbf{A}$ have to fulfil the wave equation $\frac{1}{c^2}\frac{\partial^2}{\partial t^2}\bullet = \nabla^2 \bullet$. The corresponding solutions can be written as a Fourier expansion of plane waves, e.g., for the vector potential

$$\mathbf{A}(\mathbf{r}, t) = \sum_{\mathbf{k},\lambda} \hat{\epsilon}_{\mathbf{k},\lambda} \frac{\mathcal{E}_{\mathbf{k}}}{\omega_{\mathbf{k}}} (i\alpha_{\mathbf{k},\lambda} e^{-i(\mathbf{k}\cdot\mathbf{r}-\omega_{\mathbf{k}})t} - i\alpha^*_{\mathbf{k},\lambda} e^{i(\mathbf{k}\cdot\mathbf{r}-\omega_{\mathbf{k}})t}), \tag{4.4}$$

where $\mathbf{k}$ is the wave vector, $\hat{\epsilon}_{\mathbf{k},\lambda}$ is the polarisation unit vector, $\mathcal{E}_{\mathbf{k}}$ is the field amplitude, $\omega_{\mathbf{k}}$ is the frequency, λ is the polarisation index and $\alpha_{\mathbf{k},\lambda}$ are the Fourier amplitudes.

If this is continued for $\mathbf{E}$ and $\mathbf{B}$ and plugged into the Hamiltonian, it can be shown that the result is

$$H = \frac{1}{2} \sum_{\mathbf{k},\lambda} \hbar\omega_k (\alpha^*_{\mathbf{k},\lambda}\alpha_{\mathbf{k},\lambda} + \alpha_{\mathbf{k},\lambda}\alpha^*_{\mathbf{k},\lambda}), \tag{4.5}$$

where we have deliberately kept the order of the mode functions $\alpha_{\mathbf{k},\lambda}$ and $\alpha^*_{\mathbf{k},\lambda}$; subsequently we will identify these as the ladder operators $\hat{a}_{\mathbf{k},\lambda}$ and $\hat{a}^\dagger_{\mathbf{k},\lambda}$, respectively. Using the canonical commutation relations

$$\begin{aligned} \left[\hat{a}_{\mathbf{k},\lambda}, \hat{a}^\dagger_{\mathbf{k}',\lambda'}\right] &= \delta_{\mathbf{k},\mathbf{k}'}\delta_{\lambda,\lambda'} \\ \left[\hat{a}_{\mathbf{k},\lambda}, \hat{a}_{\mathbf{k}',\lambda'}\right] &= \left[\hat{a}^\dagger_{\mathbf{k},\lambda}, \hat{a}^\dagger_{\mathbf{k}',\lambda'}\right] = 0, \end{aligned} \tag{4.6}$$

we can bring the Hamiltonian into the typical harmonic oscillator form,

$$\hat{H} = \sum_{\mathbf{k},\lambda} \hbar\omega_{\mathbf{k}} (\hat{a}^{\dagger}_{\mathbf{k},\lambda} \hat{a}_{\mathbf{k},\lambda} + \frac{1}{2}). \tag{4.7}$$

The final result lets us interpret the electromagnetic vacuum as a collection of modes, distinct in frequency, polarization and wave vector, that behave like simple quantum mechanical harmonic oscillators.

In this thesis we will be working with optical cavities in which only one, and on one occasion two, of the modes of the electromagnetic field are relevant. So, unless we are talking about the infinite modes in the environment, we will drop the indices in the photonic operators. Additionally, for brevity, we shall ignore the constant part attributed to vacuum fluctuations of the Hamiltonian since it only corresponds to a global offset that does not affect the overall dynamics. In that case, we can write

$$\hat{H} = \hbar\omega \hat{a}^{\dagger} \hat{a}. \tag{4.8}$$

4.2 Optical Cavities

Optical cavities are the heart of cavity quantum electrodynamics as they provide an environment that enhances the interaction between atoms and light, so here we now give a brief introduction to them [52]. Optical cavities in their simplest form consist of two mirrors facing, and as close to parallel as possible, to each other (see Fig. 4.1). If on top of that the two mirrors are highly reflective, then in that configuration, light will bounce back and forth between the two mirrors for a long time. Light of a given wave length λ will acquire a phase shift

$$\varphi = \frac{4\pi n \ell}{\lambda} \tag{4.9}$$

upon travelling once back and forth between the two mirrors. Here ℓ represents the distance between the two mirrors and n the refractive index inside the cavity.

If this phase shift is an integer multiple of 2π, i.e., ℓ is an integer multiple of $\frac{\lambda}{2n}$, the light will be in phase and interfere constructively, leading to a standing wave and a peak in the cavity transmission. Each scenario of this sort has an associated mode frequency

$$\omega_m = \frac{\varphi}{t} = m\frac{\pi c}{n\ell}. \tag{4.10}$$

These modes are what we shall refer to when we talk about cavity modes. These resonances have a certain linewidth given by

$$\Delta\phi = \frac{2\pi}{\mathfrak{F}}, \tag{4.11}$$

determined by the finesse $\mathfrak{F}$ of the cavity, a figure of merit for the quality of the cavity. The finesse is given by

$$\mathfrak{F} = \frac{\pi(R_1R_2)^{\frac{1}{4}}}{1-\sqrt{R_1R_2}}, \tag{4.12}$$

where the R_i represent the reflectivities of the mirrors. The more finesse the cavity has, the sharper are also the corresponding resonant modes.

Let us now consider a number of photons N. Every $\Delta t = \frac{n\ell}{c}$ we lose $\Delta N = (1-R)N(t)$ (where $R = R_1+R_2$) of our photons via transmission through the mirrors:

$$\dot{N}(t) = -\frac{c(1-R)}{n\ell}N(t) \tag{4.13}$$

with the exponential solution

$$N(t) = N_0 e^{-\kappa t}, \tag{4.14}$$

where

$$\kappa = \frac{c(1-R)}{n\ell} \tag{4.15}$$

is the cavity decay rate or cavity linewidth that determines the time scale on which photons escape the cavity.

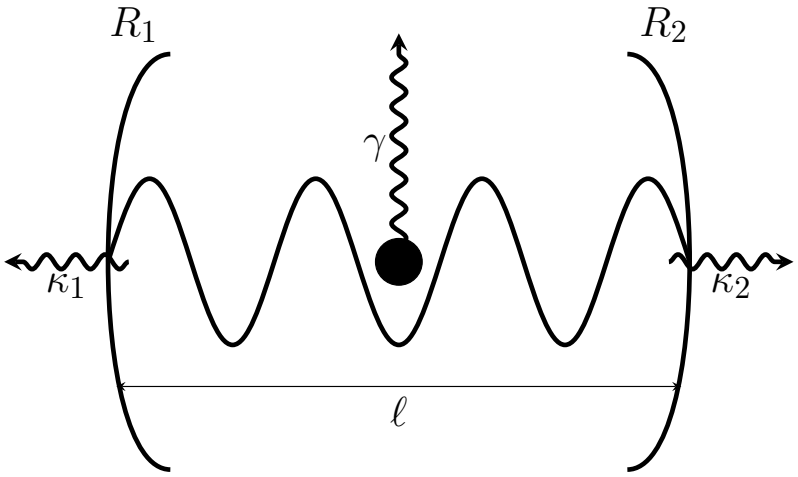

Figure 4.1: Schematic of a one-sided cavity showing input, output and intracavity field. Oftentimes, in the lab, cavities can be made of two mirrors of quite distinct reflectivities R_i (and therefore cavity decay constants κ_i), occasionally, to such a degree that the cavity can be considered one-sided.

The leakage of photons out of the cavity can be described as an interaction of the cavity modes with the infinity of modes of the electromagnetic field external to the cavity (here denoted by the operators $\hat{b}$), completely analogous to spontaneous emission. By starting with a system-bath interaction ($\hbar = 1$)

$$\hat{H}_{SE} = i \int_{-\infty}^{\infty} d\omega \sqrt{\frac{\kappa}{\pi}} (\hat{b}^\dagger(\omega)\hat{a} - \hat{b}(\omega)\hat{a}^\dagger), \tag{4.16}$$

where we assumed a single reservoir and the spectrum of the bath to be independent of frequency, we can describe the situation with the Master equation

$$\dot{\hat{\rho}}_S = -i\Big[\hat{H}_S, \hat{\rho}_S\Big] + \kappa\mathcal{D}[\hat{a}]\hat{\rho}_S. \tag{4.17}$$

4.3 Input-Output Theory

The input-output formalism [53] relates the output of a given open quantum system to its internal dynamics. Consider the cavity interaction that we just introduced in the last Section. This leads to the following quantum Langevin equations

$$\begin{aligned} \dot{\hat{b}} &= -i\omega\hat{b}(\omega,t) + \sqrt{\frac{\kappa}{\pi}}\hat{a} \\ \dot{\hat{a}} &= -i\Big[\hat{a}, \hat{H}_S\Big] - \int_{-\infty}^{\infty} d\omega \sqrt{\frac{\kappa}{\pi}}\hat{b}(\omega,t). \end{aligned} \tag{4.18}$$

We integrate formally the first line from a time $t_0 < t$ to get

$$\hat{b}(\omega,t) = e^{-i\omega(t-t_0)}\hat{b}(\omega,t_0) + \int_{t_0}^{t} dt' \sqrt{\frac{\kappa}{\pi}} e^{-i\omega(t-t')}\hat{a}(t'), \tag{4.19}$$

and substitute it back into the second equation to give

$$\begin{aligned} \dot{\hat{a}} = -i\Big[\hat{a}, \hat{H}\Big] &- \int_{-\infty}^{\infty} d\omega e^{-i\omega(t-t_0)} \sqrt{\frac{\kappa}{\pi}}\hat{b}(\omega,t_0) \\ &- \int_{-\infty}^{\infty} d\omega \frac{\kappa}{\pi} \int_{t_0}^{t} dt' e^{-i\omega(t-t')}\hat{a}(t'). \end{aligned} \tag{4.20}$$

Using the same integral properties as those in Eq. (3.30) and (3.31) we obtain

$$\dot{\hat{a}} = -i\left[\hat{a}, \hat{H}\right] - \kappa\hat{a} + \sqrt{2\kappa}\hat{a}_{\text{in}}, \tag{4.21}$$

where we have defined

$$\hat{a}_{\text{in}} = -\frac{1}{\sqrt{2\pi}} \int_{-\infty}^{\infty} d\omega e^{-i\omega(t-t_0)} \hat{b}(\omega, t_0). \tag{4.22}$$

Integrating towards a larger time $t_1 > t$ yields

$$\dot{\hat{a}} = -i\left[\hat{a}, \hat{H}\right] + \kappa\hat{a} - \sqrt{2\kappa}\hat{a}_{\text{out}} \tag{4.23}$$

where

$$\hat{a}_{\text{out}} = \frac{1}{\sqrt{2\pi}} \int_{-\infty}^{\infty} d\omega e^{-i\omega(t-t_1)} \hat{b}(\omega, t_0). \tag{4.24}$$

Equating the two results in Eq. (4.21) and (4.23) leaves us with the input-output relation

$$\sqrt{2\kappa}\hat{a}(t) = \hat{a}_{\text{in}} + \hat{a}_{\text{out}}, \tag{4.25}$$

which relates the intracavity field to the incoming and outgoing fields at the boundaries of a cavity (see Fig. 4.2).

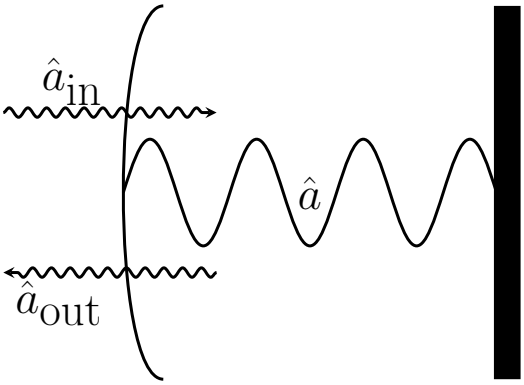

Figure 4.2: Schematic of a one-sided cavity showing input, output and intracavity fields.

4.4 Atoms interacting with Quantum Fields

The coupling of an atom to the cavity follows the same procedure as the one laid out for the interaction with a classical field. So let us consider again the same single spin-$\frac{1}{2}$ atom, but now replace the electric field in the interaction Hamiltonian by the corresponding operator for a quantised single-mode field [54],

$$\mathbf{E} = \hat{\epsilon}\mathcal{E}(\hat{a}f^*(\mathbf{r}) + \hat{a}^\dagger f(\mathbf{r})), \tag{4.26}$$

where the field per photon is given by

$$\mathcal{E} = \sqrt{\frac{\hbar\omega}{2\epsilon_0 \mathcal{V}}}, \tag{4.27}$$

and where $\mathcal{V}$ is the effective mode volume

$$\mathcal{V} = \int |f(\mathbf{r})|^2 d\mathbf{r}. \tag{4.28}$$

This is saying that the smaller the space in which our light modes are confined the stronger the interaction.

Following the same procedure as with the atom interacting with a laser field we can plug our quantum field into Eq. (3.13) and obtain the Rabi model describing the atom-field interaction for a quantised field,

$$\hat{H} = \omega\hat{a}^\dagger\hat{a} + \frac{\omega_0}{2}\hat{\sigma}_z + g(\hat{\sigma}_+ + \hat{\sigma}_-)(\hat{a} + \hat{a}^\dagger), \tag{4.29}$$

where we introduced the single atom coupling strength (assuming f is real)

$$g = -\hat{\epsilon}\cdot\mathbf{d}\mathcal{E}f(\mathbf{r}). \tag{4.30}$$

As one can see, this is pretty much the same form as that of the Rabi frequency, and indeed it is sometimes referred to as the vacuum Rabi frequency. The reason for this is that if one starts with an excited atom in an empty cavity, one can also observe Rabi oscillations between the state where the cavity is in the vacuum and the atom excited, and the state where the atom is in the ground state and a single photon is in the cavity [55].

The interaction part of the Hamiltonian in (4.29) is made up of four terms: $\hat{\sigma}_-\hat{a}$ describing the deexcitation of the atom and the annihilation of a photon, $\hat{a}^\dagger\hat{\sigma}_+$ describing the excitation of the atom and the creation of a photon, $\hat{a}\hat{\sigma}_+$ describing the absorption of a photon by the atom from the field and finally $\hat{a}^\dagger\hat{\sigma}_-$ describing the emission of a photon from the atom into the field.

The first two terms describe the creation and annihilation of two quanta of energy in the system, while the latter two describe the transfer of one quantum of energy from the atom to the field or vice-versa. Thus, these processes are said to be non-energy-conserving and energy-conserving, respectively. In the interaction picture, the two types of terms oscillate on very different time scales,

$$\hat{V} = g(\hat{\sigma}_+\hat{a}e^{-i(\omega-\omega_0)t} + \hat{\sigma}_-\hat{a}e^{-i(\omega+\omega_0)t} + \hat{\sigma}_+\hat{a}^\dagger e^{i(\omega+\omega_0)t} + \hat{\sigma}_-\hat{a}^\dagger e^{i(\omega-\omega_0)t}). \tag{4.31}$$

Assuming that $\omega \approx \omega_0$, we can perform the rotating wave approximation which consists in dropping the fast-oscillating, non-energy-conserving terms (due to them averaging to 0) and we obtain the so-called Jaynes-Cummings Hamiltonian

$$\hat{H} = \omega \hat{a}^\dagger \hat{a} + \frac{\omega_0}{2} \hat{\sigma}_z + g(\hat{a}\hat{\sigma}_+ + \hat{a}^\dagger \hat{\sigma}_-). \tag{4.32}$$

The generalisation of this model to an ensemble of N atoms using collective spin operators brings about the Tavis-Cummings Hamiltonian,

$$\hat{H} = \omega \hat{a}^\dagger \hat{a} + \omega_0 \hat{J}_z + g(\hat{a}\hat{J}_+ + \hat{a}^\dagger \hat{J}_-), \tag{4.33}$$

where again, $\hat{J}_{z,\pm} = \sum_i^N \hat{\sigma}_{z,\pm}^{(i)}$.

4.5 Cooperativity

Together with the previously introduced loss processes of cavity decay and spontaneous emission, we have a full set of channels where energy quanta can be emitted. The coupling strength gives the rate at which an atom emits into the cavity, while the other two channels are into free space. Often times the cooperativity,

$$C = \frac{2g^2}{\gamma\kappa}, \tag{4.34}$$

the ratio of these "good" and "bad" rates, is used as a figure of merit for atom-cavity systems. In particular, if the cooperativity for a system is high and $g > \gamma, \kappa$ we can assume that over short time frames the evolution stays mostly coherent.

4.6 Photon Statistics

The photon statistics, or more exactly the statistics of photon counting, give a lot of information about the nature of the measured light, such as whether it is classical or whether it is quantum. To this end, we introduce the second order (intensity) correlation function for two light fields with annihilation operators $\hat{a}$ and $\hat{b}$

$$G^{(2)}_{ab}(\tau) = \langle \hat{a}^\dagger(t)\hat{b}^\dagger(t+\tau)\hat{b}(t+\tau)\hat{a}(t)\rangle, \tag{4.35}$$

which can be understood as the probability of measuring a photon in mode $\hat{b}$ at time $t+\tau$ after having recorded a photon in mode $\hat{a}$ at time t. It is helpful to normalise the correlation function by the probability of measuring photons in those two modes in the first place; the final result is referred to as the degree of coherence,

$$g^{(2)}_{ab}(\tau) = \frac{\langle \hat{a}^\dagger(t)\hat{b}^\dagger(t+\tau)\hat{b}(t+\tau)\hat{a}(t)\rangle}{\langle \hat{a}^\dagger(t)\hat{a}(t)\rangle\langle \hat{b}^\dagger(t+\tau)\hat{b}(t+\tau)\rangle}. \tag{4.36}$$

For classical fields of intensity I, this corresponds to

$$g^{(2)}_{ab}(\tau) = \frac{\langle I_a(t)I_b(t+\tau)\rangle}{\langle I_a(t)\rangle\langle I_b(t+\tau)\rangle}. \tag{4.37}$$

Let us consider autocorrelations $g^{(2)} = g^{(2)}_{aa}$ for now. We differentiate between three regimes: bunched, coherent and antibunched light. Coherent light is characterised by $g^{(2)} = 1$, which means that photons in such light are somewhat randomly distributed in time. As the name suggests, it is true for coherent states, but also for all states as time approaches $\tau \to \infty$, as the fluctuations become uncorrelated. Light with super-Poissonian statistics has $g^{(2)} > 1$, and photons are more likely to be recorded directly after recording another one, i.e., photons come in bunches. This is true, for example, for thermal states.

Classical light will always fall into one of these two categories as $g^{(2)} \geq 1$ has to hold true, which is a consequence of classical fields adhering to $\langle I^2(t)\rangle - \langle I(t)\rangle^2 \geq 0$ and the Cauchy-Schwarz inequality $\langle I(t)I(t+\tau)\rangle \leq \langle I^2(t)\rangle$, which implies both

$$g^{(2)}(0) \geq 1 \tag{4.38}$$

and

$$g^{(2)}(0) \geq g^{(2)}(\tau), \tag{4.39}$$

respectively. It was also shown [56] that they fulfil

$$|g^{(2)}(0)-1| \geq |g^{(2)}(\tau)-1|. \tag{4.40}$$

For crosscorrelations Eq. (4.38) still holds, but Eq. (4.39) generalises to [57–59]

$$g^{(2)}_{aa}(0)g^{(2)}_{bb}(0) \geq [g^{(2)}_{ab}(\tau)]^2. \tag{4.41}$$

Eq. (4.40) on the other hand can be generalised to

$$\begin{aligned} |g^{(2)}_{ab}(\tau)-1|^2 &= \left|\frac{\langle \Delta I_a(0)\Delta I_b(\tau)\rangle}{\langle I_a\rangle\langle I_b\rangle}\right|^2 \\ &\leq \frac{\langle(\Delta I_a)^2\rangle\langle(\Delta I_b)^2\rangle}{|\langle I_a\rangle\langle I_b\rangle|^2} \\ &= (g^{(2)}_{aa}(0)-1)(g^{(2)}_{bb}(0)-1), \end{aligned} \tag{4.42}$$

using $I(t) = \langle I \rangle_{SS} + \Delta I(t)$, where we rewrite the intensity at a time t in terms of the average $\langle I \rangle_{SS}$ and its deviation from the average, $\Delta I(t)$.

Quantum light can violate these conditions in some way or another, e.g., by displaying sub-Poissonian photon statistics, $g^{(2)} < 1$, where photons are distinctly spaced in time, thus making it less probable to measure two at the same time. It may also display antibunching $g^{(2)}(0) < g^{(2)}(\tau)$. But it may also violate Eq. (4.40) without being antibunched [60].

The correlation function $g^{(2)}(\tau \neq 0)$ cannot be computed like normal single-time expectation values, but rather via the Quantum Regression theorem or via the photocount record from quantum trajectories, which in fact emulates how they are actually determined in an experimental setup.

Chapter 5

An Integer-Spin Dicke Model

5.1 The Dicke model

The Dicke model corresponds to the many-body version of the Rabi model, which for N particles we write as

$$\hat{H} = \omega\hat{a}^\dagger\hat{a} + \omega_0\hat{J}_z + g(\hat{J}_+ + \hat{J}_-)(\hat{a} + \hat{a}^\dagger), \tag{5.1}$$

where again, ω is the frequency of the cavity mode, ω_0 the frequency separation in the atomic two-level system, g the strength of the atom-cavity interaction and $\hat{J}_{z,\pm} = \sum_i^N \hat{\sigma}_{z,\pm}^{(i)}$. This situation arises when either the coupling is very strong, we are far-off resonance, or it is specifically engineered like in this thesis.

Contrary to the Tavis-Cummings model, the Dicke model does not conserve the number of excitations, but rather only the parity of the number of excitations. That is, the Tavis-Cummings terms are number-conserving, whereas the additional terms in the Dicke model change the number by plus or minus two.

The Dicke model was hotly debated due to its predicted superradiant phase transition [61], a regime where the intensity of the cavity field in the steady state becomes proportional to the number of atoms, which in the presence of a finite κ implies a continuous stream of photoemissions from the cavity.

This happens once the coupling strength $\lambda = g\sqrt{N}$ exceeds a certain critical coupling given by

$$\lambda_c = \frac{1}{2}\sqrt{\frac{\omega_0(\omega^2+\kappa^2)}{\omega}}. \tag{5.2}$$

A cavity producing an unlimited amount of energy does not seem physical. It was shown, however, that the steady-state superradiance vanishes if the term proportional to the squared vector potential $\mathbf{A}^2$ in the atom-field Hamiltonian Eq. (3.12) is not omitted [62]. This term can usually be ignored in the rotating wave approximation, but evidently not here when the field is becoming quite strong.

This seeming impossibility to realise the Dicke model experimentally with atoms in a cavity had halted any further interest in it for a while. That is, until schemes were proposed where it was effectively engineered by including external driving fields to manufacture cavity-mediated Raman transitions [63]. Experimental realisation in ensembles of spin-$\frac{1}{2}$ [64] and spin-1 atoms [65] ensued.

In parallel to this, there have also been some efforts to implement the Dicke model in Bose-Einstein condensates [66–70]. In these studies, the role of the internal degree of freedom of the atom is replaced with their motional state. Above the critical coupling, the superradiant phase transition occurs by atoms arranging in a square lattice and emitting in phase into the cavity mode.

5.2 Derivation

We shall demonstrate now the derivation for the $F = 4$ manifold of ^{133}Cs driven via the D_1 line (see Fig. 5.1), although we will try to keep most of the derivation as general as possible. This example was chosen to complement the case of the $F = 1$ manifold of ^{87}Rb also driven via the D_1 line that has been obtained [71, 72], to demonstrate that the same approach also works in another alkaline metal and their upper ground state. We will also use ^{133}Cs for N-photon pulse generation.

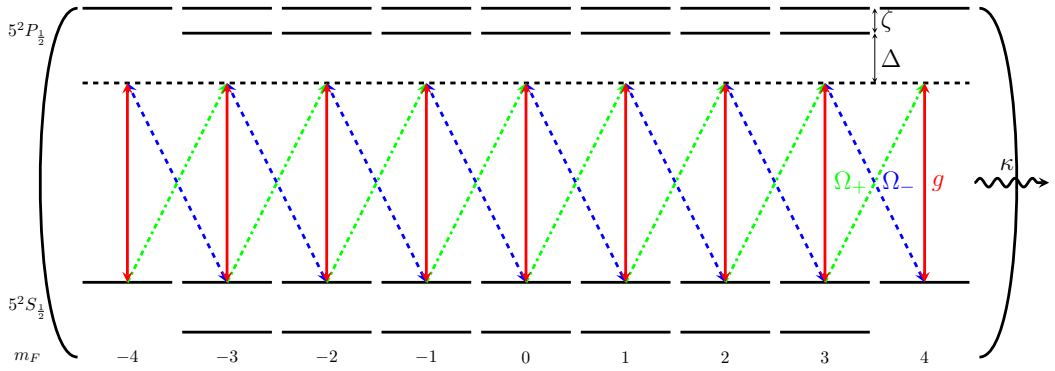

Figure 5.1: Energy level diagram of a D_1 line in ^{133}Cs that yields the Dicke model with $F = 4$. The cavity (red), the σ_-- (blue dashed) and σ_+-polarised laser (green dotdashed) are detuned by an amount Δ with respect to $F = 4 \leftrightarrow F' = 3$.

5.2.1 Hamiltonian

We use the following nomenclature: the F-manifold ground states are labelled by their magnetic quantum number $|m_F\rangle$ and the excited states by $|F', m_{F'}\rangle$; the complete Hamiltonian reads

$$\hat{H} = \hat{H}_0 + \hat{H}_e + \hat{H}_c + \hat{H}_+ + \hat{H}_-, \tag{5.3}$$

where we have the bare cavity mode and atomic ground state Hamiltonian for a single atom ($\hbar = 1$)

$$\hat{H}_0 = \omega_c \hat{a}^\dagger \hat{a} + \omega_z \sum_{m_F} m_F |m_F\rangle\langle m_F|, \tag{5.4}$$

the atomic excited state Hamiltonian

$$\hat{H}_e = \sum_{F'} \sum_{m_{F'}} \omega_{F'} |F', m_{F'}\rangle\langle F', m_{F'}|, \tag{5.5}$$

and the three interaction Hamiltonians $\hat{H}_c$, $\hat{H}_+$ and $\hat{H}_-$ corresponding to the cavity, the σ_+- and the σ_--polarised lasers, respectively:

$$\begin{aligned}\hat{H}_c &= \sum_{F,F'} g\hat{a}^\dagger \hat{D}_0(F,F') + \text{H.c.},\\ \hat{H}_\pm &= \sum_{F,F'} \frac{\Omega_\pm}{2} \hat{D}_{\pm 1}(F,F') + \text{H.c.}.\end{aligned} \tag{5.6}$$

Here we define the atomic dipole transition operators

$$\hat{D}_q(F,F') = \sum_{m_F=-F}^{F} |m_F\rangle\langle m_F|\mu_q|F', m_F+q\rangle\langle F', m_F+q|, \tag{5.7}$$

where $q = 0, \pm 1$ stands for the polarisation of the transition.

5.2.2 Interaction Picture

After moving into the interaction picture of $\hat{H}_0$, the interaction picture Hamiltonian $\hat{V} = \hat{H}_e + \hat{Q} + \hat{Q}^\dagger$ can be split into three parts. The two new parts correspond to projection onto the excited and ground state subspaces of $\hat{V}$, i.e., terms that describe excitation processes ($\hat{Q}$) and deexcitation processes ($\hat{Q}^\dagger$), where $\hat{Q} = \sum \hat{Q}_i$ and the partial operators are given by

$$\begin{aligned}\hat{Q}_c &= e^{-i\omega_c t} \sum_{F,F'} g\hat{a} e^{i\hat{H}_0 t} \hat{D}_0^\dagger(F,F') e^{-i\hat{H}_0 t},\\ \hat{Q}_\pm &= e^{-i\omega_\pm t} \sum_{F,F'} \frac{\Omega_\pm}{2} e^{i\hat{H}_0 t} \hat{D}_{\pm 1}^\dagger(F,F') e^{-i\hat{H}_0 t}.\end{aligned} \tag{5.8}$$

Simultaneously we introduce the related operator $\hat{Q}' = \sum \hat{Q}'_i$ that will be useful in the future:

$$\begin{aligned}\hat{Q}'_c &= e^{-i\omega_c t}\sum_{F,F'}\frac{1}{\omega_c-\omega_{F'}}g\hat{a}e^{i\hat{H}_0 t}\hat{D}_0^\dagger(F,F')e^{-i\hat{H}_0 t}\\ \hat{Q}'_\pm &= e^{-i\omega_\pm t}\sum_{F,F'}\frac{1}{\omega_\pm-\omega_{F'}}\frac{\Omega_\pm}{2}e^{i\hat{H}_0 t}\hat{D}_{\pm1}^\dagger(F,F')e^{-i\hat{H}_0 t}.\end{aligned} \tag{5.9}$$

5.2.3 Adiabatic Elimination of Excited States

In the following, we rewrite the energy differences $\omega_i-\omega_{4'}=\Delta_i$ $(i=c,\pm)$ and $\omega_{4'}-\omega_{3'}=\zeta$.

In the limit where the detunings are large, the excited state is only virtually populated and we can adiabatically eliminate it and compute an effective Hamiltonian through

$$\hat{H}_{\text{eff}} = \frac{1}{2}\left(\hat{Q}^\dagger\hat{Q}'+\hat{Q}'^\dagger\hat{Q}\right) = \sum_{i,j}c_{ij}|i\rangle\langle j|. \tag{5.10}$$

This procedure is equivalent to the effective Lindblad operator formalism [73], indeed $\hat{Q}'$ is the product of $\hat{Q}$ and the inverse excited state Hamiltonian $(\omega_{\pm,c}-\hat{H}_e+i\sum_q\hat{L}_q^\dagger\hat{L}_q)^{-1}$ where the last term (see next section for an explicit formula) from the effect of spontaneous emission is removed, as it will not have a great impact on the coherent dynamics due to the linewidth γ being orders of magnitude smaller than the detunings. We shall revisit spontaneous emission in the next section, where we will derive the effect of it in such a system.

Up to here everything has been kept general, let us now consider specifically the $F=4$ manifold of ^{133}Cs. We obtain the following coefficients for the diagonal elements of the Hamiltonian

$$
\begin{aligned}
c_{44} &= \frac{g^2\hat{a}^\dagger\hat{a}}{3\Delta_c}+\frac{\Omega_-^2}{48\Delta_-}+\frac{7\Omega_-^2}{48(\Delta_-+\zeta)}\\
c_{33} &= \frac{7g^2\hat{a}^\dagger\hat{a}}{48(\Delta_c+\zeta)}+\frac{3g^2\hat{a}^\dagger\hat{a}}{16\Delta_c}+\frac{\Omega_+^2}{48\Delta_+}+\frac{7\Omega_-^2}{64(\Delta_-+\zeta)}+\frac{7\Omega_-^2}{192\Delta_-}\\
c_{22} &= \frac{g^2\hat{a}^\dagger\hat{a}}{4(\Delta_c+\zeta)}+\frac{g^2\hat{a}^\dagger\hat{a}}{12\Delta_c}+\frac{7\Omega_+^2}{192\Delta_+}+\frac{\Omega_+^2}{192(\Delta_++\zeta)}+\frac{5\Omega_-^2}{64(\Delta_-+\zeta)}+\frac{3\Omega_-^2}{64\Delta_-}\\
c_{11} &= \frac{5g^2\hat{a}^\dagger\hat{a}}{16(\Delta_c+\zeta)}+\frac{g^2\hat{a}^\dagger\hat{a}}{48\Delta_c}+\frac{\Omega_+^2}{64(\Delta_++\zeta)}+\frac{3\Omega_+^2}{64\Delta_+}+\frac{5\Omega_-^2}{96(\Delta_-+\zeta)}+\frac{5\Omega_-^2}{96\Delta_-}\\
c_{00} &= \frac{g^2\hat{a}^\dagger\hat{a}}{3(\Delta_c+\zeta)}+\frac{5\Omega_+^2}{96\Delta_+}+\frac{\Omega_+^2}{32(\Delta_++\zeta)}+\frac{5\Omega_-^2}{96\Delta_-}+\frac{\Omega_-^2}{32(\Delta_-+\zeta)}\\
c_{-1-1} &= \frac{5g^2\hat{a}^\dagger\hat{a}}{16(\Delta_c+\zeta)}+\frac{g^2\hat{a}^\dagger\hat{a}}{48\Delta_c}+\frac{\Omega_+^2}{32(\Delta_++\zeta)}+\frac{\Omega_+^2}{32\Delta_+}+\frac{5\Omega_-^2}{64\Delta_-}+\frac{5\Omega_-^2}{192(\Delta_-+\zeta)}\\
c_{-2-2} &= \frac{g^2\hat{a}^\dagger\hat{a}}{4(\Delta_c+\zeta)}+\frac{g^2\hat{a}^\dagger\hat{a}}{12\Delta_c}+\frac{5\Omega_+^2}{64(\Delta_++\zeta)}+\frac{3\Omega_+^2}{64\Delta_+}+\frac{7\Omega_-^2}{192(\Delta_-+\zeta)}+\frac{\Omega_-^2}{192\Delta_-}\\
c_{-3-3} &= \frac{7g^2\hat{a}^\dagger\hat{a}}{48(\Delta_c+\zeta)}+\frac{3g^2\hat{a}^\dagger\hat{a}}{16\Delta_c}+\frac{7\Omega_+^2}{192\Delta_+}+\frac{7\Omega_+^2}{64(\Delta_++\zeta)}+\frac{\Omega_-^2}{48\Delta_-}\\
c_{-4-4} &= \frac{g^2\hat{a}^\dagger\hat{a}}{3\Delta_c}+\frac{\Omega_+^2}{48\Delta_+}+\frac{7\Omega_+^2}{48(\Delta_++\zeta)}
\end{aligned}
\tag{5.11}
$$

and the following off-diagonal coefficients

$$
\begin{aligned}
c_{43} &= \frac{1}{2}\left(e^{i(\omega_- -\omega_c+\omega_z)t}\left(\frac{7\Omega_- g\hat{a}}{48(\Delta_c+\zeta)}-\frac{\Omega_- g\hat{a}}{16\Delta_c}\right)+e^{i(\omega_c-\omega_++\omega_z)t}\frac{\Omega_+ g\hat{a}^\dagger}{12\Delta_+}\right)\\
&+\frac{1}{2}\left(e^{i(\omega_- -\omega_c+\omega_z)t}\left(\frac{7\Omega_- g\hat{a}}{48(\Delta_- +\zeta)}-\frac{\Omega_- g\hat{a}}{16\Delta_-}\right)+e^{i(\omega_c-\omega_++\omega_z)t}\frac{\Omega_+ g\hat{a}^\dagger}{12\Delta_c}\right)\\
c_{32} &= \frac{1}{2}\left(e^{i(\omega_- -\omega_c+\omega_z)t}\left(\frac{\sqrt{7}\Omega_- g\hat{a}}{16(\Delta_c+\zeta)}-\frac{\sqrt{7}\Omega_- g\hat{a}}{48\Delta_c}\right)+e^{i(\omega_c-\omega_++\omega_z)t}\left(\frac{\sqrt{7}\Omega_+ g\hat{a}^\dagger}{32\Delta_+}+\frac{\sqrt{7}\Omega_+ g\hat{a}^\dagger}{96(\Delta_++\zeta)}\right)\right)\\
&+\frac{1}{2}\left(e^{i(\omega_- -\omega_c+\omega_z)t}\left(\frac{\sqrt{7}\Omega_- g\hat{a}}{16(\Delta_- +\zeta)}-\frac{\sqrt{7}\Omega_- g\hat{a}}{48\Delta_-}\right)+e^{i(\omega_c-\omega_++\omega_z)t}\left(\frac{\sqrt{7}\Omega_+ g\hat{a}^\dagger}{32\Delta_c}+\frac{\sqrt{7}\Omega_+ g\hat{a}^\dagger}{96(\Delta_c+\zeta)}\right)\right)\\
c_{21} &= \frac{1}{2}\left(e^{i(\omega_- -\omega_c+\omega_z)t}\left(\frac{5\Omega_- g\hat{a}}{32(\Delta_c+\zeta)}-\frac{\Omega_- g\hat{a}}{32\Delta_c}\right)+e^{i(\omega_c-\omega_++\omega_z)t}\left(\frac{\Omega_+ g\hat{a}^\dagger}{16(\Delta_++\zeta)}+\frac{\Omega_+ g\hat{a}^\dagger}{16\Delta_+}\right)\right)\\
&+\frac{1}{2}\left(e^{i(\omega_- -\omega_c+\omega_z)t}\left(\frac{5\Omega_- g\hat{a}}{32(\Delta_- +\zeta)}-\frac{\Omega_- g\hat{a}}{32\Delta_-}\right)+e^{i(\omega_c-\omega_++\omega_z)t}\left(\frac{\Omega_+ g\hat{a}^\dagger}{16(\Delta_c+\zeta)}+\frac{\Omega_+ g\hat{a}^\dagger}{16\Delta_c}\right)\right)\\
c_{10} &= \frac{1}{2}\left(e^{i(\omega_- -\omega_c+\omega_z)t}\frac{\sqrt{5}\Omega_- g\hat{a}}{12\sqrt{2}(\Delta_c+\zeta)}+e^{i(\omega_c-\omega_++\omega_z)t}\left(\frac{\sqrt{5}\Omega_+ g\hat{a}^\dagger}{16\sqrt{2}(\Delta_++\zeta)}+\frac{\sqrt{5}\Omega_+ g\hat{a}^\dagger}{48\sqrt{2}\Delta_+}\right)\right)\\
&+\frac{1}{2}\left(e^{i(\omega_- -\omega_c+\omega_z)t}\frac{\sqrt{5}\Omega_- g\hat{a}}{12\sqrt{2}(\Delta_- +\zeta)}+e^{i(\omega_c-\omega_++\omega_z)t}\left(\frac{\sqrt{5}\Omega_+ g\hat{a}^\dagger}{16\sqrt{2}(\Delta_c+\zeta)}+\frac{\sqrt{5}\Omega_+ g\hat{a}^\dagger}{48\sqrt{2}\Delta_c}\right)\right)\\
c_{0-1} &= \frac{1}{2}\left(e^{i(\omega_- -\omega_c+\omega_z)t}\left(\frac{\sqrt{5}\Omega_- g\hat{a}}{16\sqrt{2}(\Delta_c+\zeta)}+\frac{\sqrt{5}\Omega_- g\hat{a}}{48\sqrt{2}\Delta_c}\right)+e^{i(\omega_c-\omega_++\omega_z)t}\frac{\sqrt{5}\Omega_+ g\hat{a}^\dagger}{12\sqrt{2}(\Delta_++\zeta)}\right)\\
&+\frac{1}{2}\left(e^{i(\omega_- -\omega_c+\omega_z)t}\left(\frac{\sqrt{5}\Omega_- g\hat{a}}{16\sqrt{2}(\Delta_- +\zeta)}+\frac{\sqrt{5}\Omega_- g\hat{a}}{48\sqrt{2}\Delta_-}\right)+e^{i(\omega_c-\omega_++\omega_z)t}\frac{\sqrt{5}\Omega_+ g\hat{a}^\dagger}{12\sqrt{2}(\Delta_c+\zeta)}\right)\\
c_{-1-2} &= \frac{1}{2}\left(e^{i(\omega_- -\omega_c+\omega_z)t}\left(\frac{\Omega_- g\hat{a}}{16(\Delta_c+\zeta)}+\frac{\Omega_- g\hat{a}}{16\Delta_c}\right)+e^{i(\omega_c-\omega_++\omega_z)t}\left(\frac{5\Omega_+ g\hat{a}^\dagger}{32(\Delta_++\zeta)}-\frac{\Omega_+ g\hat{a}^\dagger}{32\Delta_+}\right)\right)\\
&+\frac{1}{2}\left(e^{i(\omega_- -\omega_c+\omega_z)t}\left(\frac{\Omega_- g\hat{a}}{16(\Delta_- +\zeta)}+\frac{\Omega_- g\hat{a}}{16\Delta_-}\right)+e^{i(\omega_c-\omega_++\omega_z)t}\left(\frac{5\Omega_+ g\hat{a}^\dagger}{32(\Delta_c+\zeta)}-\frac{\Omega_+ g\hat{a}^\dagger}{32\Delta_c}\right)\right)\\
c_{-2-3} &= \frac{1}{2}\left(e^{i(\omega_- -\omega_c+\omega_z)t}\left(\frac{\sqrt{7}\Omega_- g\hat{a}}{32\Delta_c}+\frac{\sqrt{7}\Omega_- g\hat{a}}{96(\Delta_c+\zeta)}\right)+e^{i(\omega_c-\omega_++\omega_z)t}\left(\frac{\sqrt{7}\Omega_+ g\hat{a}^\dagger}{16(\Delta_++\zeta)}-\frac{\sqrt{7}\Omega_+ g\hat{a}^\dagger}{48\Delta_+}\right)\right)\\
&+\frac{1}{2}\left(e^{i(\omega_- -\omega_c+\omega_z)t}\left(\frac{\sqrt{7}\Omega_- g\hat{a}}{32\Delta_-}+\frac{\sqrt{7}\Omega_- g\hat{a}}{96(\Delta_- +\zeta)}\right)+e^{i(\omega_c-\omega_++\omega_z)t}\left(\frac{\sqrt{7}\Omega_+ g\hat{a}^\dagger}{16(\Delta_c+\zeta)}-\frac{\sqrt{7}\Omega_+ g\hat{a}^\dagger}{48\Delta_c}\right)\right)\\
c_{-3-4} &= \frac{1}{2}\left(e^{i(\omega_- -\omega_c+\omega_z)t}\frac{\Omega_- g\hat{a}}{12\Delta_c}+e^{i(\omega_c-\omega_++\omega_z)t}\left(\frac{7\Omega_+ g\hat{a}^\dagger}{48(\Delta_++\zeta)}-\frac{\Omega_+ g\hat{a}^\dagger}{16\Delta_+}\right)\right)\\
&+\frac{1}{2}\left(e^{i(\omega_- -\omega_c+\omega_z)t}\frac{\Omega_- g\hat{a}}{12\Delta_-}+e^{i(\omega_c-\omega_++\omega_z)t}\left(\frac{7\Omega_+ g\hat{a}^\dagger}{48(\Delta_c+\zeta)}-\frac{\Omega_+ g\hat{a}^\dagger}{16\Delta_c}\right)\right),
\end{aligned}
\tag{5.12}
$$

and

$$
\begin{aligned}
c_{42} = c_{-2-4} &= \frac{1}{2}e^{i(\omega_- - \omega_+ + 2\omega_z)t}\frac{\sqrt{7}\Omega_+\Omega_-}{24}\left(\frac{1}{\Delta_+ + \zeta} - \frac{1}{\Delta_+}\right) \\
&+ \frac{1}{2}e^{i(\omega_- - \omega_+ + 2\omega_z)t}\frac{\sqrt{7}\Omega_+\Omega_-}{24}\left(\frac{1}{\Delta_- + \zeta} - \frac{1}{\Delta_-}\right) \\
c_{31} = c_{-1-3} &= \frac{1}{2}e^{i(\omega_- - \omega_+ + 2\omega_z)t}\frac{\sqrt{7}\Omega_+\Omega_-}{16}\left(\frac{1}{\Delta_+ + \zeta} - \frac{1}{\Delta_+}\right) \\
&+ \frac{1}{2}e^{i(\omega_- - \omega_+ + 2\omega_z)t}\frac{\sqrt{7}\Omega_+\Omega_-}{16}\left(\frac{1}{\Delta_- + \zeta} - \frac{1}{\Delta_-}\right) \\
c_{20} = c_{0-2} &= \frac{1}{2}e^{i(\omega_- - \omega_+ + 2\omega_z)t}\frac{\sqrt{5}\Omega_+\Omega_-}{8\sqrt{2}}\left(\frac{1}{\Delta_+ + \zeta} - \frac{1}{\Delta_+}\right) \\
&+ \frac{1}{2}e^{i(\omega_- - \omega_+ + 2\omega_z)t}\frac{\sqrt{5}\Omega_+\Omega_-}{8\sqrt{2}}\left(\frac{1}{\Delta_- + \zeta} - \frac{1}{\Delta_-}\right) \\
c_{1-1} &= \frac{1}{2}e^{i(\omega_- - \omega_+ + 2\omega_z)t}\frac{5\Omega_+\Omega_-}{96}\left(\frac{1}{\Delta_+ + \zeta} - \frac{1}{\Delta_+}\right) \\
&+ \frac{1}{2}e^{i(\omega_- - \omega_+ + 2\omega_z)t}\frac{5\Omega_+\Omega_-}{96}\left(\frac{1}{\Delta_- + \zeta} - \frac{1}{\Delta_-}\right).
\end{aligned}
\tag{5.13}
$$

The inverse coefficients are of course just the Hermitian conjugates ($c_{i,j} = c_{j,i}^\dagger$). For the terms corresponding to the off-diagonal terms of the Hamiltonian, the first lines corresponds to the contribution from $\hat{Q}^\dagger\hat{Q}'$ and the second one to ${\hat{Q}'}^\dagger\hat{Q}$. As one can see, those are basically identical, with the only difference being the detuning changing to the respective other field contributing to that Raman transition, i.e., Δ_c replacing Δ_+, and Δ_- replacing Δ_c for the terms corresponding to $c_{i,i-1}$ and Δ_- replacing Δ_+ each other for the terms corresponding to $c_{i,i-2}$.

Note: in the previous derivation of the Dicke model in [72], solely $\hat{H}_{\text{eff}} = \hat{Q}^\dagger\hat{Q}'$ was used, which leads to a non-Hermitian variant. In that case, the coefficients are just one of the lines of our coefficients. This, however, ends up being inconsequential, as they were operating in a regime where the non-Hermiticity vanishes, i.e., when all fields and therefore detunings are equal. Ultimately, we will also choose this limit.

All time dependence in the effective Hamiltonian is now being eliminated by transforming with

$$\hat{H}_T = \left(-\omega_c + \frac{\omega_+ + \omega_-}{2}\right)\hat{a}^\dagger\hat{a} + \left(-\omega_z + \frac{\omega_+ - \omega_-}{2}\right)\hat{S}_z, \tag{5.14}$$

where

$$\hat{S}_z = \sum_{m_F} m_F |m_F\rangle\langle m_F|. \tag{5.15}$$

After the removal of the global offset

$$\Xi = \frac{5\Omega_+^2}{96\Delta_+} + \frac{\Omega_+^2}{32(\Delta_+ + \zeta)} + \frac{5\Omega_-^2}{96\Delta_-} + \frac{\Omega_-^2}{32(\Delta_- + \zeta)}, \tag{5.16}$$

and setting the various detunings to be equal, $\Delta_c = \Delta_+ = \Delta_- = \Delta$, we can rewrite the Hamiltonian as

$$\begin{aligned}\hat{H} = {} & \omega\hat{a}^\dagger\hat{a} + \omega_0\hat{S}_z + \omega_q\hat{S}_z^2 + \frac{\delta_q}{2}\hat{S}_z^2\hat{a}^\dagger\hat{a} + \frac{\lambda_1}{\sqrt{2}}\left(\hat{S}_+\hat{a} + \hat{S}_-\hat{a}^\dagger\right) + \frac{\lambda_2}{\sqrt{2}}\left(\hat{S}_-\hat{a} + \hat{S}_+\hat{a}^\dagger\right) \\ & + \xi_1\hat{Q}_{xz}\left(\hat{a} + \hat{a}^\dagger\right) + \xi_2\hat{Q}_{yz}\left(\hat{a} - \hat{a}^\dagger\right) + h_+\hat{S}_+^2 + h_-\hat{S}_-^2,\end{aligned} \tag{5.17}$$

where

$$\hat{S}_\pm = \sum_{m_F} \sqrt{F(F+1) - m_F(m_F \pm 1)}\,|m_F \pm 1\rangle\langle m_F|. \tag{5.18}$$

and the $\hat{Q}_{ij}$ operators are the nematic tensors

$$\hat{Q}_{ij} = \hat{S}_i\hat{S}_j + \hat{S}_j\hat{S}_i - \frac{4}{3}\delta_{ij}, \tag{5.19}$$

and we have identified the following parameters

$$\omega = \frac{g^2}{3(\Delta+\zeta)} + \omega_c - \frac{\omega_+ + \omega_-}{2}, \tag{5.20}$$

$$\omega_0 = \frac{\Omega_+^2 - \Omega_-^2}{384}\left(\frac{9}{\Delta+\zeta} - \frac{1}{\Delta}\right), \tag{5.21}$$

$$\omega_q = \frac{\Omega_+^2 + \Omega_-^2}{384}\left(\frac{1}{\Delta+\zeta} - \frac{1}{\Delta}\right), \tag{5.22}$$

$$\delta_q = \frac{g^2}{24}\left(\frac{1}{\Delta} - \frac{1}{\Delta+\zeta}\right), \tag{5.23}$$

$$\lambda_1 = \frac{\Omega_- g}{192}\left(\frac{1}{\Delta} + \frac{7}{\Delta+\zeta}\right), \tag{5.24}$$

$$\lambda_2 = \frac{\Omega_+ g}{192}\left(\frac{1}{\Delta} + \frac{7}{\Delta+\zeta}\right), \tag{5.25}$$

$$\zeta_1 = \frac{\Omega_+ g}{192}\left(\frac{1}{\Delta} - \frac{1}{\Delta+\zeta}\right) + \frac{\Omega_- g}{192}\left(\frac{1}{\Delta+\zeta} - \frac{1}{\Delta}\right), \tag{5.26}$$

$$\zeta_2 = \frac{\Omega_+ g}{192}\left(\frac{1}{\Delta+\zeta} - \frac{1}{\Delta}\right) + \frac{\Omega_- g}{192}\left(\frac{1}{\Delta+\zeta} - \frac{1}{\Delta}\right), \tag{5.27}$$

$$h = \frac{\Omega_+\Omega_-}{384}\left(\frac{1}{\Delta_+ + \zeta} - \frac{1}{\Delta_+}\right). \tag{5.28}$$

5.2.4 Large Detuning Limit

Finally, we assume that the detuning is much larger than the excited state manifold energy splitting $\Delta \gg \zeta$ which removes all the terms that are not found in the standard Dicke model so that the Hamiltonian reduces to

$$\hat{H} = \omega\hat{a}^\dagger\hat{a} + \omega_0\hat{S}_z + \frac{\lambda_1}{\sqrt{2}}\left(\hat{S}_+\hat{a} + \hat{S}_-\hat{a}^\dagger\right) + \frac{\lambda_2}{\sqrt{2}}\left(\hat{S}_-\hat{a} + \hat{S}_+\hat{a}^\dagger\right), \tag{5.29}$$

with

$$\begin{aligned}\omega &= \frac{g^2}{3\Delta}+\omega_c-\frac{\omega_+ +\omega_-}{2},\\ \omega_0 &= -\frac{\Omega_+^2-\Omega_-^2}{48\Delta}+\omega_z-\frac{\omega_+ -\omega_-}{2},\\ \lambda_1 &= \frac{\Omega_- g}{24\Delta},\\ \lambda_2 &= \frac{\Omega_+ g}{24\Delta}.\end{aligned} \tag{5.30}$$

5.2.5 Other F-Levels/Atoms

For the sake of completeness, we want to also give the Dicke models for the $F = 3$ manifold in ^{133}Cs

$$\begin{aligned}\omega &= \frac{g^2}{3\Delta}+\omega_c-\frac{\omega_+ +\omega_-}{2},\\ \omega_0 &= \frac{\Omega_+^2-\Omega_-^2}{48\Delta}+\omega_z-\frac{\omega_+ -\omega_-}{2},\\ \lambda_1 &= -\frac{\Omega_- g}{24\Delta},\\ \lambda_2 &= -\frac{\Omega_+ g}{24\Delta},\end{aligned} \tag{5.31}$$

for the $F = 2$ manifold in ^{87}Rb

$$\begin{aligned}\omega &= \frac{g^2}{3\Delta}+\omega_c-\frac{\omega_+ +\omega_-}{2},\\ \omega_0 &= -\frac{\Omega_+^2-\Omega_-^2}{24\Delta}+\omega_z-\frac{\omega_+ -\omega_-}{2},\\ \lambda_1 &= \frac{\Omega_- g}{12\Delta},\\ \lambda_2 &= \frac{\Omega_+ g}{12\Delta}.\end{aligned} \tag{5.32}$$

and for the $F = 1$ manifold in ^{87}Rb

$$\begin{aligned}\omega &= \frac{g^2}{3\Delta} + \omega_c - \frac{\omega_+ + \omega_-}{2},\\ \omega_0 &= \frac{\Omega_+^2 - \Omega_-^2}{24\Delta} + \omega_z - \frac{\omega_+ - \omega_-}{2},\\ \lambda_1 &= -\frac{\Omega_- g}{12\Delta},\\ \lambda_2 &= -\frac{\Omega_+ g}{12\Delta}.\end{aligned} \tag{5.33}$$

At times, we will extract a factor S out of the coupling strengths $\lambda_\pm$ to normalise the edge transition of the spin operator $\hat{S}_\pm$ to unity to make relative strengths between models (especially for growing atom number) more apparent, i.e,

$$\hat{H} = \omega \hat{a}^\dagger \hat{a} + \omega_0 \hat{\sigma}_z + \frac{\lambda_-}{\sqrt{2S}}\left(\hat{S}_+ \hat{a} + \hat{S}_- \hat{a}^\dagger\right) + \frac{\lambda_+}{\sqrt{2S}}\left(\hat{S}_- \hat{a} + \hat{S}_+ \hat{a}^\dagger\right), \tag{5.34}$$

with

$$\lambda_\pm = \lambda_{1/2}\sqrt{S}. \tag{5.35}$$

5.3 Modelling Spontaneous Emission

The adiabatic elimination of the excited states can be extended to incorporate effects of spontaneous emission in a way that is compatible with the effective Tavis-Cummings model. To do this, we use again the effective Lindblad operator formalism described in [73], but this time actually for the Lindblad operators. Note that the cavity decay remains unchanged. Since the simple Tavis-Cummings model ignores the lower hyperfine ground state, we shall also

ignore decay to this state. The new effective spontaneous emission operators,

$$\hat{\mathscr{L}}_q = \hat{L}_q \hat{Q}', \tag{5.36}$$

include a dissipative part $\hat{L}_q$ corresponding to the normal spontaneous emission operator for the different polarisations from the full model,

$$\hat{L}_q = \sqrt{\frac{\gamma}{2}} \sum_{F,F'} \hat{D}_q(F, F'), \tag{5.37}$$

and the coherent part $\hat{Q}'$ we introduced in the last section corresponding to the interaction part of $\hat{H}_\pm$ responsible for the excitations from the ground state to the excited state prior to the collapse.

5.4 Engineering of Collisional Dynamics for an Ensemble of Atoms

5.4.1 Many-body Hamiltonian

Now we shall consider the case of an ensemble of N atoms. We start by reformulating the Hamiltonian in terms of collective spin operators, i.e.

$$\begin{aligned} \hat{H} &= \omega \hat{a}^\dagger \hat{a} + \sum_i^N \left(\omega_0 \hat{S}_z^{(i)} + \frac{\lambda_1}{\sqrt{2}} (\hat{S}_+^{(i)} \hat{a} + \hat{S}_-^{(i)} \hat{a}^\dagger) + \frac{\lambda_2}{\sqrt{2}} (\hat{S}_-^{(i)} \hat{a} + \hat{S}_+^{(i)} \hat{a}^\dagger) \right) \\ &= \omega \hat{a}^\dagger \hat{a} + \omega_0 \hat{J}_z + \frac{\lambda_-}{\sqrt{2NS}} (\hat{J}_+ \hat{a} + \hat{J}_- \hat{a}^\dagger) + \frac{\lambda_+}{\sqrt{2NS}} (\hat{J}_- \hat{a} + \hat{J}_+ \hat{a}^\dagger), \end{aligned} \tag{5.38}$$

which for an ensemble of spin-1 particles updates the parameters from Eq. (5.33) to

$$\begin{aligned}\omega &= \frac{Ng^2}{3\Delta}+\omega_c-\frac{\omega_+ +\omega_-}{2}\\ \omega_0 &= -\frac{\Omega_+^2-\Omega_-^2}{24\Delta}+\omega_z-\frac{\omega_+-\omega_-}{2}\\ \lambda_- &= \frac{\sqrt{N}\Omega_- g}{12\Delta}\\ \lambda_+ &= \frac{\sqrt{N}\Omega_+ g}{12\Delta}.\end{aligned} \tag{5.39}$$

5.4.2 Adiabatic Elimination of the Bosonic Mode

We move into the interaction picture

$$\hat{\rho}'(t) = e^{i(\omega\hat{a}^\dagger\hat{a}+\omega_0\hat{S}_z)t}\hat{\rho}(t)e^{-i(\omega\hat{a}^\dagger\hat{a}+\omega_0\hat{S}_z)t} \tag{5.40}$$

which yields the interaction picture Hamiltonian

$$\hat{H}_I(t) = \hat{a}e^{-i\omega t}\hat{X}(t)+\hat{a}^\dagger e^{i\omega t}\hat{X}^\dagger(t), \tag{5.41}$$

where

$$\hat{X}(t) = \frac{\lambda_-}{\sqrt{2S}}\hat{J}_- e^{-i\omega_0 t}+\frac{\lambda_+}{\sqrt{2S}}\hat{J}_+ e^{i\omega_0 t}. \tag{5.42}$$

Under the assumption that $\sqrt{\omega^2+\kappa^2} \gg \omega_0, \lambda_\pm$, we expand to second order in the interaction Hamiltonian and trace out the bosonic environment E as

follows,

$$
\begin{aligned}
\dot{\hat{\rho}}'_S &= -\int_0^t dt' \mathrm{Tr}_E\Big(\Big[\hat{H}_I, e^{\mathcal{L}_E(t-t')}\Big[\hat{H}_I(t'), \hat{\rho}'_S \otimes \hat{\rho}'_E(t')\Big]\Big]\Big) \\
&= -\int_0^t dt' \hat{X}^\dagger(t)\hat{X}(t')\hat{\rho}'_S(t')\mathrm{Tr}_E\Big[\hat{a}e^{\mathcal{L}_E(t-t')}\big(\hat{a}^\dagger\hat{\rho}'_E(t')\big)\Big]e^{-i\omega(t-t')} \\
&-\hat{X}^\dagger(t)\hat{\rho}'_S(t')\hat{X}(t')\mathrm{Tr}_E\Big[\hat{a}e^{\mathcal{L}_E(t-t')}\big(\hat{\rho}'_E(t')\hat{a}^\dagger\big)\Big]e^{-i\omega(t-t')} \\
&-\hat{X}(t')\hat{\rho}'_S(t')\hat{X}^\dagger(t)\mathrm{Tr}_E\Big[\hat{a}e^{\mathcal{L}_E(t-t')}\big(\hat{a}^\dagger\hat{\rho}'_E(t')\big)\Big]e^{-i\omega(t-t')} \\
&+\hat{\rho}'_S(t')\hat{X}(t')\hat{X}^\dagger(t)\mathrm{Tr}_E\Big[\hat{a}e^{\mathcal{L}_E(t-t')}\big(\hat{\rho}'_E(t')\hat{a}^\dagger\big)\Big]e^{-i\omega(t-t')} \\
&+\hat{X}(t)\hat{X}^\dagger(t')\hat{\rho}'_S(t')\mathrm{Tr}_E\Big[\hat{a}^\dagger e^{\mathcal{L}_E(t-t')}\big(\hat{a}\hat{\rho}'_E(t')\big)\Big]e^{i\omega(t-t')} \\
&-\hat{X}(t)\hat{\rho}'_S(t')\hat{X}^\dagger(t')\mathrm{Tr}_E\Big[\hat{a}^\dagger e^{\mathcal{L}_E(t-t')}\big(\hat{\rho}'_E(t')\hat{a}\big)\Big]e^{i\omega(t-t')} \\
&-\hat{X}^\dagger(t')\hat{\rho}'_S(t')\hat{X}(t)\mathrm{Tr}_E\Big[\hat{a}^\dagger e^{\mathcal{L}_E(t-t')}\big(\hat{a}\hat{\rho}'_E(t')\big)\Big]e^{i\omega(t-t')} \\
&+\hat{\rho}'_S(t')\hat{X}^\dagger(t')\hat{X}(t)\mathrm{Tr}_E\Big[\hat{a}^\dagger e^{\mathcal{L}_E(t-t')}\big(\hat{\rho}'_E(t')\hat{a}\big)\Big]e^{i\omega(t-t')}
\end{aligned}
\tag{5.43}
$$

where we eliminated terms proportional to $\hat{a}\hat{a}$ and $\hat{a}^\dagger\hat{a}^\dagger$ because their expectation value for a thermal state is zero. Next of, we can assume that the system dynamics are slow when compared to relaxation time of the bosonic mode and set $t' \to t$ in all operators acting on the system only.

By assuming that the environment E is in a thermal state we can replace the following terms

$$\begin{aligned}
\mathrm{Tr}_E\Big[\hat{a}e^{\mathcal{L}_E(t-t')}\big(\hat{a}^\dagger\hat{\rho}'_E(t')\big)\Big] &= (\bar{\mathfrak{n}}+1)e^{-\kappa(t-t')}\\
\mathrm{Tr}_E\Big[\hat{a}e^{\mathcal{L}_E(t-t')}\big(\hat{\rho}'_E(t')\hat{a}^\dagger\big)\Big] &= \bar{\mathfrak{n}}e^{-\kappa(t-t')}\\
\mathrm{Tr}_E\Big[\hat{a}^\dagger e^{\mathcal{L}_E(t-t')}\big(\hat{a}\hat{\rho}'_E(t')\big)\Big] &= \bar{\mathfrak{n}}e^{-\kappa(t-t')}\\
\mathrm{Tr}_E\Big[\hat{a}^\dagger e^{\mathcal{L}_E(t-t')}\big(\hat{\rho}'_E(t')\hat{a}\big)\Big] &= (\bar{\mathfrak{n}}+1)e^{-\kappa(t-t')}.
\end{aligned} \tag{5.44}$$

Evaluating the integral for a large time t we get

$$\int_0^t dt' e^{-(\kappa\pm i\omega)(t-t')} = \frac{1}{\kappa\pm i\omega}\big(1-e^{-(\kappa\pm i\omega)t}\big) \approx \frac{1}{\kappa\pm i\omega}. \tag{5.45}$$

After rotating back to the Schrödinger picture this leaves us with

$$\begin{aligned}
\dot{\hat{\rho}}_S &= -i\Big[\hat{H},\hat{\rho}_S\Big]\\
&+(\bar{\mathfrak{n}}+1)\bigg(-\frac{1}{\kappa+i\omega}\hat{X}^\dagger\hat{X}\hat{\rho}_S+\frac{1}{\kappa+i\omega}\hat{X}\hat{\rho}_S\hat{X}^\dagger+\frac{1}{\kappa-i\omega}\hat{X}\hat{\rho}_S\hat{X}^\dagger-\frac{1}{\kappa-i\omega}\hat{\rho}_S\hat{X}^\dagger\hat{X}\bigg)\\
&+\bar{\mathfrak{n}}\bigg(-\frac{1}{\kappa-i\omega}\hat{X}\hat{X}^\dagger\hat{\rho}_S+\frac{1}{\kappa+i\omega}\hat{X}^\dagger\hat{\rho}_S\hat{X}+\frac{1}{\kappa-i\omega}\hat{X}^\dagger\hat{\rho}_S\hat{X}-\frac{1}{\kappa+i\omega}\hat{\rho}_S\hat{X}\hat{X}^\dagger\bigg)\\
&= -i\Big[\hat{H},\hat{\rho}_S\Big]+\frac{\kappa(\bar{\mathfrak{n}}+1)}{\omega^2+\kappa^2}\Big(2\hat{X}\hat{\rho}_S\hat{X}^\dagger-\hat{X}^\dagger\hat{X}\hat{\rho}_S-\hat{\rho}_S\hat{X}^\dagger\hat{X}\Big)\\
&+\frac{\kappa\bar{\mathfrak{n}}}{\omega^2+\kappa^2}\Big(2\hat{X}^\dagger\hat{\rho}_S\hat{X}-\hat{X}\hat{X}^\dagger\hat{\rho}_S-\hat{\rho}_S\hat{X}\hat{X}^\dagger\Big),
\end{aligned} \tag{5.46}$$

where

$$\hat{H} = \omega_0\hat{J}_z-\frac{\omega(\bar{\mathfrak{n}}+1)}{\omega^2+\kappa^2}\hat{X}^\dagger\hat{X}+\frac{\omega\bar{\mathfrak{n}}}{\omega^2+\kappa^2}\hat{X}\hat{X}^\dagger \tag{5.47}$$

and

$$\hat{X} = \frac{\lambda_-}{\sqrt{2S}}\hat{J}_- + \frac{\lambda_+}{\sqrt{2S}}\hat{J}_+. \tag{5.48}$$

Chapter 6

Reconstructing Quantum States of Light

6.1 Temporal Modes

Optical homodyne detection allows us to measure a set of marginals of the Wigner function of a field mode for a set of different angles θ by scanning the phase of the local oscillator. The quantum state of interest occupying the quantum pulse output from a cavity can be associated to a temporal mode [74] bosonic annihilation operator

$$\hat{A} = \int_0^\infty dt f(t) \hat{a}_{\text{out}}(t), \tag{6.1}$$

with the output field of the cavity $\hat{a}_{\text{out}}$ and the normalisation

$$\int_0^\infty |f(t)|^2 dt = 1, \tag{6.2}$$

so that the filtered mode obeys the bosonic commutation relation

$$\left[\hat{A}, \hat{A}^\dagger\right] = 1. \tag{6.3}$$

Since we want to mode match to a field amplitude the natural choice for the filter function is the normalised amplitude correlation function

$$f(t) = \frac{\langle \hat{a}^\dagger(\epsilon)\hat{a}(t)\rangle}{\sqrt{\int_\epsilon^T dt' |\langle \hat{a}^\dagger(\epsilon)\hat{a}(t')\rangle|^2}}, \tag{6.4}$$

which is related to the power spectrum P via the Fourier transform

$$P(\nu) = \int_{-\infty}^{\infty} \langle \hat{a}^\dagger(\epsilon)\hat{a}(t)\rangle e^{-i\nu t} dt. \tag{6.5}$$

In the next Chapters the initial state will always be the vacuum state. Therefore, we start an infinitesimal time ϵ after 0, after the initial transient rise in cavity population, otherwise the filter would just be zero

$$\langle \hat{a}^\dagger(0)\hat{a}(t)\rangle = \mathrm{Tr}\{\hat{a}e^{\mathcal{L}t}[\underbrace{\rho(0)\hat{a}^\dagger}_{=0}]\} = 0. \tag{6.6}$$

Finally, we obtain a single measurement of the rotated quadrature by integrating the photocurrent of a single trajectory over time after applying the time filter,

$$[x_\theta]_i = \int_0^T dt f(t) I(t). \tag{6.7}$$

Experimentally, the filter can be implemented by giving the local oscillator a similar temporal profile.

6.2 Radon Transform

The Radon transform $\mathcal{R}(x_\theta, \theta)$ [75] of the Wigner distribution $W(x, y)$ is a marginal distribution,

$$\begin{aligned}\mathcal{R}(x_\theta,\theta)[W(x,y)] &= \int_{-\infty}^{\infty}\int_{-\infty}^{\infty} W(x,y)\delta(x_\theta - x\cos\theta - y\sin\theta)dxdy \\ &= \int_{-\infty}^{\infty} W(x_\theta\cos\theta - y_\theta\sin\theta, x_\theta\sin\theta + y_\theta\cos\theta)dy_\theta \\ &= \langle x_\theta|\hat{\rho}|x_\theta\rangle.\end{aligned} \tag{6.8}$$

As we measure these marginals in our simulations we may reconstruct the Wigner distribution by employing the inverse Radon transform, more specifically a filtered back-projection algorithm.

6.3 Balanced Homodyne Detection

In balanced homodyne detection [76] the cavity output field is overlapped at a 50/50 beamsplitter with a strong and resonant local oscillator field, i.e., a large coherent state of amplitude $|\epsilon|e^{i\theta}$. The difference in photon counts between the two beamsplitter outputs is then proportional to

$$\Delta n = |\epsilon|\Big(\sqrt{2\kappa}\langle\hat{a}^\dagger e^{i\theta} + \hat{a}e^{-i\theta}\rangle\Delta t + \Delta W\Big), \tag{6.9}$$

which is directly proportional to the expectation value of the quadrature $\hat{x}_\theta = \hat{a}^\dagger e^{i\theta} + \hat{a}e^{-i\theta}$, while $\Delta W = \sqrt{\Delta t}\mathcal{N}(0,1)$ is a Wiener noise increment accounting for detector shot noise, where $\mathcal{N}(0,1)$ is a normally-distributed number with mean 0 and variance 1.

The continuous detection of the output field is modelled with a stochastic Schrödinger equation [77] which evolves the wave function between quantum

jumps with the propagator

$$\hat{U} = 1 - i\hat{H}_B\Delta t + \sqrt{2\kappa}\frac{\Delta n}{|\epsilon|}e^{-i\theta}\hat{a} + \mathcal{O}(\Delta t^2), \tag{6.10}$$

where $\hat{H}_B$ is the non-Hermitian Hamiltonian from the quantum jump method. For a detector with bandwidth Γ, the (scaled) photocurrent obeys

$$\Delta I(t) = -\Gamma\left(I(t)\Delta t - \frac{\Delta n}{|\epsilon|}\right). \tag{6.11}$$

For our simulations, we consider the bandwidth to be large, e.g., $\Gamma \approx \frac{1}{\Delta t}$.

6.4 Maximum Likelihood Estimation for Quantum States

With maximum likelihood estimation [78, 79] we are trying to find the density operator that is most likely to generate our set of N_θ measured marginals. For this we start with an initial guess $\hat{\rho}_0 = \mathbb{1}_5/5$ (specifically for our purposes of $N = 4$-photon pulses the Hilbert space is truncated to $|4\rangle$) and iterate like so,

$$\hat{\rho}_{k+1} = \frac{\hat{R}\hat{\rho}_k\hat{R}}{\mathrm{Tr}(\hat{R}\hat{\rho}_k\hat{R})}, \tag{6.12}$$

where

$$\hat{R} = \frac{1}{N_\theta}\sum_{\theta,x_\theta}\frac{f_\theta(x_\theta)}{p_\theta(x_\theta)}|x_\theta\rangle\langle x_\theta|. \tag{6.13}$$

Here f_θ is our measured marginal function, $f_\theta(x_\theta)$ the relative frequency with which x_θ was measured, and $p_\theta(x_\theta) = \mathrm{Tr}(|x_\theta\rangle\langle x_\theta|\hat{\rho}_k)$ is the probability of our

current guess $\hat{\rho}_k$ to measure x_θ. In the Fock state basis, we can write

$$\begin{aligned} |x_\theta\rangle\langle x_\theta| &= \sum_{n,n'} \langle n|x_\theta\rangle\langle x_\theta|n'\rangle |n\rangle\langle n'|, \\ \langle x_\theta|n\rangle &= \frac{2^{-n/2}}{\sqrt{n!}\pi^{\frac{1}{4}}} e^{-x_\theta^2/2} e^{-in\theta} H_n(x_\theta), \end{aligned} \tag{6.14}$$

where $H_n(x)$ is the n-th Hermite polynomial. The iteration converges towards the ideal density operator $\hat{\rho}$, because as we approach the ideal state, $\mathrm{Tr}(|x_\theta\rangle\langle x_\theta|\hat{\rho}) = f_\theta(x_\theta)$, and then because of the closure relation, $\hat{R} = \sum_{x_\theta} |x_\theta\rangle\langle x_\theta| = \mathbb{1}_5$.

6.5 Input-Output Theory for Quantum Pulses

An alternative and more abstract method to reconstruct the quantum state is the following Gedankenexperiment [80], where virtual cavities with time-dependent mirror reflectivities inject input pulses into and absorb output pulses from a target system.

For our purposes, we can ignore the input part of the idea and consider the outgoing pulse $f(t)$ from Eq. (6.4) now to be incident on a virtual one-sided cavity with cavity mode annihilation operator $\hat{b}$. If the mirror coupling of the second cavity is chosen to be

$$g_f(t) = -\frac{f^*(t)}{\sqrt{\int_0^t dt' |f(t')|^2}} \tag{6.15}$$

the state of the pulse is asymptotically mapped onto the virtual cavity mode. The system is treated as a cascaded system [81, 82] with the additional intercavity coupling Hamiltonian

$$\hat{H} = i\sqrt{\frac{\kappa}{2}}(g_f(t)\hat{a}^\dagger\hat{b} - g_f^*(t)\hat{a}\hat{b}^\dagger) \tag{6.16}$$

and updated cavity decay

$$\begin{aligned}\kappa\mathcal{D}[\hat{a}]\hat{\rho} &\rightarrow \mathcal{D}[\sqrt{\kappa}\hat{a}+\frac{g_f(t)}{\sqrt{2}}\hat{b}]\hat{\rho} \\ &= \kappa\mathcal{D}[\hat{a}]\hat{\rho}+\sqrt{\frac{\kappa}{2}}(g_f(t)\mathcal{D}[\hat{a},\hat{b}]+g_f^*(t)\mathcal{D}[\hat{b},\hat{a}])\hat{\rho}+\frac{|g_f(t)|^2}{2}\mathcal{D}[\hat{b}]\hat{\rho},\end{aligned} \tag{6.17}$$

where the generalised Lindblad form is

$$\mathcal{D}[\hat{a},\hat{b}]\hat{\rho} = 2\hat{a}\hat{\rho}\hat{b}^\dagger-\hat{\rho}\hat{b}^\dagger\hat{a}-\hat{b}^\dagger\hat{a}\hat{\rho}. \tag{6.18}$$

The quantum state can then simply read out from the state of the virtual cavity mode.

Part III

Single- or Few-atom Sources of Nonclassical Light

Chapter 7

Deterministic Single-atom Source of Quasi-superradiant N-photon Pulses

7.1 Introduction

Recent proposals and proof-of-principle demonstrations of optical N-photon sources, typically using parametric down conversion or quantum dots, are intrinsically probabilistic and low-yield in nature [83–89]. The use of a known number of (effective) two-level atoms emitting into a cavity or photonic waveguide has also been proposed [90–93], but the required many-body control and repeatability is still very challenging. Complementary to this, there also exists a range of ideas and efforts around N-photon sources in the microwave regime [94–98].

Here, we propose a deterministic N-photon source that requires just a *single* atom and makes use of its entire, multilevel energy structure in a manner that reduces the effective system dynamics to a simple and transparent form. In particular, we demonstrate that a single alkali atom coupled strongly to a cavity mode and subject to Raman transitions between sublevels of a ground F hyperfine state can replicate the collective emission of $N = 2F$ initially excited, two-level atoms into the cavity mode. In this way, a "superradiant" pulse of

precisely N photons can be extracted, through the cavity mode, from a *single* atom. Moreover, an initial, coherent superposition state of the atom's ground sublevels is also preserved in the emission process, enabling the generation of a light pulse in an arbitrary superposition of Fock states; as particular examples, we consider $0N$-state and binomial-code-state pulses of light.

Key to the reduction of the single-atom, multilevel dynamics is a very large detuning of the laser and cavity fields from an entire excited state hyperfine manifold of the atom, such that the excited-state hyperfine splittings can be ignored; alternatively, such that the total electronic angular momentum, J, is a good quantum number. Such large detuning from the atomic transition in turn demands a very large atom-cavity coupling strength and, as we show here, the experimental configurations of [3–8] attain the requisite strength for our scheme to be feasible and efficient.

The potential for making use of the multilevel energy structure of an alkali atom to prepare N-photon states has been considered previously, using either adiabatic passage with time-dependent laser and atom-cavity coupling strengths [99, 100], or cavity-mediated optical pumping between atomic ground state sublevels [101, 102]. However, in contrast to the present scheme, these approaches assume near-resonant laser and cavity fields and consider just a single $F \leftrightarrow F'$ transition. This limits the range of validity of the approaches and means that Clebsch-Gordan coefficients between m_F and $m_{F'}$ sublevels play a nontrivial and restricting (with regard to choice of F and F') role in the scope and performance of the scheme.

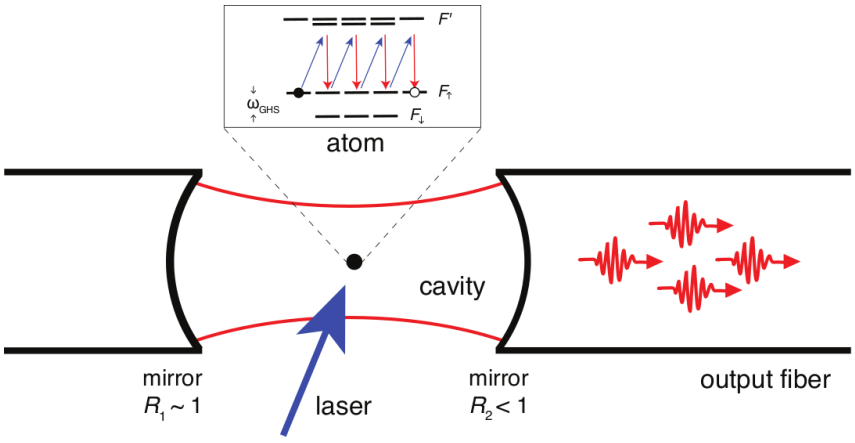

Figure 7.1: Fibre-cavity configuration with a σ_+-polarised laser and π-polarised cavity mode coupled to the D_1 line of a ^{87}Rb atom. The atom is initially prepared in the $\{F = 2, m_F = -2\}$ ground-state sublevel. The cavity field decays predominantly through the right-hand mirror.

7.2 Engineered Tavis-Cummings type Dynamics

We consider a single alkali atom tightly confined inside an optical cavity. The atom couples to a π-polarised cavity mode (annihilation operator $\hat{a}$) and is also driven by either a σ_+- or σ_--polarised laser field (Fig. 7.1). We define the atomic dipole transition operators

$$\hat{D}_q(F, F') = \sum_{m_F=-F}^{F} |F, m_F\rangle\langle F, m_F|\mu_q|F', m_F+q\rangle\langle F', m_F+q|, \tag{7.1}$$

where $q = \{-1, 0, 1\}$ and μ_q is the dipole operator for $\{\sigma_-, \pi, \sigma_+\}$-polarisation, normalised such that $\langle\mu\rangle = 1$ for a cycling transition. The master equation for the density operator, $\hat{\rho}$, of our system in the interaction picture is ($\hbar = 1$)

$$\dot{\hat{\rho}} = -i\left[\hat{H}_\pm, \hat{\rho}\right] + \kappa\mathcal{D}[\hat{a}]\hat{\rho} + \frac{\gamma}{2}\sum_q \mathcal{D}\left[\sum_{F,F'} \hat{D}_q(F, F')\right]\hat{\rho}, \tag{7.2}$$

where κ is the cavity field decay rate, γ the free-space atomic spontaneous emission rate, and $\mathcal{D}[\hat{O}]\hat{\rho} = 2\hat{O}\hat{\rho}\hat{O}^\dagger - \hat{\rho}\hat{O}^\dagger\hat{O} - \hat{O}^\dagger\hat{O}\hat{\rho}$. Setting the zero of energy at the lower ground hyperfine level, and assuming (for the moment) zero magnetic field, the Hamiltonian is

$$\begin{aligned}\hat{H}_\pm = {} & \Delta_c\hat{a}^\dagger\hat{a} + \sum_{m_{F_\uparrow}} \omega_{\mathrm{HF}} |F_\uparrow, m_{F_\uparrow}\rangle\langle F_\uparrow, m_{F_\uparrow}| \\ & - \sum_{F',m_{F'}} \Delta_{F'} |F', m_{F'}\rangle\langle F', m_{F'}| \\ & + \sum_{F,F'} \left(\frac{\Omega}{2} \hat{D}_{\pm 1}(F,F') + g\hat{a}^\dagger \hat{D}_0(F,F') + \mathrm{H.c.} \right).\end{aligned} \tag{7.3}$$

Here, $\Delta_c = \omega_c - \omega_\pm$ is the detuning between the cavity and laser frequencies, $\Omega = |\Omega|e^{i\phi}$ the Rabi frequency of the $\sigma_\pm$-polarised laser field, g the atom-cavity coupling strength, ω_{GHS} the ground state hyperfine splitting [$F_\uparrow$ ($F_\downarrow$) denotes the upper (lower) hyperfine ground state], and $\Delta_{F'} = \omega_\pm - \omega_{F'}$ the detuning of the laser from the $F_\downarrow \leftrightarrow F'$ transition. Note that, given the large coupling strengths and detunings that we consider here, we assume that the light fields couple all hyperfine ground and excited states. Consistent with this, we also assume that all atomic decays of a given polarisation are into a common reservoir [103].

If we now assume also, more specifically, that the detunings of the fields (cavity and laser) are much larger than the excited state hyperfine splitting, such that this splitting can essentially be neglected, then, in addition to being able to adiabatically eliminate the atomic excited states and neglect atomic spontaneous emission, we obtain a tremendously simplified effective model of the atom-cavity dynamics in the form of an anti-Tavis-Cummings or Tavis-Cummings model (anti-TCM or TCM, depending on the polarisation of the laser field) for a collective spin F [71, 104, 105], where F (either $F_\uparrow$ or $F_\downarrow$) is determined by the initial state of the atom; i.e., our master equation reduces

to

$$\dot{\hat{\rho}} = -i\Big[\hat{\mathcal{H}}_{\pm}, \hat{\rho}\Big] + \kappa\mathcal{D}[\hat{a}]\hat{\rho}, \tag{7.4}$$

with

$$\hat{\mathcal{H}}_{\pm} = \omega\hat{a}^{\dagger}\hat{a} + \omega_0\hat{S}_z + \lambda\Big(e^{-i\phi}\hat{a}\hat{S}_{\mp} + e^{i\phi}\hat{a}^{\dagger}\hat{S}_{\pm}\Big), \tag{7.5}$$

where $\{\hat{S}_{\pm}, \hat{S}_z\}$ are the spin-F angular momentum operators and, for example, for the D_1 line of ^{87}Rb, the effective parameters are

$$\begin{aligned} \omega &= \Delta_c + \frac{g^2}{3\Delta}, \\ \omega_0 &= \omega_z \mp \frac{|\Omega|^2}{24\Delta}, \\ \lambda &= \frac{g|\Omega|}{12\sqrt{2}\Delta}. \end{aligned} \tag{7.6}$$

Here, we now assume an external magnetic field giving rise to a shift ω_z of the m_F levels. The detuning Δ depends on the choice of F; for $F = F_{\uparrow}$, we take $\Delta = \Delta_{F'} + \omega_{\mathrm{HF}}$, where the choice of F' in $\Delta_{F'}$ makes little difference due to the very large detuning assumed (in practice, we pick the lowest F'). The same forms of expressions for $\{\omega, \omega_0, \lambda\}$ are obtained for the D_1 and D_2 lines of other alkali atoms, but with slightly different numerical factors. Note that such a reduction of dynamics as described above has been demonstrated experimentally in a many-atom realisation of the Dicke model with spin-1 atoms in an optical cavity [104].

The essence of our scheme follows clearly and simply from the dynamics described by (7.4) and (7.5). With the choice $\hat{\mathcal{H}}_{\pm}$ and corresponding initial atom-cavity state $|F, m_F = \mp F\rangle|0\rangle_{\mathrm{cav}}$, the system evolves irreversibly to the unique steady state $|F, m_F = \pm F\rangle|0\rangle_{\mathrm{cav}}$ with emission from the cavity of a pulse of exactly $2F$ photons. The dynamics is irreversible because each photon

that is created (via $\hat{a}^\dagger \hat{S}_+$) in and subsequently emitted from the cavity (at rate κ) occurs in unison with a single unidirectional step along the ladder of spin states.

Additionally, in the regime of interest to us, where $\kappa \gg \sqrt{F}\lambda$ and $\omega \simeq \omega_0 \simeq 0$ (via tuning of Δ_c and ω_z), the effective model of our *single* spin-F atom emulates resonant, cavity-mediated superradiant emission of $2F$ spin-$\frac{1}{2}$ particles; i.e., the emitted $2F$-photon pulse will have a characteristic sech^2-shaped temporal profile [106].

7.3 Output Photon Number

A preliminary way to quantify the quality of our state generation scheme is to compute the time evolution of the output photon flux from the cavity and the mean number of emitted photons,

$$\overline{N} = 2\kappa \int_0^\infty dt \langle \hat{a}^\dagger(t)\hat{a}(t)\rangle. \tag{7.7}$$

We consider first the case of a ^{87}Rb atom initially prepared in the ground state $|F = 2, m_F = -2\rangle$ and coupled to the laser and cavity fields via the D_1 line. With this system, we expect an output pulse of exactly 4 photons. Note that we neglect any extraneous photon losses, which is a good approximation provided the dominant loss channel from the system is photon transmission through the cavity mirror (at rate κ). For our quantum trajectory simulations the photon detection efficiency is additionally assumed to be ideal.

We solve the master equation numerically for the full model, (7.2–7.3), and compare results with the solution for the effective anti-TCM, (7.4–7.5), for two sets of cavity QED parameters: (i) $\{\kappa, g, \gamma\}/2\pi = \{50, 250, 5.7\}$ MHz and (ii) $\{\kappa, g, \gamma\}/2\pi = \{0.5, 2, 0.0057\}$ GHz. The first set corresponds to the fibre microcavity system of [3–5], while the second set is relevant to the nanocavity system of [6–8]. Results for the output photon flux are shown in Fig. 7.2. The agreement between the full and reduced models is clearly very good, and the predicted sech^2-shaped pulse is confirmed, with a duration on the order

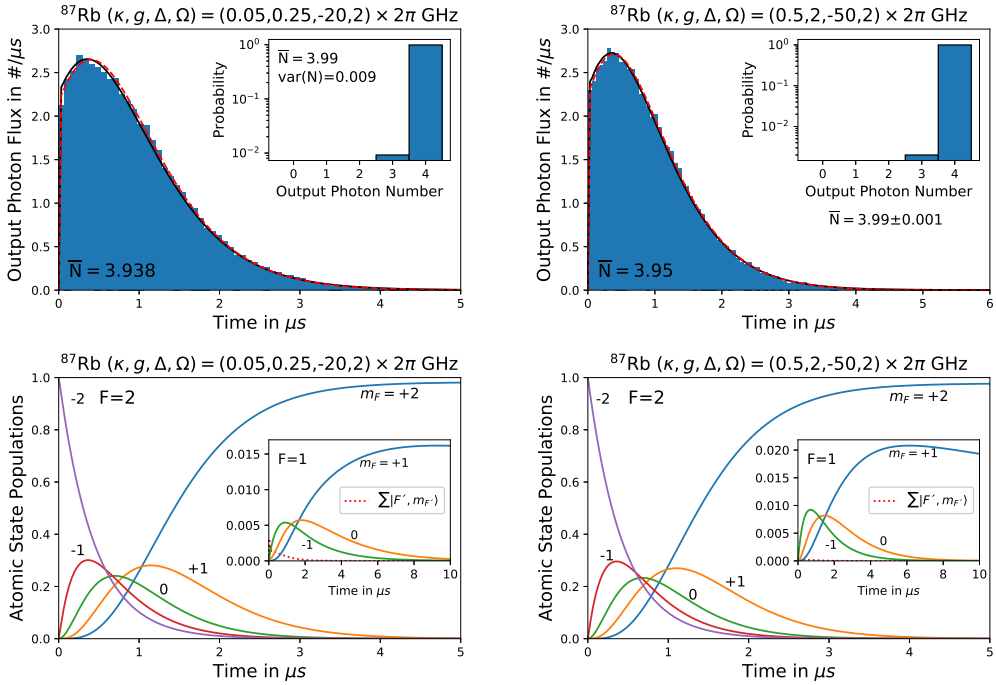

Figure 7.2: Top row: Output photon flux for a ^{87}Rb atom initially prepared in $|F = 2, m_F = -2\rangle$. The black solid line represents the full model and the red dashed line the anti-TCM. The histogram shows the temporal distribution of photocounts (renormalised to $\bar{N}$) for 10000 trajectories of the anti-TCM with additional, effective spontaneous emission. The number below the curves gives $\bar{N}$ for the full model. Insets: Histogram of photon number counts per trajectory (i.e., per output pulse). Bottom row: Atomic ground state populations ($F = 2$: main plot, $F = 1$: inset), and total excited state population (inset, red-dashed) as a function of time.

of $(F\lambda^2/\kappa)^{-1}$. The atomic state populations are also plotted in Fig. 7.2 and similarly show the expected evolution, with a smooth transfer of population along the $F = 2$ hyperfine level to the final state $|F = 2, m_F = +2\rangle$. A very small fraction of population may be transferred to the $F = 1$ ground state via off-resonant processes, but, in fact, the effective superradiant emission simply continues from within this level and any population there is ultimately driven back (also by an off-resonant process) into the $F = 2$ level and so to the final (dark) state $|F = 2, m_F = +2\rangle$. Atomic excited state populations are essentially negligible.

Similar results for the photon flux are shown in Fig. 7.3 for a ^{133}Cs atom

initially prepared in the $|F = 4, m_F = -4\rangle$ ground state, also operating on the D_1 line. For the parameters used, there is a slight discrepancy between pulse shapes for the two models, but the mean photon number obtained from the full model is still very close to the expected value of 8. The discrepancy arises primarily from the larger excited state hyperfine splitting in ^{133}Cs, which means that a larger detuning is required to ensure closer agreement with the TCM; a similar discrepancy is also observed in ^{87}Rb for smaller detunings.

The integrated photon flux obtained from the master equation, however, does not tell us about the variance in the photon number of the output pulse. To get the variance we perform quantum trajectory simulations [43, 44] and record the times and total number of photon counts in each trajectory. The histogram of photon detection times gives us again the output photon flux, which is shown for comparison in Figs. 7.2 and 7.3, along with the photon number distribution and its variance for the output pulse. The distributions are clearly very close to an ideal number state. Note that for these simulations we do not use the full model (owing to the stiffness of the numerical integration caused by the large detunings and ground state hyperfine splitting), but rather use the anti-TCM (or TCM) with spontaneous emission added, in the form of an effective Lindblad operator acting just within the relevant ground state. Spontaneous emission to the other hyperfine ground state is therefore

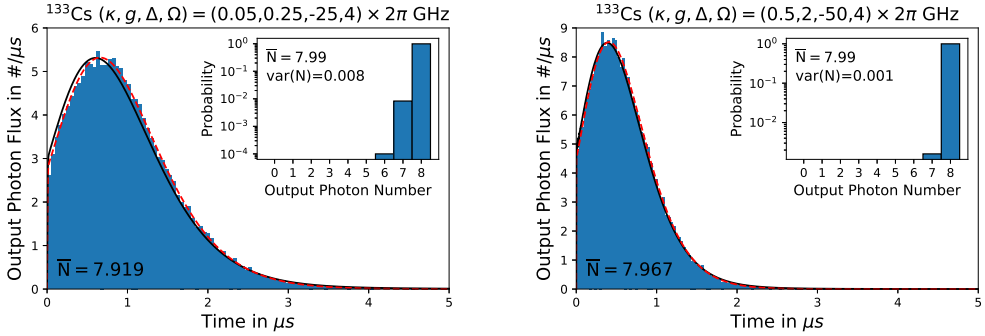

Figure 7.3: Output photon flux for a ^{133}Cs atom initially prepared in $|F = 4, m_F = -4\rangle$. Line markings, histograms, and annotations are the same as described in Fig. 2.

neglected, but the numerical results from the master equation support this as a good approximation.

Finally, we note that shorter or longer output pulses can be obtained by changing the detuning Δ and/or laser Rabi frequency Ω. Also, in the results presented here, we assume an instantaneous switch-on of the laser field. This can be relaxed to allow for a smooth initial ramp of the laser field to its peak value, which can be used to tailor the shape of the output $2F$-photon pulse.

7.3.1 Quantum Trajectories

To access the variance in the output photon number we perform photon-counting quantum jump simulations [43, 44], where we accumulate photocount records from an ensemble of quantum trajectories. In each quantum trajectory, the system state is evolved with the non-Hermitian effective Hamiltonian

$$\hat{H}_{\rm eff} = \hat{\mathcal{H}}_{\pm} - i\kappa\hat{a}^{\dagger}\hat{a} - i\frac{\gamma}{2}\sum_{q}\hat{\mathcal{L}}_{q}^{\dagger}\hat{\mathcal{L}}_{q}, \tag{7.8}$$

where $\hat{\mathcal{L}}_q$ ($q = -1, 0, +1$) is an effective spontaneous emission operator (see below). In particular, over an infinitesimal time step Δt, we have

$$|\psi(t+\Delta t)\rangle = e^{-i\hat{H}_{\rm eff}t}|\psi(t)\rangle \approx \Big(1 - i\hat{H}_{\rm eff}\Delta t + \mathcal{O}(\Delta t^2)\Big)|\psi(t)\rangle. \tag{7.9}$$

The loss in norm through this non-Hermitian evolution is given by

$$\Delta p = \Delta t\langle\psi(t)|\kappa\hat{a}^{\dagger}\hat{a}|\psi(t)\rangle + \Delta t\langle\psi(t)|\frac{\gamma}{2}\sum_{q}\hat{\mathcal{L}}_{q}^{\dagger}\hat{\mathcal{L}}_{q}|\psi(t)\rangle, \tag{7.10}$$

which corresponds to the probability for a quantum jump to occur. If a jump does occur (as decided by a random number), we replace the effective Hamiltonian evolution with the action of a quantum jump, itself also chosen by a

random number:

$$|\psi(t+\Delta t)\rangle \rightarrow \begin{cases} \frac{\sqrt{2\kappa}\hat{a}|\psi(t)\rangle}{\sqrt{\langle\psi(t)|2\kappa\hat{a}^\dagger\hat{a}|\psi(t)\rangle}} & \text{or} \\ \frac{\sqrt{\gamma}\hat{\mathcal{L}}_q|\psi(t)\rangle}{\sqrt{\langle\psi(t)|\gamma\hat{\mathcal{L}}_q^\dagger\hat{\mathcal{L}}_q|\psi(t)\rangle}} & (q=-1,0 \text{ or } +1). \end{cases} \tag{7.11}$$

If the jump corresponds to emission of a photon from the cavity, we record its timestamp and increase the photon count for that trajectory by one; sampling over many trajectories then yields the temporal distribution of the output photons and the output photon number histogram, respectively.

7.4 Atomic State Populations

Let us start with discussing the atomic state populations in more detail. In Fig. 7.4 below we show the time evolution of the atomic state populations for parameter sets that are the same as those used in Fig. 7.2, except for larger detunings. This change yields pulses and dynamics of longer duration, however, apart from this, the behaviour is qualitatively the same. For convenience, in the first column we plot the output photon flux again. The atomic population is seen to transfer smoothly and predominantly along the $F = 2$ ground state manifold from the initial state $|F = 2, m_F = -2\rangle$ to the state $|F = 2, m_F = +2\rangle$. The peak in the output photon flux coincides approximately with the peak in the population of the state $|F = 2, m_F = -1\rangle$. A small amount of population makes it into the $F = 1$ manifold, where it is also subject to effective, resonant (spin-1) anti-Tavis-Cummings dynamics and is transferred to the state $|F = 1, m_F = +1\rangle$. From there, a far-off-resonant Raman transition eventually transfers this small population into the target state $|F = 2, m_F = +2\rangle$.

For the two cases considered in Fig. 7.4 there is not a large difference in the populations of the $F = 2$ manifold. The $F = 1$ manifold on the other hand shows some slight differences; it depletes more rapidly (even though initially more highly populated) for the nanocavity system as a result of the

larger atom-cavity coupling strength, which enhances the off-resonant Raman transition back into the $F = 2$ ground state. The figure also underpins our assumptions that the excited state and lower-ground-state populations are very small, thus ensuring the validity of the effective Tavis-Cummings (or anti-Tavis-Cummings) model.

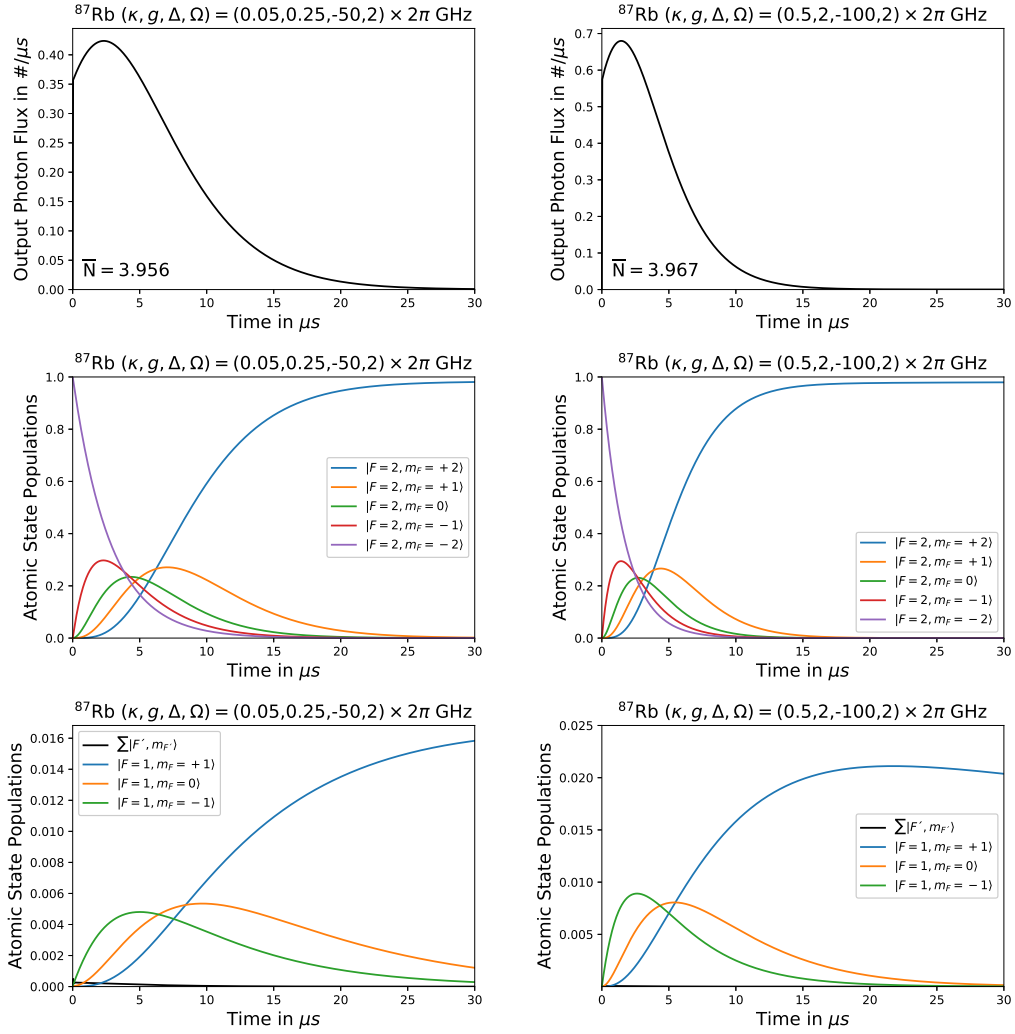

Figure 7.4: Output photon flux (top row), atomic ground state populations ($F = 2$: middle row, $F = 1$: bottom row), and total excited state population (bottom row) as a function of time for a ^{87}Rb atom initially prepared in state $|F = 2, m_F = -2\rangle$. Parameters are for optical microcavity (left column) and nanocavity (right column) systems.

7.5 Additional Examples

7.5.1 Constant Laser Amplitude

As the formula for the approximate time scale of the output pulse $\tau \propto \frac{\kappa\Delta^2}{Fg^2|\Omega|^2}$ suggests we can create even shorter pulses by further decreasing the detuning Δ. While the approximation, that the detuning is larger than the excited state hyper fine splitting, might still be valid, at some point we usually observe a discrepancy between the full system dynamics from the Tavis-Cummings ones in the form of oscillations in the initial rise of the output photon flux and an offset in the two curves.

We observe these oscillations only as Δ becomes small but the $\{\kappa, g\} = \{0.05, 0.25\}\cdot 2\pi$ GHz set of values is more robust against them than the $\{\kappa, g\} = \{0.5, 2\}\cdot 2\pi$ GHz set. That is because their occurrence is facilitated by a larger cavity decay rate κ, but we can counteract to a certain degree and eliminate them by increasing $|\Omega|$ and/or g but lowering κ is the most effective.

While the offset seems to worsen by lowering Δ (see top row of Fig. 7.2), the change is very small. It is far more affected by the amplitude of κ and will persist through to much larger Δ as shown in the middle row of Fig. 7.5 where the cavity decay rate κ that is a factor 2 larger than before (and closer to state-of-the-art values [6]), where the two curves are noticeably offset from each other and oscillations arise for the lower detuning.

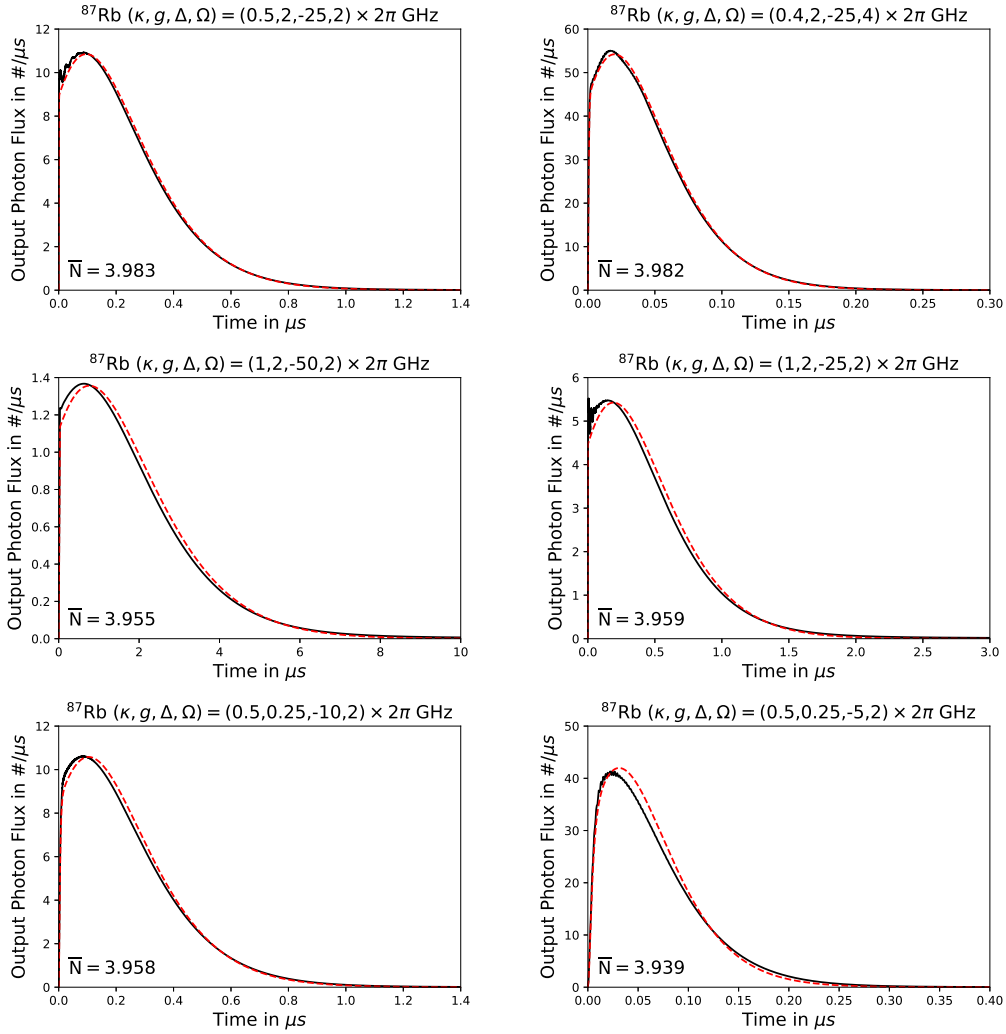

Figure 7.5: Output photon flux for a ^{87}Rb atom initially prepared in $|F = 2, m_F = -2\rangle$. The lines represent the full model (solid black) and the simple Tavis-Cummings model where the excited states have been adiabatically eliminated (dashed red). The number below the curves represents the output photon number from the full model.

7.5.2 Time-varying Laser Amplitude

In a real experiment, the laser will not instantaneously turn on at the chosen intensity, but rather get there through a continuous ramp. Ramping would eliminate some of the very fast non-adiabatic processes which affect the early parts of the pulse. Additionally, we would like to know how valid the "instantaneous" approximation really is. We approximate the ramp through the

following sinusoidal function

$$r(t) = \begin{cases} \sin(\frac{\pi t}{2t_r}), & t < t_r \\ 1, & t > t_r \end{cases}. \tag{7.12}$$

The smoothness of the initial rise increases slowly for increasing ramp times. The output photon number and the offset present for larger κ stays mainly the same. For very slow ramps, i.e., large t_r, we are able to produce pulses with both smooth leading and trailing edges.

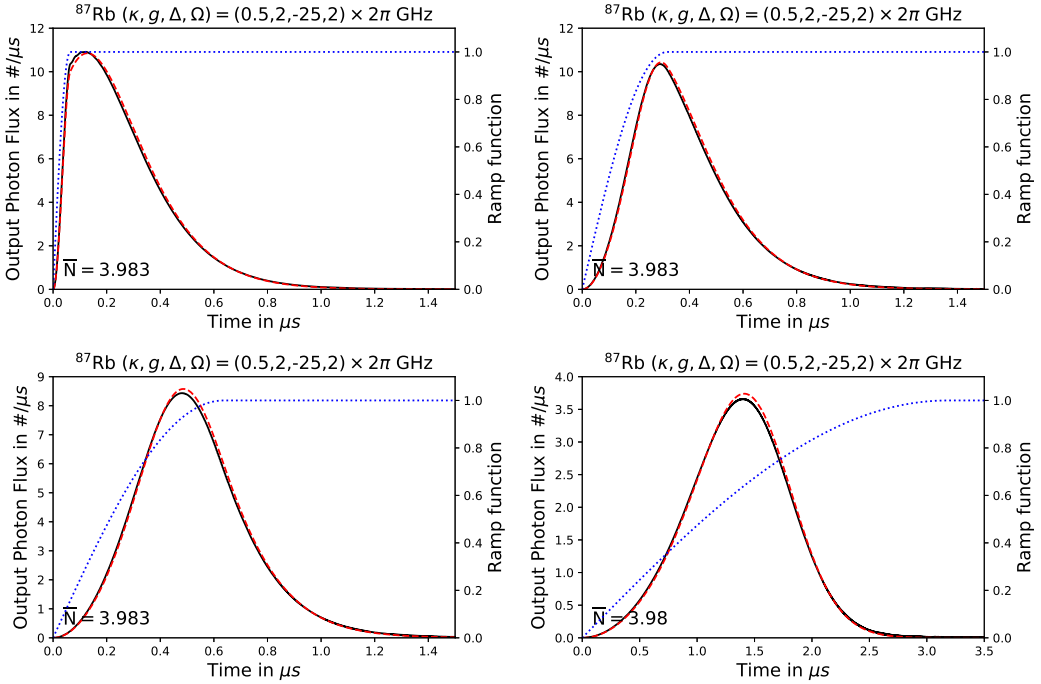

Figure 7.6: Output photon flux for a ^{87}Rb atom initially prepared in $|F = 2, m_F = -2\rangle$. The lines represent the full model (solid black), the simple Tavis-Cummings model where the excited states have been adiabatically eliminated (dashed red) and the ramp function $r(t)$ (dotted blue) that has been applied to both models. The number below the curves represents the output photon number from the full model.

7.6 $0N$-states and other Superpositions

Instead of starting with an atom in an end state of the Zeeman ladder, we also have the option to start with a superposition of Zeeman substates; for example, $|\psi_{\rm oat}\rangle_F = (|F,-F\rangle+|F,+F\rangle)/\sqrt{2}$, which can be created using a one-axis twisting (oat) scheme [107], or an arbitrary superposition, created using a scheme such as in [108]. With our proposed system, these atomic superposition states are directly mapped onto photonic states of the output light pulse. So, for example, the initial state $|\psi_{\rm oat}\rangle_F$ leads to an output pulse in a coherent superposition of vacuum and $N = 2F$ photons, i.e., an $0N$-state, $|\Psi\rangle_{\rm pulse} = (|0\rangle_{\rm out}+|N\rangle_{\rm out})/\sqrt{2}$, which is a basic resource in schemes proposed for universal quantum computation [20]. The output photon flux and photon number distribution for initial atomic state $|\psi_{\rm oat}\rangle_{F=2}$ are shown in Fig. 7.7 for ^{87}Rb with cavity QED parameters relevant to the fibre microcavity.

As a further example, in Fig. 7.7 we also consider an initial state of ^{87}Rb of the form $|\psi_{\rm bc}\rangle_{F=2} = (|2,-2\rangle+\sqrt{2}|2,0\rangle+|2,+2\rangle)/2$, yielding an output pulse state $|\Psi\rangle_{\rm pulse} = (|0\rangle_{\rm out}+\sqrt{2}|2\rangle_{\rm out}+|4\rangle_{\rm out})/2$. Such a state is of particular interest, as it constitutes a superposition of states $|0_{\rm L}\rangle = (|0\rangle+|4\rangle)/\sqrt{2}$ and $|1_{\rm L}\rangle = |2\rangle$, which are logically encoded (binomial code) states of a qubit for a quantum computation scheme protected up to one photon loss [21]. Note that in mapping general atomic ground-state superpositions onto the states of the output light pulses, one must pay attention to the relative phases between the different components and the phase ϕ of the effective cavity-spin coupling. For an exact mapping of relative phases, we require in our model that $\phi = \mp\pi/2$ (depending on the sign of Δ), which can of course be chosen through the phase of the laser field. Alternatively, ϕ can also be incorporated as the relative phase between neighbouring m_F levels in the initial atomic state.

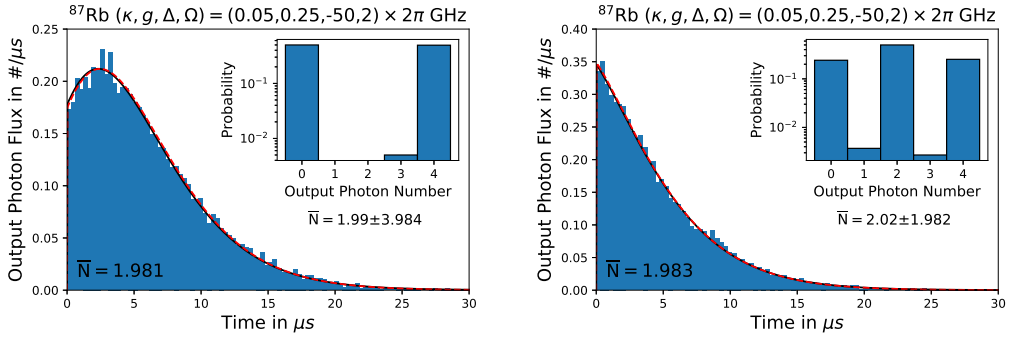

Figure 7.7: Output Photon Flux of a Rubidium atom prepared in equal superposition states of $m_F = -2$ and $m_F = 2$ (left), and of $m_F = -2$, $m_F = 0$ and $m_F = 2$ (right). The lines represent the full model (solid black) and the simple Tavis-Cummings model where the excited states have been adiabatically eliminated (dashed red). The histogram shows the temporal distribution of photocounts (renormalised to $\overline{\mathrm{N}}$) for 10000 trajectories of the Tavis-Cummings model with additional effective spontaneous emission. The number below the curves represents the output photon number from the full model. The inset plots show the histogram of the photon number counts for the different quantum trajectories and includes the mean photon number for the effective Tavis-Cummings model plus the variance of the photocounts as an error.

In Fig. 7.7 the pulses of the two superpositions state we consider are depicted. Note that the pulse shape of the 0N-state is the same as the one of the corresponding Fock state, just rescaled by a factor $\frac{1}{2}$. Contrariwise, the other superposition state gives rise to a very different looking pulse that resembles a superradiant pulse where everything before the maximum has been discarded.

7.6.1 Relative Phase Shifts in Superposition States

To understand the origin of the phase shift between the different components of a superposition state, let us, without loss of generality, look at the most simple imaginable example; the coherent time evolution of the initial state with the atom one step away from the edge in an empty cavity, i.e., $\frac{1}{\sqrt{2}}(|F = 2, m_F = +2\rangle + |F = 2, m_F = +1\rangle)|0\rangle_{\mathrm{cav}}|0\rangle_{\mathrm{out}}$.

If we consider the capture cavity method as described in Section 6.5, then for the Anti-Tavis-Cummings version of the Hamiltonian, the corresponding

time evolution operator including the cavity decay is given by [82]

$$\begin{aligned}\hat{U} = 1 - i\Delta t\lambda(e^{-i\phi}\hat{a}\hat{S}_- + e^{i\phi}\hat{a}^\dagger\hat{S}_+) \\ -\kappa\hat{a}^\dagger\hat{a}\Delta t - |g_f(t)|^2\hat{b}^\dagger\hat{b}\Delta t - \sqrt{2\kappa}g_f^*(t)\hat{a}b^\dagger\Delta t.\end{aligned} \tag{7.13}$$

The final state will be $|F = 2, m_F = +2\rangle|0\rangle_{\text{cav}}\frac{1}{\sqrt{2}}(|0\rangle_{\text{out}} + e^{i\varphi}|1\rangle_{\text{out}})$, where φ is a phase to be determined below. By virtue of being a dark state, the phase of the $|F = 2, m_F = +2\rangle)|0\rangle_{\text{cav}}|0\rangle_{\text{out}}$ component of the wave function remains unchanged. Recall that $g_f^*(t) \propto -f(t)$, where in this case f is a positive real-valued function, thus the transfer into the virtual cavity does not cause any phase change. The phase φ of the one-photon output state $|F = 2, m_F = +2\rangle|0\rangle_{\text{cav}}|1\rangle_{\text{out}}$ is therefore determined by the phase of $|F = 2, m_F = +2\rangle|1\rangle_{\text{cav}}|0\rangle_{\text{out}}$, which itself is regulated by the phase of the term proportional to $\hat{a}^\dagger\hat{S}_+$ of the Taylor expansion in Eq. (7.13). That phase amounts to

$$\varphi = \phi - \frac{\pi}{2} + \arg(\lambda), \tag{7.14}$$

meaning that we can use the polarisation (and to some extent the detuning) of the laser to control the relative phases in the state and set $\phi = \frac{\pi}{2} - \arg(\lambda)$ to get rid of all relative phases. If we were to consider a superposition of states that lie further apart, e.g., 2 steps, then the second power of $\hat{U}$ matters and Eq. (7.14) just doubles, meaning that Eq. (7.14) really is the shift incurred for each step along the Zeeman ladder.

7.7 Quantum State Tomography via Optical Homodyne Detection

The photon number distribution of the output pulse is not sufficient to confirm that the desired output state has been generated. To verify that the target quantum state has indeed been generated, we implement quantum state tomography on simulated, pulsed-homodyne measurements, obtained via the method

of homodyne quantum trajectories. That is, we reconstruct the Wigner function of the pulse by measuring marginals of the Wigner function for a set of homodyne phase angles θ and then applying the inverse Radon transform to these marginals [75]. For these simulations, we again use the TCM with effective spontaneous emission added. Results of these reconstructions are shown in Fig. 7.8. Our reconstructions can clearly be assigned to the predicted, ideal state. For a better comparison, we remove most of the noise from the simulated results by smoothing with a Gaussian blur, which reveals some discrepancy in the heights of the extrema between the ideal case and our reconstruction. This effect can also be observed in the untreated marginals, where we observe some noise in the outer peaks of these marginals that can be attributed to atomic spontaneous emission.

Alternatively, the density matrix itself can be reconstructed using maximum likelihood estimation [78, 79] on the marginals. We start with the identity matrix as the initial guess and go through 500 iterations. The resulting fidelities, a figure of merit telling us about the closeness to the target state $|\Psi\rangle$, of these output density matrices are computed via

$$\mathrm{F} = \left(\mathrm{Tr} \sqrt{\sqrt{|\Psi\rangle\langle\Psi|}\hat{\rho}\sqrt{|\Psi\rangle\langle\Psi|}} \right)^2 \tag{7.15}$$

and amount for the Fock state, 0N-state and the binomial-code state from Fig. 7.8 to 0.849, 0.922, and 0.937, respectively. These are in accord with the fidelities obtained using the capture-cavity method. This illustrates that, even though the superposition states are somewhat more complex, the initial atomic superposition states are, in a certain sense, closer to the final atomic state, and therefore more robust against spontaneous emission.

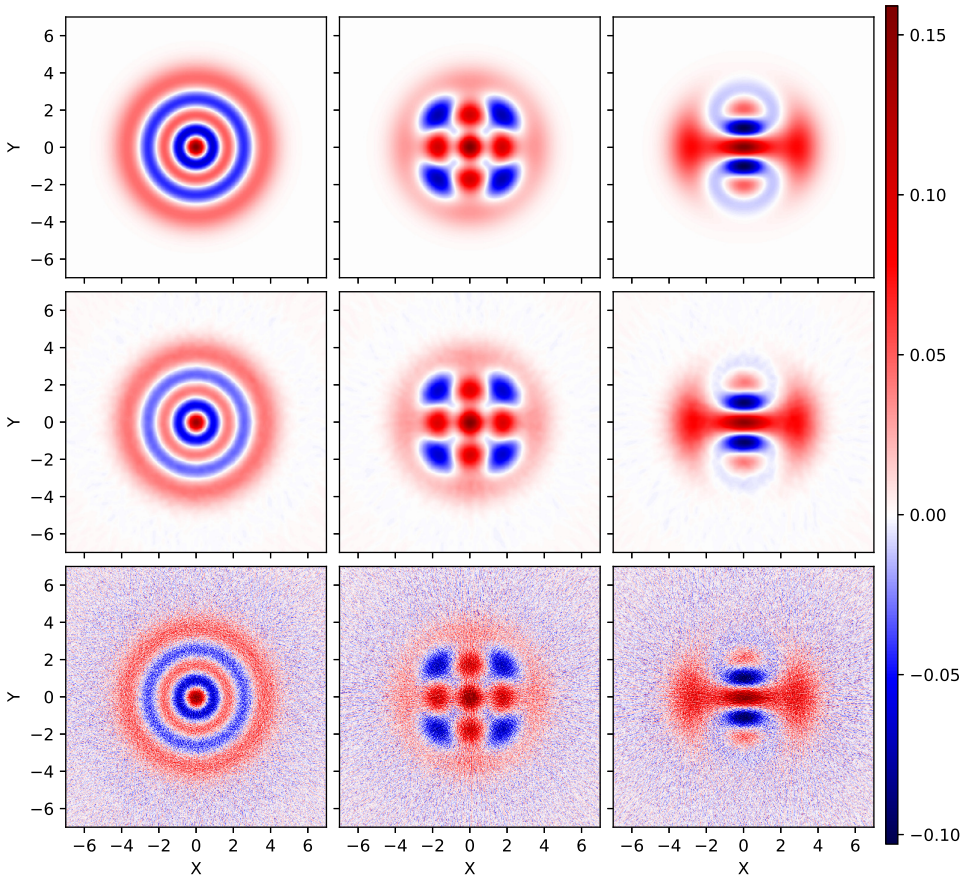

Figure 7.8: Ideal Wigner functions (top), smoothened with a Gaussian blur (middle) and raw (bottom) reconstructed Wigner functions for a single Rubidium atom in a fibre cavity setup ($\{\kappa, g, \Delta, \Omega\} = \{0.05, 0.25, -50, 2\}\cdot 2\pi$ GHz) for different configurations. The reconstructions are using a set of 500 angles $\theta \in [0, \pi)$ and 10000 trajectories per angle. The leftmost column shows $|4\rangle_{\text{out}}$, the middle $\frac{1}{\sqrt{2}}(|0\rangle_{\text{out}}+|4\rangle_{\text{out}})$ and the rightmost column $\frac{1}{2}(|0\rangle_{\text{out}}+\sqrt{2}|2\rangle_{\text{out}}+|4\rangle_{\text{out}})$.

7.7.1 Full Model Input-Output formalism

Input-output simulation for the full atomic model can be quite numerically demanding due to the additional "capture" cavity mode. We check that the desired state leaves the cavity also in the full model by looking at the simplest case, a 1-photon pulse from a ^{87}Rb atom initially prepared in $|F = 2, m_F = +1\rangle$. We manage to retrieve the 1-photon Fock state in the virtual cavity with

a fidelity of 0.994. As can be seen in Fig. 7.9, in that case, the filter function of the effective model corresponds to the absolute value of the full-model filter function. The non-zero free Hamiltonian of the full model (involving the large detuning Δ) adds a time-dependent phase.

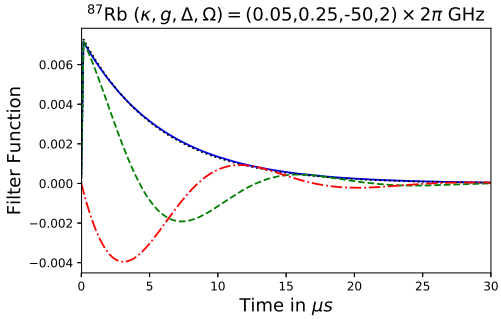

Figure 7.9: Plot comparing the filter functions for the full and the effective model for a ^{87}Rb atom initially prepared in the ground state $|F = 2, m_F = +1\rangle$. The lines represent $|f(t)|$ (solid blue), Re($f(t)$) (green dashed), and Im($f(t)$) (red dash-dotted) from the full model, and $f(t)$ (black dotted) from the simple Tavis-Cummings model where the excited states have been adiabatically eliminated.

7.8 Conclusions and Outlook

We have proposed a single-atom, deterministic source of optical number-state, $0N$-state, and binomial-code-state pulses. The scheme does not require time-dependent atom-laser or atom-cavity coupling strengths or detunings, or specific $F \leftrightarrow F'$ atomic transitions, and should be feasible with recently-demonstrated, fibre-integrated micro- and nano-cavity QED setups. Some other potential features of the scheme are worth noting. For the case of number-state pulses, it is a simple matter to generate a stream of separate pulses by switching the polarisation of the laser field at the end of each pulse and cycling the atom back and forth between the end states $|F, \pm m_F\rangle$. Also, one may increase the number of photons per pulse, N, by adding more atoms; e.g., with two identically-prepared ^{87}Rb atoms coupled collectively to the cavity mode, the effective spin in the TCM is simply doubled, enabling the generation of 8-photon pulses. Finally, we have assumed throughout this work that the cavity is essentially one-sided, so that pulses are emitted in just one direction into

the output fibre. We could equally well assume a symmetric cavity, in which case our scheme could be equated to a 50/50 beamsplitter with the incident state in one input port determined by the initial state of the atom. This would provide a straightforward means of producing an entangled state of light fields propagating in opposite directions away from the cavity.

Chapter 8

N-Photon Pulses via Resonant Optical Pumping of a Single Atom

8.1 Introduction

In the previous chapter, we proposed a single-atom source of N-photon pulses by exploiting the Zeeman substructure. There we focused on high couplings and far detuned fields, resulting in a coherent sequence of Raman transitions. We extend this now to the case of resonance, where the model no longer can be reduced to a simple Tavis-Cummings type model. Our scheme can essentially be described as resonant optical pumping [109], but where the cavity mode "catches" each emitted photon from the atom. This can be done efficiently when the cooperativity is high, so that emission through the cavity mode dominates spontaneous emission. Being on resonance opens up the door to high-cooperativity Fabry-Pérot cavities and tapered nanofibre cavities, which were impractical for our previous scheme due to their relatively low coupling strength. On the flipside, very high coupling strengths (in the GHz's) can also not be used for this setup, since such strengths are of the same order of magnitude as the hyperfine splittings and this would lead to significant coupling to the second ground hyperfine state.

So, to reiterate, we consider continuous resonant driving (as opposed to pulsed or continuous, detuned driving), but still include all hyperfine levels in

our model. As before, we also consider initial, coherent superpositions of the atom's ground states to investigate the possibility of generating more exotic Fock state superpositions in the outgoing light pulse, e.g., $0N$-states. However, there are also new aspects to be explored, for instance, the weaker atom-field coupling allows us to effectively hide the part of the atomic population that is in one hyperfine ground state, which in turn offers the chance to generate interesting entangled states.

8.2 Preliminary Considerations

When choosing a specific transition for the scheme, there are some things that prove to be beneficial for our purposes.

In particular, the total angular momentum of the excited state, F', should be smaller than or equal to that of the ground state F, else the opposite edge of the ground state Zeeman ladder is no longer a dark state and will undergo a cycling transition with the excited states, this ultimately complicates the quantum state tomography; more on that in Section 8.3.5. On top of that, the higher ground state can also generate larger photon numbers due to the larger number of Zeeman states.

This leaves us mainly with 2 possible transitions that we can consider for resonant driving: $F = 2 \leftrightarrow F' = 2$ and $F = 2 \leftrightarrow F' = 1$ of the Rubidium D_1 line. A visualisation of the corresponding main pathways through the state manifold is given in Fig. 8.1.

The same transitions can of course also be chosen in the D_2 line, but there the energy differences between the excited hyperfine states are smaller, making populating the non-resonantly driven excited states more likely. The D_2 line also always comes with an excited state F' that is larger than the highest ground state F, which is problematic because of the aforementioned cycling transition. Additionally, the spontaneous emission on that line is stronger. Therefore, we mainly consider the D_1 line.

If $F' = F$ for the considered transition, the $|F, m_F = 0\rangle \leftrightarrow |F', m_F = 0\rangle$ transition is forbidden and represents a "roadblock". In this case, we have to start in the $|F, m_F = 0\rangle$ state and we can only extract F photons.

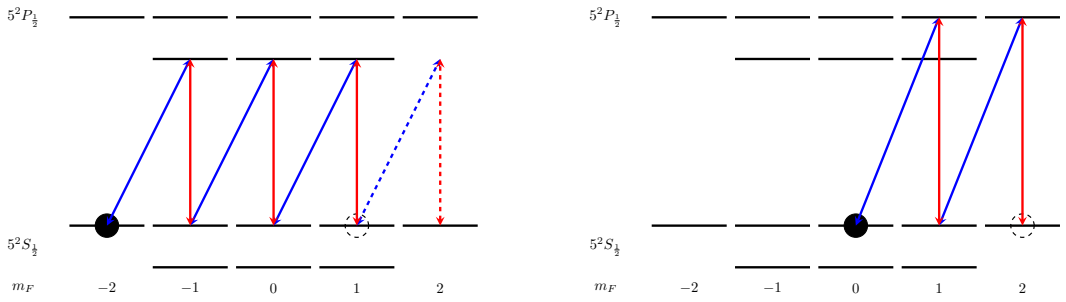

Figure 8.1: Depiction of the movement of the atoms through the state manifold for the D_1 line. The black dot is the initial state that yields the pulse with the highest photon number. The dashed circle represents the final state. (a) $F = 2 \leftrightarrow F' = 1$ transition with initial state $|F, m_F = -2\rangle$. The dashed lines represent the Raman process. (b) $F = 2 \leftrightarrow F' = 2$ transition with initial state $|F, m_F = 0\rangle$.

8.3 Number State Generation

We consider exactly the same full model as in the aforegoing chapter, except that now the detuning from the chosen $F \leftrightarrow F'$ transition is set to zero. The effective TCM model is no longer valid.

We solve the master equation numerically for the full model, (7.2–7.3), for two sets of cavity QED parameters: (i) a "high coupling regime" $\{\kappa, g, \gamma\}/2\pi = \{50, 250, 5.7\}$ MHz and (ii) a "low coupling regime" $\{\kappa, g, \gamma\}/2\pi = \{4, 25, 5.7\}$ MHz. The first set corresponds to the fibre microcavity system of [3–5], while the second set is relevant to state-of-the-art, high cooperativity Fabry-Pérot cavities or tapered nano-fibre cavities [110, 111].

8.3.1 Treating the $F = 1$ manifold as a single dark state

Note that for quantum trajectories in the present scenario we do not use the full model (owing to the stiffness of the numerical integration caused by the large ground state hyperfine splitting), but rather use a model where the other ground state is treated as a dark state. Additionally, trajectory simulations in the low coupling regime also ignore the off-resonant excited state manifold.

The large hyperfine splitting between the two ground states suggests that the lower one should not matter, and indeed the coherent dynamics show no

discernible difference between the inclusion or omission of the $F = 1$ manifold. However, due to the resonant drive, spontaneous emission to the $F = 1$ ground state cannot be neglected.

Hence, we eliminate all occurrences of $F = 1$ in the Hamiltonian $\hat{H}_{\pm}$, but keep the non-Hermitian quantum jump picture Hamiltonian otherwise unchanged,

$$\hat{H}_{NH} = \hat{H}_{\pm} - i\frac{\gamma}{2}\left(\sum_{F,F'}\hat{D}_q(F,F')\right)^{\dagger}\sum_{F,F'}\hat{D}_q(F,F'), \tag{8.1}$$

thus preserving the loss in amplitude corresponding to the different decay channels, even those to $F = 1$. Whenever a jump is deemed to have occurred we apply the new effective Lindblad operator $\sum_{F,F'}\hat{D}'_q(F,F')$, where we have replaced all the states of the $F = 1$ manifold by a single level $|D\rangle$, i.e.,

$$\hat{D}'_q(F=1,F') = \sum_{m_F=-F}^{F}|D\rangle\langle F,m_F|\mu_q|F',m_F+q\rangle\langle F',m_F+q|. \tag{8.2}$$

Thus we do not allow for any reexcitation from the $F = 1$ manifold and any population therein is completely lost to the dynamics. This means that the quantum trajectories tend to underestimate the output photon number in that regard, which explains the small discrepancy in the average output photon number between them and the master equation for most of the plots. Eliminating these manifolds can also lead to some overestimation, for instance, when additionally excited state levels are eliminated in the low coupling regime one is removing a competing slower process. The elimination of the other ground state eliminates also some destructive interference from different pathways with opposite sign Clebsch-Gordan coefficients.

8.3.2 Low Coupling Regime

We consider first the case of a ^{87}Rb atom initially prepared in the ground state $|F = 2, m_F = -2\rangle$ and coupled to the laser and cavity fields via the $F = 2 \leftrightarrow F' = 1$ transition (Fig. 8.1a). With this system, we expect an output pulse of exactly 3 photons. Then, we start with the ground state $|F = 2, m_F = 0\rangle$ and couple the laser and cavity fields via the $F = 2 \leftrightarrow F' = 2$ transition, which generates a 2 photon pulse (Fig. 8.1b).

Let us look at the output photon flux and quantum state reconstruction in Fig. 8.2 to begin with. The average photon number from the integrated output photon flux obtained from the master equation and from the quantum trajectories reaches values close to the target photon number, especially for the $F = 2 \leftrightarrow F' = 1$ transition. The photon counting statistics reveal that observing zero photons is more likely than observing one in both cases, which can be mostly attributed to spontaneous emission to $F = 1$. Decay to $F = 1$ affects the $F = 2 \leftrightarrow F' = 2$ disproportionately more than the $F = 2 \leftrightarrow F' = 1$ scheme because the average Clebsch-Gordan coefficients for $F = 1 \leftrightarrow F' = 2$ tend to be higher than those of $F = 1 \leftrightarrow F' = 1$.

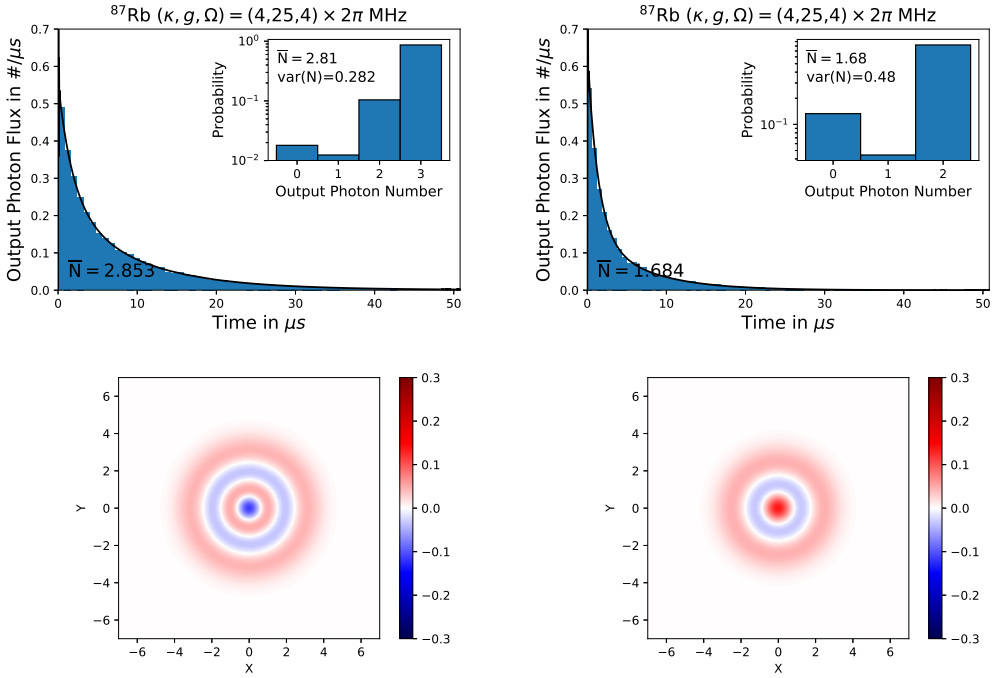

Figure 8.2: Output Photon Flux (top row) of a Rubidium atom prepared in $m_F = -2$ driven via $F = 2 \leftrightarrow F' = 1$ (left), and $m_F = 0$ driven via $F = 2 \leftrightarrow F' = 2$ (right). The lines represent the full master equation model (solid black). The histogram shows the temporal distribution of photocounts (renormalised to $\overline{\mathrm{N}}$) for 10000 trajectories of the reduced model. The number below the curves represents the output photon number from the full model. The inset plots show the histogram of the photon number counts for the different quantum trajectories and includes the mean photon number plus the variance of the photocounts. Corresponding Wigner functions plots from the quantum tomography applied to the master equation are shown in the bottom row.

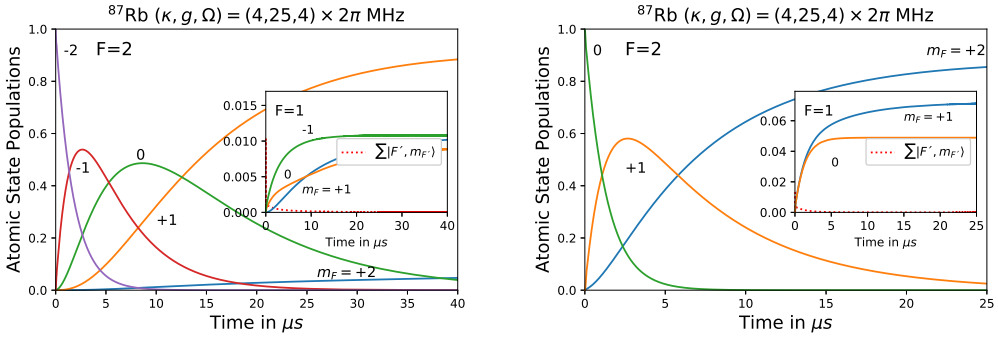

Figure 8.3: Atomic ground state populations ($F = 2$: main plot, $F = 1$: inset), and total excited state population (inset, red-dashed) as a function of time in the low coupling regime for $F = 2 \leftrightarrow F' = 1$ with initial state $m_F = -2$ (left) and $F = 2 \leftrightarrow F' = 2$ with initial state $m_F = 0$ (right).

Let us continue by discussing the atomic state populations in more detail. In Fig. 8.3 we show the time evolution of the atomic state populations for parameter sets that are the same as those in the output photon flux plots. The atomic population is seen to transfer smoothly and predominantly along the $F = 2$ ground state manifold from the initial state $|F = 2, m_F = -2\rangle$ (or $|F = 2, m_F = 0\rangle$) to the state $|F = 2, m_F = +1\rangle$ (or $|F = 2, m_F = +2\rangle$). In all cases, the excited state populations are very small, although the initial spike can get quite high.

A small amount of population makes it into the $F = 1$ manifold. For our mostly low driving (when compared to the hyperfine ground state splitting), it effectively remains trapped there, and we have somewhat constant populations of these states.

For $F = 2 \leftrightarrow F' = 1$ one can observe the population of the $|F = 2, m_F = +2\rangle$ state slowly growing, through a resonant Raman processes, thus making $|F = 2, m_F = +1\rangle$ not a truly dark state. The photon counting statistics do not show no trajectories with 4 counts because the $F' = 2$ manifold is eliminated and this process therefore not allowed.

8.3.3 High Coupling Regime

The two configurations from the low coupling regime can readily be taken to the high coupling regime. There is, however, a little twist for the atom starting in $|F = 2, m_F = -2\rangle$ and driven on resonance with the $F = 2 \leftrightarrow F' = 1$ transition, which will, now that the couplings are large enough, undergo a more effective Raman process between $|F = 2, m_F = 1\rangle$ and $|F = 2, m_F = 2\rangle$ through $|F = 2', m_F = 2\rangle$ (in complete analogy to the previous Section and Chapter 7), thus leading to a pulse with 4 photons. The rate of this additional process is proportional to

$$\lambda \propto \frac{\Omega^2 g^2}{\kappa \Delta^2}. \tag{8.3}$$

Apart from generating larger Fock states, this variant has the advantage that reversing it in an attempt to repeat the process should yield the same number of photons. When compared to the low g setups from before, this seems to be much less impacted by spontaneous emission see Figs. 8.4-8.5. For example, we virtually see no trajectories with a photoncount of 1 and the second-highest count number has a probability of around $2 \cdot 10^{-2}$, while the previous $F' = 1$ example recorded losses of three photons and had a probability of about 10^{-1} even though that one had a lower maximum photon number. This can be explained by the cooperativity being larger, such that the spontaneous emission is competing with a cavity coupling much larger than it. On top of that, the last step is a strong resonant Raman transition, for which spontaneous emission is effectively suppressed due to the negligible excited state population.

Note that a similar approach, for when $F = 2 \leftrightarrow F' = 2$ is resonantly driven from the initial state $m_F = -2$, is not practical. While theoretically it could circumvent the forbidden $|F = 2, m_F = 0\rangle \rightarrow |F' = 2, m_F = 0\rangle$ transition, what ends up effectively happening is that the atom still gets predominantly pumped to the $|F' = 2, m_F = 0\rangle$ level from where it can cycle back to $|F = 2, m_F = -1\rangle$ or decay by spontaneous emission to $|F = 2, m_F = 1\rangle$ (which

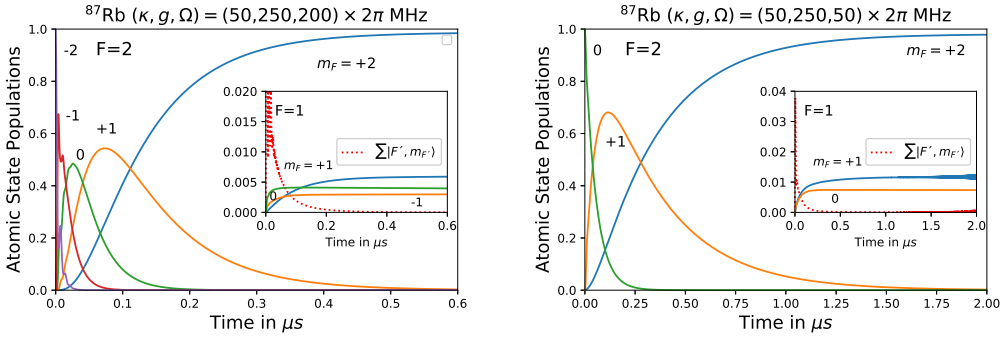

Figure 8.4: Atomic ground state populations ($F = 2$: main plot, $F = 1$: inset), and total excited state population (inset, red-dashed) as a function of time in the high coupling regime for $F = 2 \leftrightarrow F' = 1$ with initial state $m_F = -2$ (left) and $F = 2 \leftrightarrow F' = 2$ with initial state $m_F = 0$ (right).

corresponds to a 2 photon loss!). The rate of this process is much stronger than that of the Raman process, so that we actually enhance spontaneous emission and this is reflected in the photon statistics where 2 photons are more likely to be registered than 3, and almost as likely as 4, due to the aforementioned loss.

Even though the output photon flux and quantum trajectories of the 4-photon pulse indicate that it is a 4-photon state, the actual quantum state tomography does not properly reproduce the maxima and minima of the Wigner functions, thus the faded look in Fig. 8.5. Artificially lowering the $|F' = 2, m_F = 2\rangle$ state in our simulations seems to rectify this issue, suggesting that the Raman process' large detuning, i.e., the excited state manifold splitting is too large to easily filter the pulse appropriately.

The situation for the $F = 2 \leftrightarrow F' = 2$ remains qualitatively the same, just quantitatively the average output photon number is relatively speaking much closer to its ideal value.

Most of the discussion of the atomic state population in the low coupling regime still holds for the high coupling regime. There are differences in the populations of the $F = 1$- and $F = 2$-manifolds; in the high g regime at the end of the pulse, the $F = 1$ manifold population is overall lower and that of

$F = 2$ is higher when compared to the low coupling. This is because there the cooperativity is higher and thus dominates spontaneous emission more, which is the main source of population for $F = 1$. Moreover, due to the higher driving, these populations are subject to effective, resonant (spin-1) anti-Tavis-Cummings dynamics and slowly transferred to the state $|F = 1, m_F = +1\rangle$. From there, a far-off-resonant Raman transition eventually transfers this small population into the target state $|F = 2, m_F = +2\rangle$.

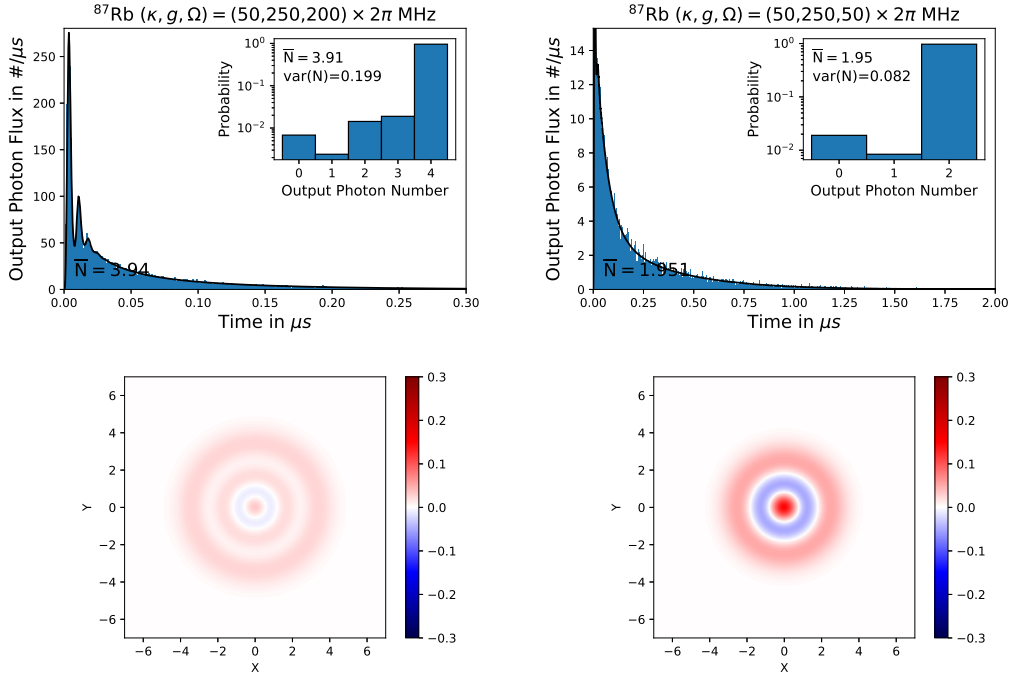

Figure 8.5: Output Photon Flux (top row) of a Rubidium atom prepared in $m_F = -2$ driven via $F = 2 \leftrightarrow F' = 1$ (left), and $m_F = 0$ driven via $F = 2 \leftrightarrow F' = 2$ (right). The lines represent the full master equation model (solid black). The histogram shows the temporal distribution of photocounts (renormalised to $\overline{N}$) for 10000 trajectories of the reduced model. The number below the curves represents the output photon number from the full model. The inset plots show the histogram of the photon number counts for the different quantum trajectories and includes the mean photon number plus the variance of the photocounts. Corresponding Wigner functions plots from the quantum tomography applied to the master equation are shown in the bottom row.

Table 8.1: Fidelities F of the reconstructed density operators relative to the target Fock state.

$\{\kappa, g\}/2\pi$	$\{4, 25\}$ MHz		$\{50, 250\}$ MHz	
$F \leftrightarrow F'$	$2 \leftrightarrow 1$	$2 \leftrightarrow 2$	$2 \leftrightarrow 1$	$2 \leftrightarrow 2$
F	0.808	0.741	0.290	0.874

8.3.4 Quantum Tomography

As before, we verify that the target quantum state has indeed been produced via quantum state tomography, although here this is done using the input-output formalism for quantum pulses [80] because of the complex-valued nature of the filter functions. The additional imaginary part of the filter function comes from the free evolution when the wave function is in a state with non-zero energy, which did not occur in the previous chapter because either the Tavis-Cummings model did not include any such terms or in the corresponding full model these states were barely populated. In general, the filter function can end up somewhat noisy, this is especially true for the high coupling case of the $F = 2 \leftrightarrow F' = 1$ transition. The resulting fidelities are compiled in table 8.1. Overall, our reconstructions always let us visually identify what the target was, i.e., correct number of rings for Fock states or correct number of Wigner-negative zones in the $0N$-states.

In Table 8.1 we display the fidelities of the reconstructed density operators. Comparing the results for the $F = 2 \leftrightarrow F' = 1$ and $F = 2 \leftrightarrow F' = 2$ transitions in the low coupling regime we see that the $F = 2 \leftrightarrow F' = 1$ transition performs better for the Fock state generation even though the photon number state is larger, this can be attributed to the, on average, higher Clebsch-Gordan coefficients for that transition. In the large coupling regime, $F = 2 \leftrightarrow F' = 1$ always gets outperformed by the $F = 2 \leftrightarrow F' = 2$ transition, however, this is due to the previously mentioned difficulty in filtering the state and the real fidelity should be higher, as the photon counting statistics suggest. Finally, $F = 2 \leftrightarrow F' = 2$ transition in the high coupling regime is better than in the low coupling regime by virtue of the higher cooperativity.

8.3.5 $F \leftrightarrow F' = F+1$ and the Cycling Transition

For the sake of completeness, we shall also briefly discuss the case of $F \leftrightarrow F' = F+1$ on the D_2 line (see Fig. 8.6). This transition has the benefit of having no roadblocks and can therefore produce 4 photons without relying on any off-resonant Raman process.

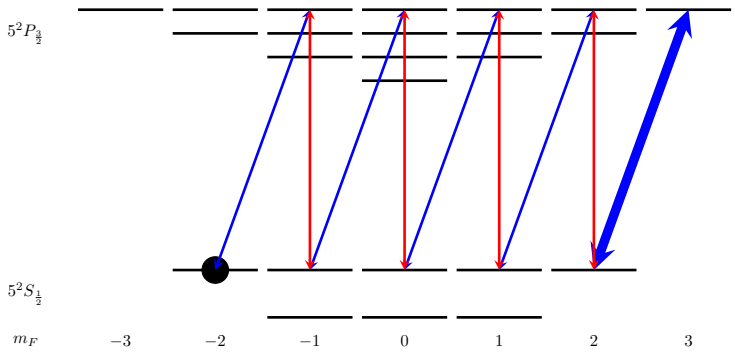

Figure 8.6: Depiction of the movement of the atom through the state manifold for the D_2 line. The black dot is the initial state that yields the pulse with the highest photon number. The dashed circle represents the final state. The thick line represents the cycling transition.

The integrated output photon flux, however, ends up being further from the ideal value of 4 than for $F = 2 \leftrightarrow F' = 1$ as can be seen in Fig. 8.7. This can be attributed to the higher spontaneous emission (both higher rate and higher Clebsch-Gordan coefficients) on the D_2 line and the absence of a Raman process, which is inherently more robust due to the detuning.

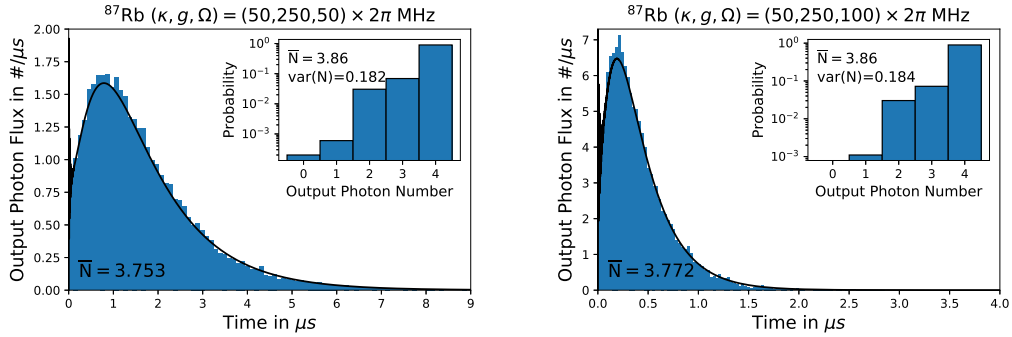

Figure 8.7: Output Photon Flux of a Rubidium atom prepared in $m_F = -2$ driven via $F = 2 \leftrightarrow F' = 3$ (right). The lines represent the full master equation model (solid black). The histogram shows the temporal distribution of photocounts (renormalised to $\overline{N}$) for 10000 trajectories of the reduced model. The number below the curves represents the output photon number from the full model. The inset plots show the histogram of the photon number counts for the different quantum trajectories and includes the mean photon number plus the variance of the photocounts.

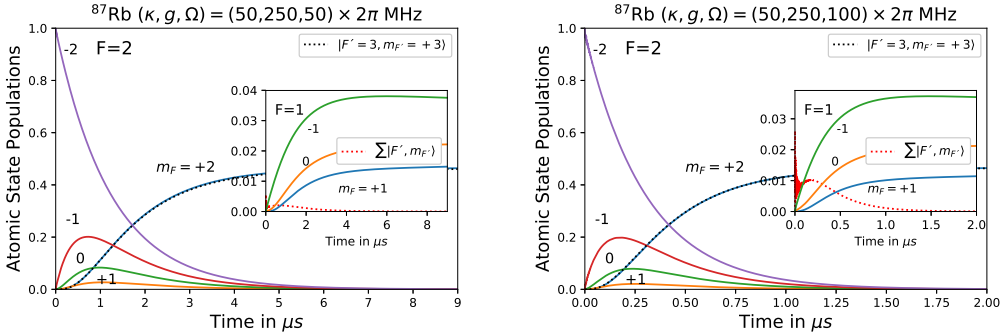

Figure 8.8: Atomic ground state populations ($F = 2$: main plot, $F = 1$: inset), and total excited state population (inset, red-dashed) as a function of time.

In contrast to the previously considered transitions, the output photon flux of this transition does not have an exponential shape, but rather displays something more alike to the superradiant shape. This can be understood by having a closer look at the transition strengths between two ground states, i.e.,

the product of the two dipole matrix elements

$$\lambda_{m_F,m_F+1} = \langle F, m_F|\mu_{+1}|F', m_F+1\rangle \times \langle F', m_F+1|\mu_0|F, m_F+1\rangle, \tag{8.4}$$

for the transition from m_F to m_F+1. For $F \leftrightarrow F' = F+1$, these grow monotonically as the atom traverses the state manifold, i.e.,

$$\lambda_{m_F,m_F+1} < \lambda_{m_F+1,m_F+2}, \tag{8.5}$$

while in the previous case from the D_1 line, they were decreasing monotonically. This is similar to the first half of the components of the spin raising or lowering operators $\hat{S}_\pm$ (although there the coefficients are mirrored around the centre), which are the origin of a similar pulse shape in the Dicke model. The same effect is also observed when driving $F = 3 \leftrightarrow F' = 4$ on the D_1 line.

The quantum state reconstruction for this transition, however, fails completely. The filter function ends up being even more rapidly oscillating than the previous cases. On top of that, using our argument about relative phases from before, there must be a relative phase of $-\frac{\pi}{2}$ between the states $|F = 2, m_F = 2\rangle$ and $|F' = 3, m_F = 3\rangle$. The atomic steady state is a mixture of these two states with non-negligible contribution of $|F' = 3, m_F = 3\rangle$ as can be seen in Fig. 8.8. The cavity field thus exits with a mixture of these two phases depending on the atomic state, which is a significant issue for superposition states.

8.4 $0N$-states and other Superpositions

Similar to the previous chapter, we may again start with a superposition of Zeeman levels of $F = 2$. For every level the atom goes through, it still incurs a phase shift of $-\frac{\pi}{2}$, which gets transferred to the output light pulse. Since here the excited states do not only get virtually populated, every photon emission corresponds to a two-level process (which means a phase shift of $-\pi$), therefore

all our pulses with even photon number states are unaffected, but for the $F = 2 \leftrightarrow F' = 1$ case, where we have 3 photons, the relative sign of the superposition is changed, which rotates the Wigner function by an angle -3π. This is different to the high detuning case, as there each photon emission was a simple transition between two levels due to being a Raman process. Since our 4-photon $0N$-state preparation includes one Raman process and 3 resonant processes, the relative phase is $-\frac{7\pi}{2}$.

The two reconstructed Wigner functions of the $0N$-states in Figs. 8.9-8.10 show a considerable rotation in the clockwise direction from their predicted orientation. This corresponds to a relative phase between the $|0\rangle$ and $|N\rangle$ parts. The origin of this phase is the sizeable population of states of the atom-cavity system, where the atom is in the off-resonant ground state manifold and the cavity is not empty. This either happens when spontaneous emission of a state with a photonic contribution decays to the lower ground state or through an off-resonant cavity transition, the latter one mainly being important in the high coupling regime. For low coupling, $F = 2 \leftrightarrow F' = 1$ has a much smaller phase difference from the theoretical prediction $\Delta\varphi = 0.1459$ than the $F = 2 \leftrightarrow F' = 2$ transition with $\Delta\varphi = 0.4264$. This can be explained by the population of $F = 1$ being more important in the case of the $F = 2 \leftrightarrow F' = 2$ transition. The same logic can also be applied if we compare the $F = 2 \leftrightarrow F' = 2$ transition for low and high coupling, i.e., for high coupling the $F = 1$ population is lower and so is the phase difference $\Delta\varphi = 0.2991$. $F = 2 \leftrightarrow F' = 1$ for high coupling is a bit peculiar as it has the lowest $F = 1$ population but also the highest phase difference $\Delta\varphi = 2.4980$. The $F = 1$ population is lower because of the higher driving strength, but that will also enable Raman processes on top of the final step, which add a different phase each step than their resonant counterpart. We also noticed that smoothening out some of the oscillations of the filter functions with a Gaussian filter can decrease the relative phase.

The first thing to notice about Table 8.2, is that again the $0N$-states, compared to the Fock states of the same configuration, sport a higher fidelity all across the board. In contrary to the number state generation, the $F = 2 \leftrightarrow F' = 2$ performs better because the 4 photon contributions of the $F = 2 \leftrightarrow$

Table 8.2: Fidelities F of the reconstructed density operators relative to the target ON-state. The fidelities take into account the added phase shifts.

$\{\kappa, g\}/2\pi$	$\{4, 25\}$ MHz		$\{50, 250\}$ MHz	
$F \leftrightarrow F'$	$2 \leftrightarrow 1$	$2 \leftrightarrow 2$	$2 \leftrightarrow 1$	$2 \leftrightarrow 2$
F	0.888	0.905	0.611	0.956

$F' = 1$ transition have more effect on the $0N$-state than in Fock state, i.e. the additional $|0\rangle\langle 4|$ and $|4\rangle\langle 0|$ components on top of the $|4\rangle\langle 4|$ component of the density operator.

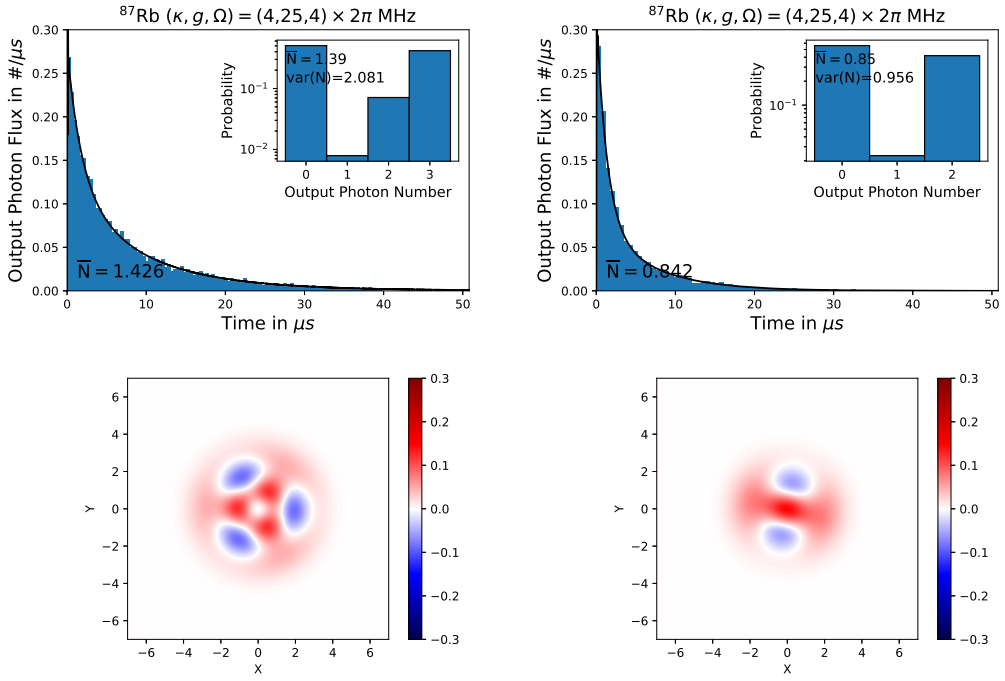

Figure 8.9: Output Photon Flux (top row) of a Rubidium atom prepared in equal superposition states of $m_F = -2$ and $m_F = 1$ driven via $F = 2 \leftrightarrow F' = 1$ (left), and of $m_F = 0$ and $m_F = 2$ driven via $F = 2 \leftrightarrow F' = 2$ (right). The lines represent the full master equation model (solid black). The histogram shows the temporal distribution of photocounts (renormalised to $\overline{\mathrm{N}}$) for 10000 trajectories of the reduced model. The number below the curves represents the output photon number from the full model. The inset plots show the histograms of the photon number counts for the different quantum trajectories and includes the mean photon number plus the variance of the photocounts. Corresponding Wigner functions plots from the quantum tomography applied to the master equation are shown in the bottom row.

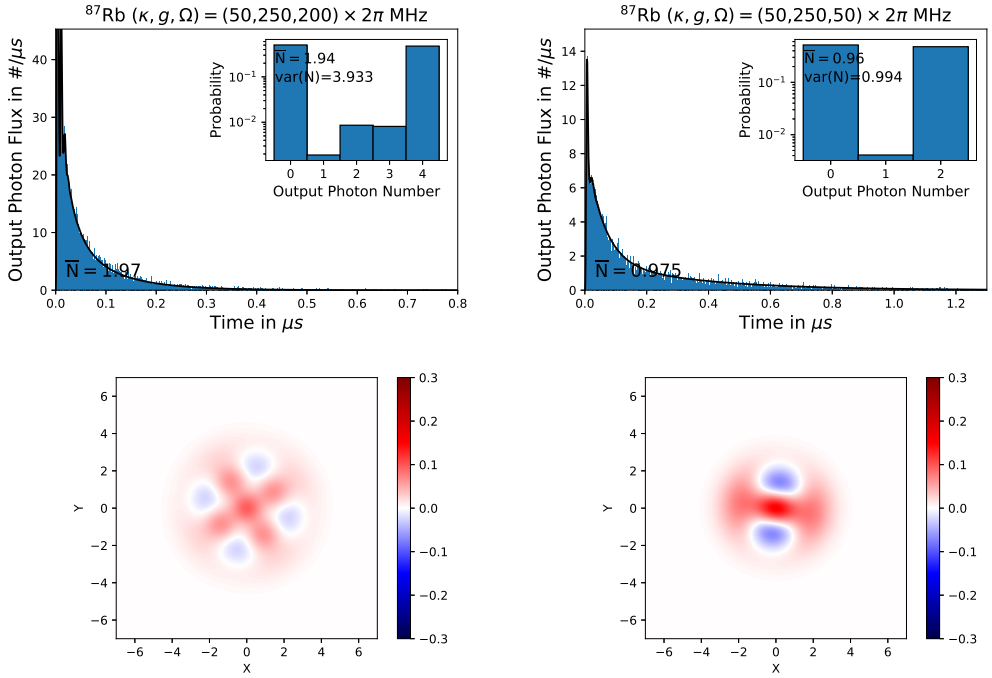

Figure 8.10: Output Photon Flux (top row) of a Rubidium atom prepared in equal superposition states of $m_F = -2$ and $m_F = 2$ driven via $F = 2 \leftrightarrow F' = 1$ (left), and of $m_F = 0$ and $m_F = 2$ driven via $F = 2 \leftrightarrow F' = 2$ (right). The lines represent the full master equation model (solid black). The histogram shows the temporal distribution of photocounts (renormalised to $\overline{\mathrm{N}}$) for 10000 trajectories of the reduced model. The number below the curves represents the output photon number from the full model. The inset plots show the histograms of the photon number counts for the different quantum trajectories and includes the mean photon number plus the variance of the photocounts. Corresponding Wigner functions plots from the quantum tomography applied to the master equation are shown in the bottom row.

8.5 Preparation of Entangled States

Since the lower ground state $F = 1$ is really far detuned, any part of the wave function in these states is essentially unaffected by the dynamics, especially in the low coupling regime, which we will be considering from now on. We exploit this by starting with an atom initially in a superposition of both ground states,

e.g.,

$$|\psi\rangle = \frac{1}{\sqrt{2}}\Big(|F=1, m_F=-1\rangle + |F=2, m_F=-1\rangle\Big). \tag{8.6}$$

We run our $F = 2 \leftrightarrow F' = 1$ scheme (see Fig. 8.11 for a schematic representation) to obtain a superposition of 0 and 2 photons conditioned on the atomic state, so the output photon number is entangled with the atomic state:

$$|\psi\rangle = \frac{1}{\sqrt{2}}\Big(|F=1, m_F=-1\rangle \otimes |0\rangle_{\text{out}} + |F=2, m_F=+1\rangle \otimes |2\rangle_{\text{out}}\Big). \tag{8.7}$$

This transition is chosen because $|F = 2, m_F = \pm 1\rangle$ are pseudo-dark states (also the reason why this is our initial state) and we already showed that this yields a satisfactory fidelity. Inverting the polarisation of the laser for the reverse operation yields

$$|\psi\rangle = \frac{1}{\sqrt{2}}\Big(|F=1, m_F=-1\rangle \otimes |0\rangle_{\text{out}}^{\otimes 2} + |F=2, m_F=-1\rangle \otimes |2\rangle_{\text{out}}^{\otimes 2}\Big). \tag{8.8}$$

Now, in addition to the aforementioned entanglement between the internal atomic state and photon number, the photon numbers of consecutive pulses are also entangled, i.e., if we measured the output photon number we would either have a sequence of 2 photons or no photons at all.

We can now disentangle the atom from the exact output photon number by mixing the atomic states with a microwave $\pi/2$-pulse which yields

$$\begin{aligned} |\psi\rangle = \frac{1}{\sqrt{2}}(&|F=1, m_F=-1\rangle \frac{|0\rangle_{\text{out}}^{\otimes 2} + |2\rangle_{\text{out}}^{\otimes 2}}{\sqrt{2}} \\ &+ |F=2, m_F=-1\rangle \frac{-|0\rangle_{\text{out}}^{\otimes 2} + |2\rangle_{\text{out}}^{\otimes 2}}{\sqrt{2}}). \end{aligned} \tag{8.9}$$

The entanglement has been transferred to these superposition states, that are

two of the maximally entangled Bell states, if we imagine for a moment that we could encode the logical $|0\rangle$ and $|1\rangle$ of a qubit on the states $|0\rangle_{\text{out}}$ and $|2\rangle_{\text{out}}$. A state measurement ($F = 1$ or $F = 2$) collapses the state of the propagating light into the corresponding Bell state. The dimensionality of this final superposition depends only on how often we invert the polarisation of the laser, which would give us the option to generate Greenberger-Horne-Zeilinger state [112], the generalisation of Bell states to higher dimensions.

The production of GHZ-like states is mainly limited by the fact that the losses to $F = 1$ or $|F = 2, m_F = \pm 2\rangle$ for every drive will accumulate for every switch of the polarisation, the former one leading to a loss in amplitude and the latter to some 3-photon contributions.

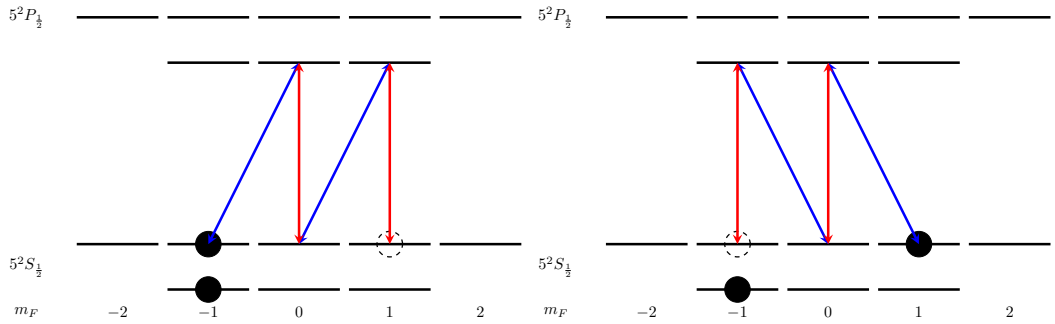

Figure 8.11: Depiction of the movement of the atoms through the state manifold. The black dot is the initial state, the dashed circle represent the final state of the upper half of the superposition.

8.6 Conclusions and Outlook

In this Chapter, we have shown that our deterministic single-atom source of N-photon pulses can readily be taken to resonance, if the emission into free space via spontaneous emission is dominated by the emission into the cavity. Overall, the fidelities obtained are a bit lower than those from before, especially considering the lower photon number of the output pulse, but our overall goal to demonstrate that such a scheme is feasible for low coupling cavities was

fulfilled. The pulses also end up happening on a much shorter time scale, which is a welcome addition.

Most of what we have shown here for ^{87}Rb will hold for similar atoms such as ^{133}Cs, where one could utilise the $F = 4 \leftrightarrow F' = 4$ and $F = 4 \leftrightarrow F' = 3$ transitions of the D_1 line. The output photon numbers would be doubled in that case. The larger hyperfine state splittings will also help by suppressing both resonant Raman transitions in the low coupling regime and off-resonant cavity deexcitation in the high coupling regime. Note that for the $F = 4 \leftrightarrow F' = 4$ transition, similar to the $F = 2 \leftrightarrow F' = 2$ transition in Rb, the Clebsch-Gordan coefficients going to $F = 3/F = 1$ are larger than the ones of the main paths, this circumstances is accentuated for ^{133}Cs, thus making this transition less ideal for low g. The bigger ground state manifolds open up the door to look at $F = 3 \leftrightarrow F' = 4$.

Chapter 9

Two-Mode Single-Atom Laser

9.1 Introduction

In an ordinary laser (light amplification by stimulated emission of radiation), a gain medium such as atoms is placed between two mirrors forming a cavity, in such a fashion that the emitted photons get reflected back through the medium leading to stimulated emission of additional photons.

Single-atom lasers are different in that the medium is now made up of one strongly coupled atom (or ion) instead of a lot of weakly coupled ones. Theoretical proposals and studies of such systems have been around since the early 90s [113–123]. They have recently been successfully implemented experimentally with a beam of ^{138}Ba atoms (technically multiple atoms, but they traverse the cavity one-by-one) [124, 125] and one-and-the-same ^{133}Cs atom [126], the latter implementation being the one we are interested in here. Recent investigations of single-atom lasers also include normal-superconductor quantum dot systems [127].

These experiments displayed sub-Poissonian photon statistics and anti-bunching. That means that these systems are potential candidates for single-photon sources, which are necessary prerequisites for quantum informatical applications such as quantum key distribution. Another exciting feature is the lack of a lasing threshold, a minimum pump strength above which a normal laser has to be driven so that lasing occurs.

In the original experiment [126], the ideal trajectory of the ^{133}Cs atom would be as follows: it would be driven with a laser from $F = 3$ to $F' = 3$. From there it will decay to $F = 4$, while emitting a photon into the cavity. Then it gets driven by another laser to $F' = 4$. The scheme relied on spontaneous emission back to $F = 3$ to enable the next round trip (Fig. 9.1, left).

We are now interested in expanding this idea to the two-cavity-mode case, where the atom no longer relies on spontaneous emission in the last step, but rather is strongly coupled to a second cavity mode. This is made possible by the relatively small free spectral range of novel fibre cavities [110, 128] that allow for the simultaneous strong coupling to two π-polarised cavity modes $\hat{a}$ and $\hat{b}$, roughly separated by the ground state hyperfine splitting ω_{HF}. In a current nanofibre cavity QED setup [128], the modes $\hat{a}$ and $\hat{b}$ end up being red- and blue-detuned by $\Delta = 2\pi \times 60$ MHz from their respective atomic resonances. This is the closest to resonance the free spectral range allows for now in the experiment. The cavity has single-atom coupling strengths $g = 2\pi \times 9$ MHz and cavity linewidths $\kappa = 2\pi \times 5$ MHz.

We consider a single ^{133}Cs atom trapped in a dipole trap and driven by σ_+- and σ_--polarised lasers with frequencies ω_3 and ω_4 respectively. The frequencies ω_3 and ω_4 are chosen to be red- and blue-detuned by the same amount as the frequencies of the corresponding cavity modes going to the same excited state. For a schematic representation of the transition (Fig. 9.1, right). The trap is positioned in the evanescent field of a tapered optical nanofibre between two fibre-Bragg gratings, which forms the aforementioned cavity.

With the addition of the second strongly-coupled cavity mode, this system has the potential to behave as a quasi-deterministic two-photon source. In this Chapter, we give a thorough analysis of its emission properties.

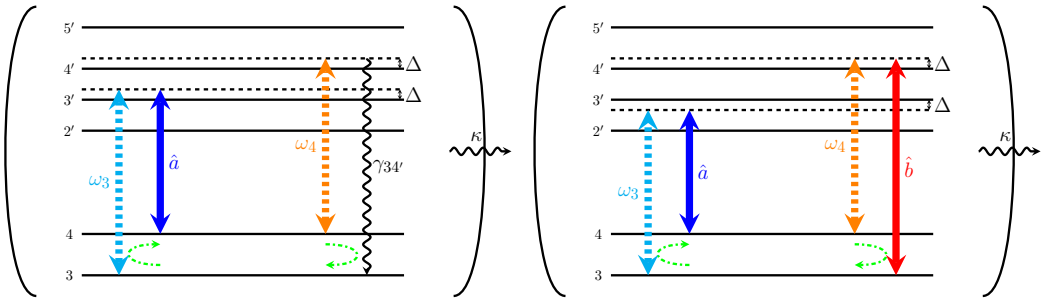

Figure 9.1: Schematic Representations of the laser and cavity transition arrangement from the experiment in [126] (left) and the one we are now considering (right). Zeeman sublevels are not shown.

9.2 Full Model

The Hamiltonian for this system reads ($\hbar = 1$)

$$\begin{aligned}
\hat{H} = {} & \omega_a \hat{a}^\dagger \hat{a} + \omega_b \hat{b}^\dagger \hat{b} - \omega_{HF} |3\rangle\langle 3| \\
& + \omega_{2'} |2'\rangle\langle 2'| + \omega_{3'} |3'\rangle\langle 3'| + \omega_{4'} |4'\rangle\langle 4'| + \omega_{5'} |5'\rangle\langle 5'| \\
& + \frac{\Omega e^{i\omega_3 t}}{2} (|3\rangle\langle 2'|_- + |3\rangle\langle 3'|_- + |3\rangle\langle 4'|_-) + H.c. \\
& + \frac{\Omega e^{i\omega_3 t}}{2} (|3\rangle\langle 2'|_+ + |3\rangle\langle 3'|_+ + |3\rangle\langle 4'|_+) + H.c. \\
& + \frac{\Omega e^{i\omega_4 t}}{2} (|4\rangle\langle 3'|_- + |4\rangle\langle 4'|_- + |4\rangle\langle 5'|_-) + H.c. \\
& + \frac{\Omega e^{i\omega_4 t}}{2} (|4\rangle\langle 3'|_+ + |4\rangle\langle 4'|_+ + |4\rangle\langle 5'|_+) + H.c. \\
& + g\hat{a} (|4\rangle\langle 3'|_\pi + |4\rangle\langle 4'|_\pi + |4\rangle\langle 5'|_\pi) + H.c. \\
& + g\hat{b} (|3\rangle\langle 2'|_\pi + |3\rangle\langle 3'|_\pi + |3\rangle\langle 4'|_\pi) + H.c.,
\end{aligned} \tag{9.1}$$

where we have already removed all the terms corresponding to very far off-resonant processes, i.e., those detuned by the large ground state hyperfine splitting (e.g., we neglect the coupling of mode $\hat{a}$ to the $|3\rangle \leftrightarrow |2', 3', 4'\rangle$ transitions). We have also absorbed the dipole transition elements and the different Zeeman sublevels into the $|i\rangle\langle i|_+$, where the subscript specifies the polarisation of the transitions, and we assume the same Rabi frequency Ω for each laser field. We consider the system to be open and introduce cavity decay at a rate

κ and spontaneous emission at a rate γ. The different spontaneous emission channels ($\pi, \sigma_\pm$ for each $F' \to F$ transition) are taken to be independent, leading to the following master equation

$$\begin{aligned}\dot{\hat{\rho}} = &-i\Big[\hat{H},\hat{\rho}\Big]+\kappa\mathcal{D}[\hat{a}]\hat{\rho}+\kappa\mathcal{D}[\hat{b}]\hat{\rho}\\ &+\frac{\gamma}{2}\mathcal{D}[|3\rangle\langle 2'|_\pi]\hat{\rho}+\frac{\gamma}{2}\mathcal{D}[|3\rangle\langle 3'|_\pi]\hat{\rho}+\frac{\gamma}{2}\mathcal{D}[|3\rangle\langle 4'|_\pi]\hat{\rho}\\ &+\frac{\gamma}{2}\mathcal{D}[|4\rangle\langle 5'|_\pi]\hat{\rho}+\frac{\gamma}{2}\mathcal{D}[|4\rangle\langle 3'|_\pi]\hat{\rho}+\frac{\gamma}{2}\mathcal{D}[|4\rangle\langle 4'|_\pi]\hat{\rho}\\ &+\frac{\gamma}{2}\mathcal{D}[|3\rangle\langle 2'|_-]\hat{\rho}+\frac{\gamma}{2}\mathcal{D}[|3\rangle\langle 3'|_-]\hat{\rho}+\frac{\gamma}{2}\mathcal{D}[|3\rangle\langle 4'|_-]\hat{\rho}\\ &+\frac{\gamma}{2}\mathcal{D}[|4\rangle\langle 5'|_-]\hat{\rho}+\frac{\gamma}{2}\mathcal{D}[|4\rangle\langle 3'|_-]\hat{\rho}+\frac{\gamma}{2}\mathcal{D}[|4\rangle\langle 4'|_-]\hat{\rho}\\ &+\frac{\gamma}{2}\mathcal{D}[|3\rangle\langle 2'|_+]\hat{\rho}+\frac{\gamma}{2}\mathcal{D}[|3\rangle\langle 3'|_+]\hat{\rho}+\frac{\gamma}{2}\mathcal{D}[|3\rangle\langle 4'|_+]\hat{\rho}\\ &+\frac{\gamma}{2}\mathcal{D}[|4\rangle\langle 5'|_+]\hat{\rho}+\frac{\gamma}{2}\mathcal{D}[|4\rangle\langle 3'|_+]\hat{\rho}+\frac{\gamma}{2}\mathcal{D}[|4\rangle\langle 4'|_+]\hat{\rho}.\end{aligned} \tag{9.2}$$

9.2.1 Interaction Picture

For our numerical simulations, the large ground state hyperfine splitting (around 9.2 GHz) is problematic, as it makes the problem 'stiff', i.e., having time scales very different from each other (the coupling strengths are in the MHz range). Therefore, we transform the full Hamiltonian (9.1) into the interaction picture using the transformation Hamiltonian

$$\begin{aligned}\hat{H}_T = &(\omega_3-\omega_{HF})\hat{a}^\dagger\hat{a}+(\omega_4+\omega_{HF})\hat{b}^\dagger\hat{b}+(\omega_3-\omega_{HF})\sum_{F'}|F'\rangle\langle F'|\\ &+(\omega_3-\omega_4-2\omega_{HF})|3\rangle\langle 3|.\end{aligned} \tag{9.3}$$

The Hamiltonian in this new frame is given by

$$\begin{aligned}\hat{V} = &\delta|3\rangle\langle 3|+(\Delta+\omega_{2'3'})|2'\rangle\langle 2'|+\Delta|3'\rangle\langle 3'| \\ &+(\Delta+\omega_{3'4'})|4'\rangle\langle 4'|+(\Delta+\omega_{3'4'}+\omega_{4'5'})|5'\rangle\langle 5'| \\ &+\frac{\Omega e^{-i\delta t}}{2}(|3\rangle\langle 2'|_-+|3\rangle\langle 3'|_-+|3\rangle\langle 4'|_-)+H.c. \\ &+\frac{\Omega e^{-i\delta t}}{2}(|3\rangle\langle 2'|_++|3\rangle\langle 3'|_++|3\rangle\langle 4'|_+)+H.c. \\ &+\frac{\Omega e^{i\delta t}}{2}(|4\rangle\langle 3'|_-+|4\rangle\langle 4'|_-+|4\rangle\langle 5'|_-)+H.c. \\ &+\frac{\Omega e^{i\delta t}}{2}(|4\rangle\langle 3'|_++|4\rangle\langle 4'|_++|4\rangle\langle 5'|_+)+H.c. \\ &+g\hat{a}(|4\rangle\langle 3'|_\pi+|4\rangle\langle 4'|_\pi+|4\rangle\langle 5'|_\pi)+H.c. \\ &+g\hat{b}(|3\rangle\langle 2'|_\pi+|3\rangle\langle 3'|_\pi+|3\rangle\langle 4'|_\pi)+H.c.,\end{aligned} \tag{9.4}$$

where we define

$$\delta = 2\Delta+\omega_{3'4'} \tag{9.5}$$

and the energy difference between the excited levels

$$\omega_{ij} = \omega_j-\omega_i. \tag{9.6}$$

The transformation does not affect the dissipative part of the Master equation.

9.3 Atomic Populations and Intracavity Photon Number

For the numerical integration of the master equation, we start with the atom initially in a mixed state with equal populations of all Zeeman sublevels of the

lower ground state, i.e.,

$$\hat{\rho}_0 = \frac{1}{7} \sum_{m_F=-3}^{3} |F=3, m_F\rangle\langle F=3, m_F| \otimes |0\rangle\langle 0|_a \otimes |0\rangle\langle 0|_b \tag{9.7}$$

if using the full model (or in $|F=3\rangle$ when using one of the 4-state models later in the Chapter). Both cavity modes are initially in the vacuum state. For trajectory simulations of the full model, we start with the atom in a random Zeeman level of the lower ground state, unless we only do a single trajectory, in which case we start with an equal superposition of all of them.

9.3.1 Varying the Laser Strengths

We start by looking at what happens if we vary the strength of the lasers in our system. Fig. 9.2 shows the population of various hyperfine manifolds. For low field strengths, the population of the initial state $F = 3$ remains dominant. As we get further from that condition, the populations of the two ground states become equal, and the excited state populations start to become important. Note also that for very large driving strengths, the population of the upper ground may even surpass that of the lower. Fig. 9.3 shows the behaviour of the photon number for the same set of parameters. The populations of the cavity modes in the steady state are mainly equal unless the driving laser becomes strong, in which case the mode $\hat{b}$ ends up being slightly more populated on average. The initially larger population of mode $\hat{a}$ is due to the atom starting in $F = 3$, from which that mode is the first to be excited.

For the corresponding trajectory picture, that means that on average the atom stays longer in $F = 3$. The noise on the curve corresponds to spontaneous emission events. Every jump with one of the cavity mode annihilation operators cements the two photon transition and comes thus with a switch in ground state and cavity population. The same is true for spontaneous emission decaying to a ground state different from the one it came from. The frequency of this swapping increases as the laser driving increases. For low driving, jumps are infrequent, for intermediate there is a regular occurrence, and in the

high driving limit the trajectory becomes quite erratic as spontaneous emission dominates.

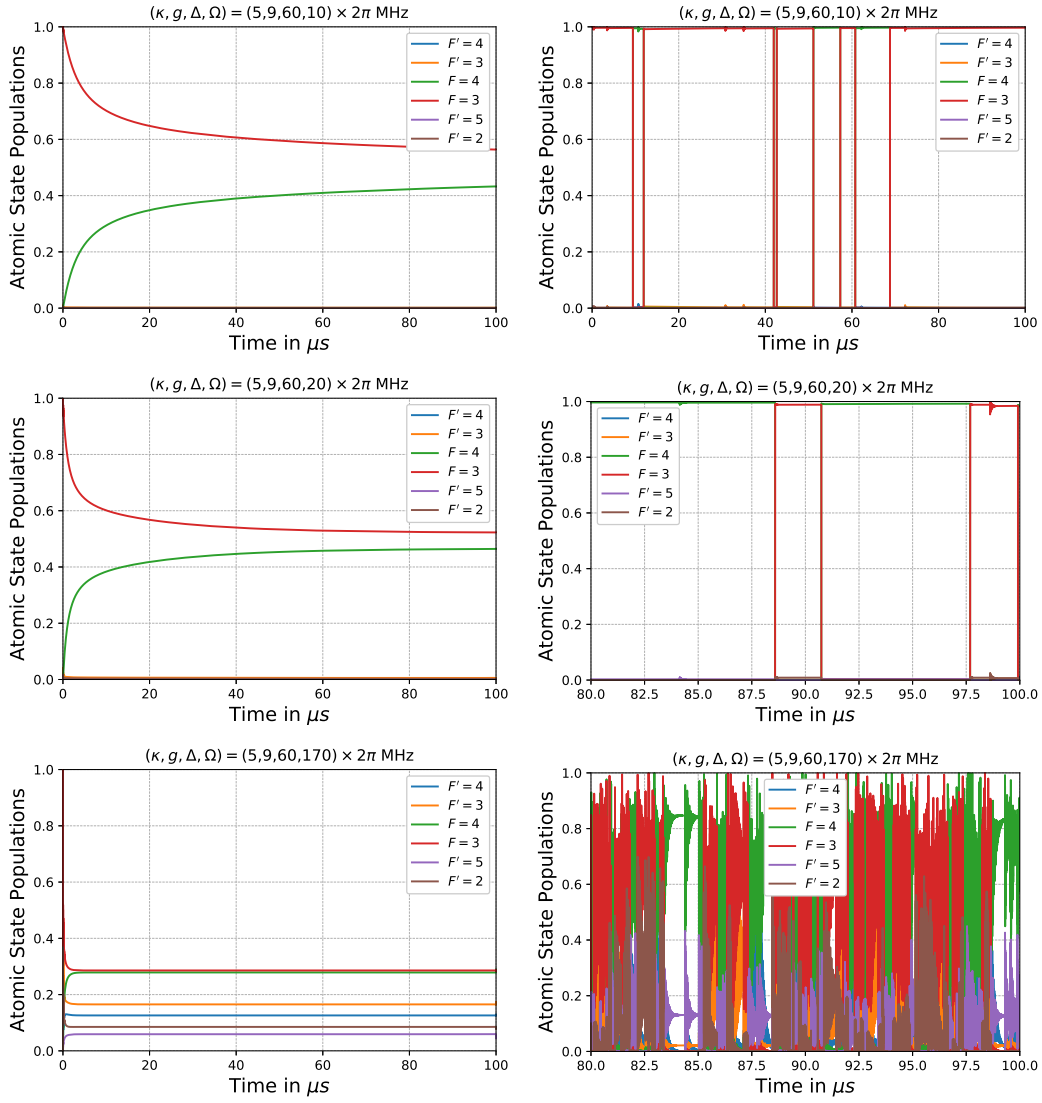

Figure 9.2: Atomic state populations from the Master equation (left column) and for a single quantum trajectory (right column) as a function of time for varying driving strengths Ω.

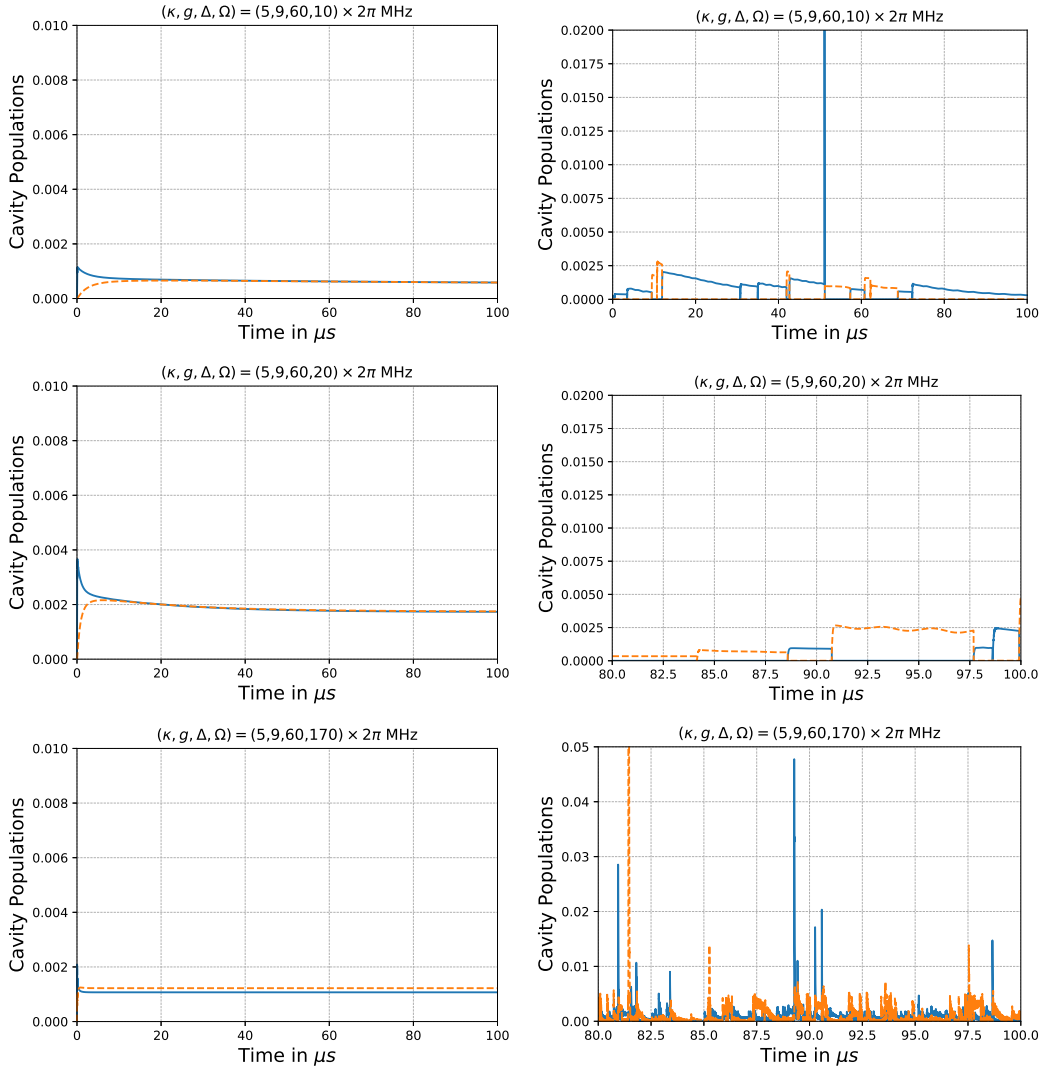

Figure 9.3: Average photon number $\langle \hat{a}^\dagger \hat{a} \rangle$ (solid blue) and $\langle \hat{b}^\dagger \hat{b} \rangle$ (dashed orange) from the Master equation (left column) and for a single quantum trajectory (right column) as a function of time for varying driving strengths Ω.

9.3.2 Varying the Detunings

In contrast to higher laser strengths, lower detunings do not cause the steady state excited state populations to become more important, even though they are quite important in the initial dynamics, as can be seen in the first row of Fig. 9.4. This hints toward the atom reaching a state that is close to being dark. In the trajectory picture, this results in jumps becoming less prevalent

as we approach resonance.

The master equation solutions suggest that the steady state populations of the cavity modes stay roughly equal (Fig. 9.5). Looking at a single trajectory, we see again that the frequency of jumps diminishes closer to resonance.

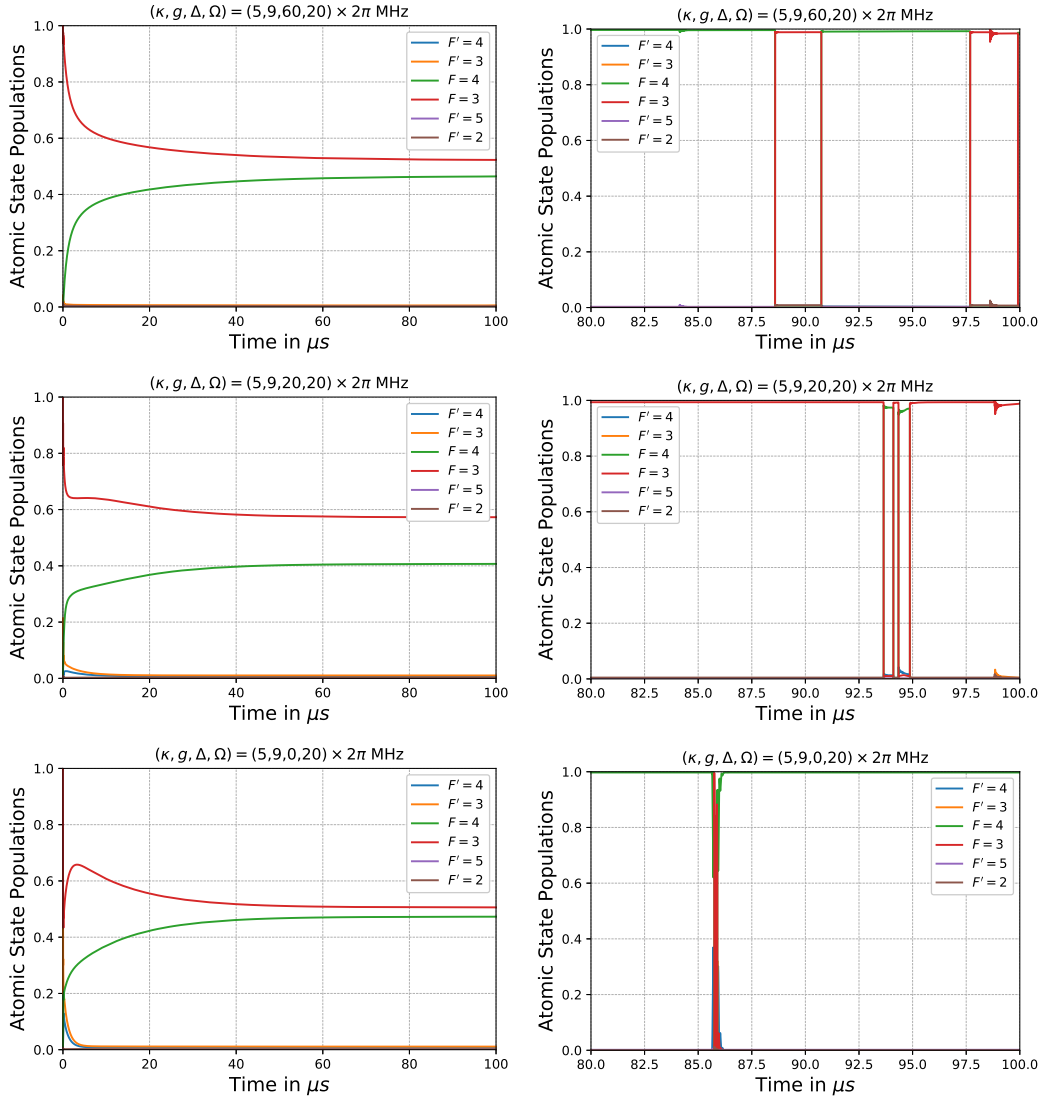

Figure 9.4: Atomic state populations from the Master equation (left column) and for a single quantum trajectory (right column) as a function of time for varying detuning Δ.

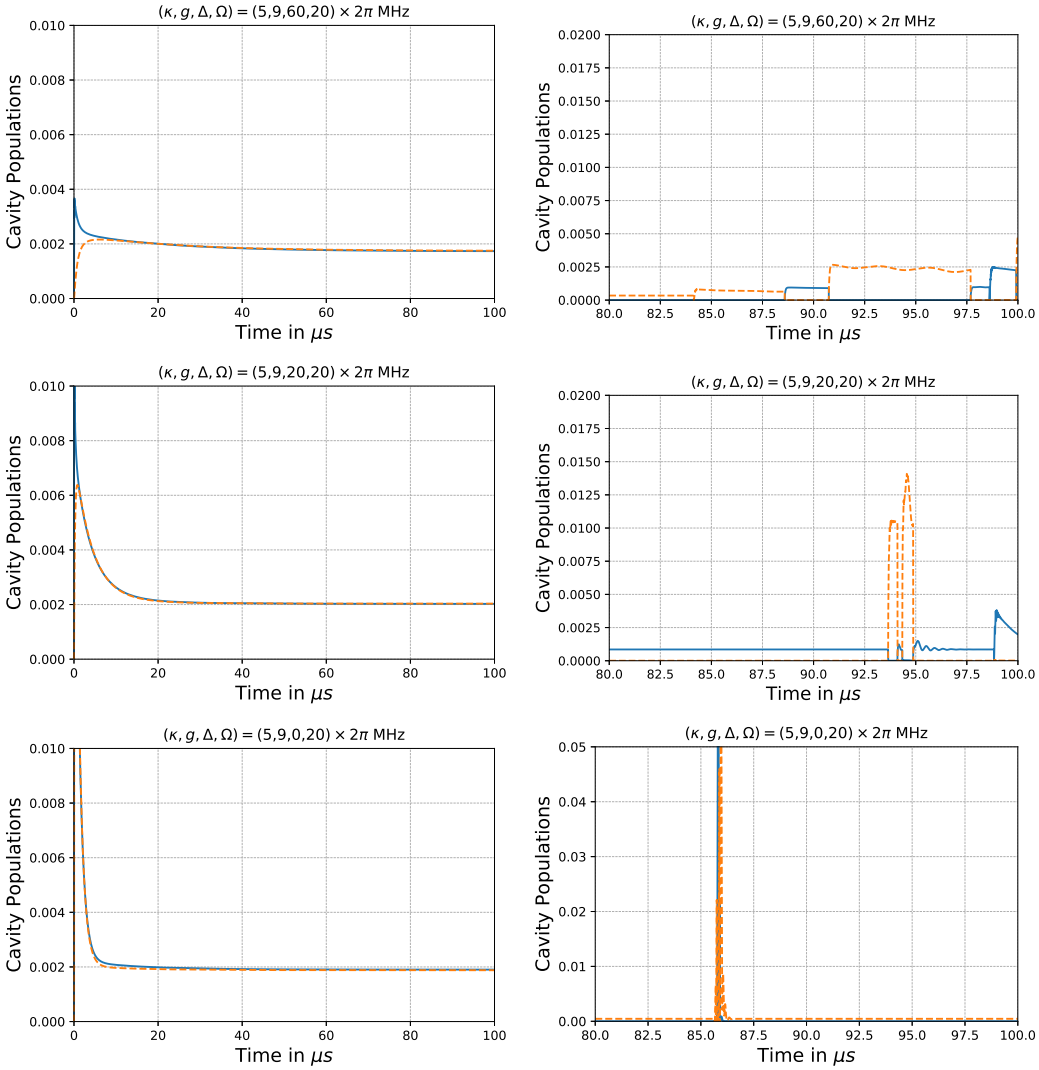

Figure 9.5: Average photon number $\langle \hat{a}^\dagger \hat{a} \rangle$ (solid blue) and $\langle \hat{b}^\dagger \hat{b} \rangle$ (dashed orange) from the Master equation (left column) and for a single quantum trajectory (right column) as a function of time for varying detuning Δ.

9.3.3 Varying the Atom-Cavity Coupling Strength

The cavity coupling strength is a parameter that is not easily tunable experimentally, but it is imaginable that in the future slight increases can be realised. In contrast to increasing the laser strength, the increased cavity coupling leads to an increased splitting of the ground state populations. Also, spontaneous emission should become less prevalent because the cavity transitions are in

stronger competition with them.

Since the cavity coupling strength is quite small to begin with (relative to the driving), increasing it can only accelerate the dynamics and thus increase the cavity photon number. If it was increased further, we would expect this to decrease the photon number as well because vacuum Rabi oscillations between the cavity modes and the atom could be expected to occur.

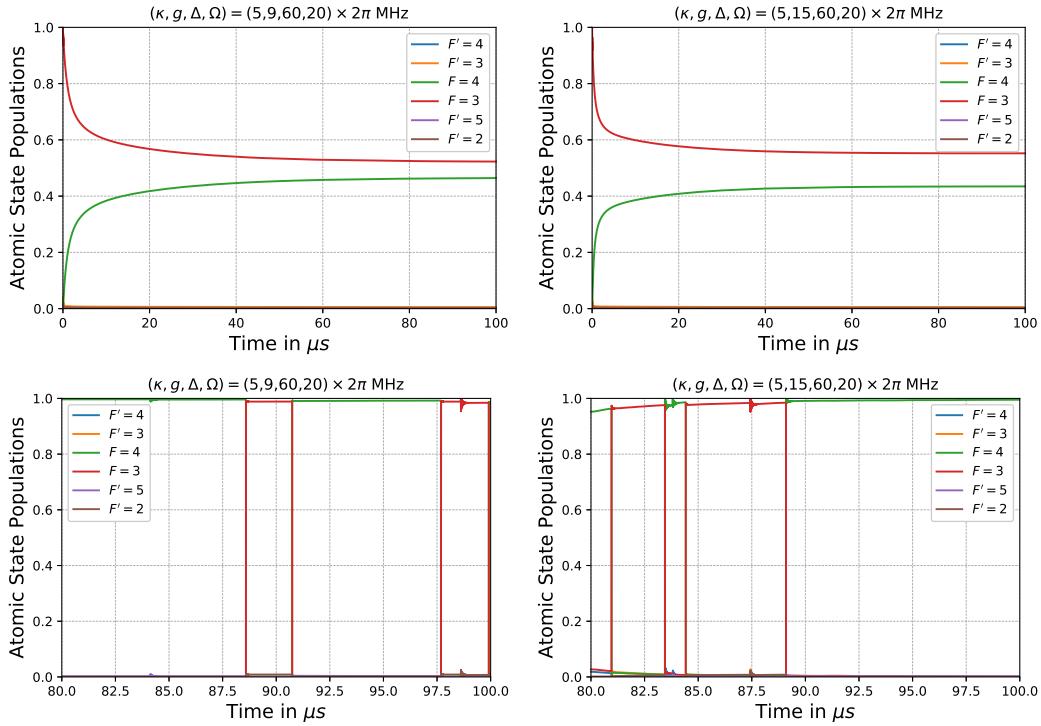

Figure 9.6: Atomic state populations from the Master equation (first row) and for a single quantum trajectory (second row) as a function of time for varying coupling strength g.

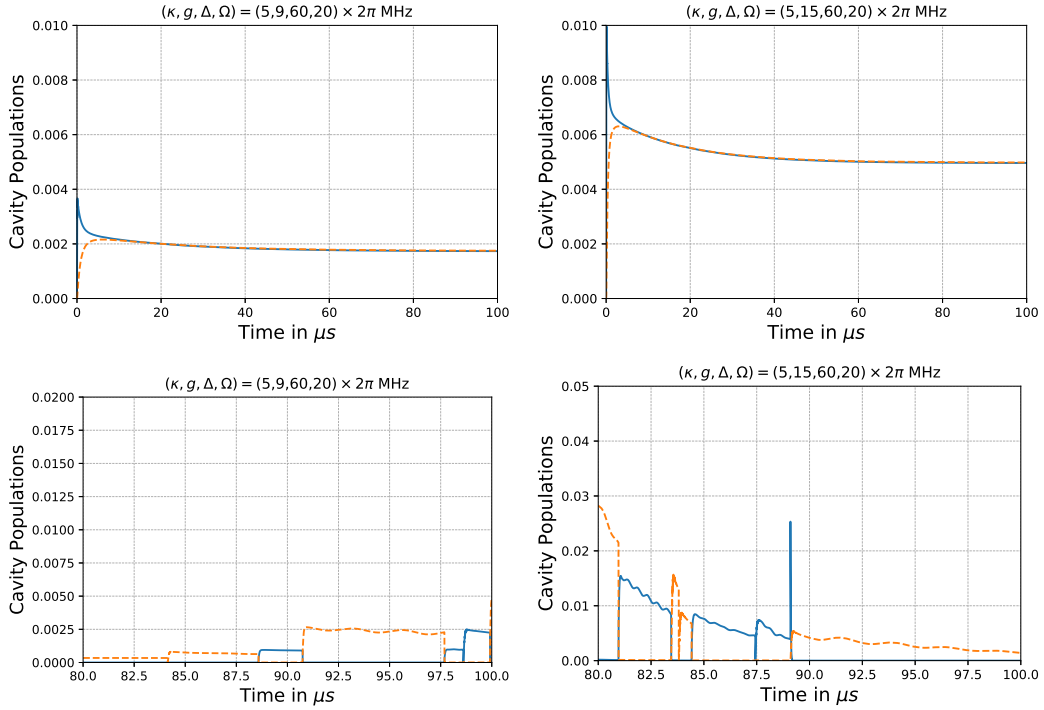

Figure 9.7: Average photon number $\langle \hat{a}^\dagger \hat{a} \rangle$ (solid blue) and $\langle \hat{b}^\dagger \hat{b} \rangle$ (dashed orange) from the Master equation (first row) and for a single quantum trajectory (second row) as a function of time for varying coupling strength g.

9.4 Photon Statistics

9.4.1 Inference from Photoelectric Counts

We use the method outlined in [126], where the photonic intensity correlation functions are reconstructed from the coincidence of photoelectric counts. We simulate N trajectories of a single atom for a duration T with y time steps. We record the times at which photons are emitted from one of the cavity modes. These times are then converted into histograms with a bin number equal to the number of time steps, meaning we only have a count number c that is equal to either one or zero in each bin. This is done for each cavity mode separately, giving us two lists of photoelectric events $(c_0^a, c_1^a, ..., c_{y-1}^a)$ and $(c_0^b, c_1^b, ..., c_{y-1}^b)$.

We compute the coincidence function for the rth trajectory through

$$n_{ij}^{(r)}(k) = \sum_m c_m^i c_{m+k}^j \qquad i,j \in \{a,b\}, \tag{9.8}$$

and sum the results of all trajectories up to a total coincidence function

$$n_{ij}(\tau) = \sum_r n_{ij}^{(r)}(\tau) \qquad i,j \in \{a,b\}. \tag{9.9}$$

Because of the high resolution, the coincidence function is most of the time zero or 1 and therefore quite noisy. We smoothen the coincidence function by convolving it with a Gaussian function. Fig. 9.8 shows both the raw output of this procedure and how a convolution of it leads to more telling data sets. Furthermore, in the case where we want to compute the coincidence for photons of the same mode, we have to set the 0th element of the coincidence function manually to zero as otherwise we are coinciding the photon with itself in that case.

The correlation function can be computed from the coincidence function through

$$g_{ij}^{(2)}(\tau) = \frac{n_{ij}(\tau)}{R_i R_j N T \epsilon}, \qquad i,j \in \{a,b\} \tag{9.10}$$

where R_a and R_b are the counting rates, i.e., the integral over the output photon flux $2\kappa\langle\hat{a}^\dagger\hat{a}\rangle$ (average over all trajectories) divided by the observation time of the two modes,

$$\begin{aligned} R_a &= \frac{2\kappa}{T}\int_0^T dt\langle\hat{a}^\dagger\hat{a}\rangle, \\ R_b &= \frac{2\kappa}{T}\int_0^T dt\langle\hat{b}^\dagger\hat{b}\rangle, \end{aligned} \tag{9.11}$$

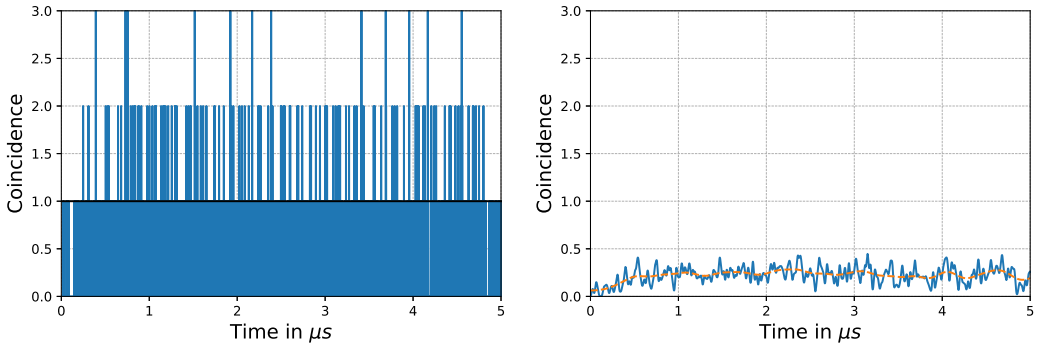

Figure 9.8: Exemplary raw coincidence function (left) and convoluted with a selection of Gaussian filters (right) of standard deviation $\sigma = 10$ ns (blue solid) and $\sigma = 100$ ns (orange dashed).

and $\epsilon = \frac{T}{y}$ is the time resolution.

The observation time starts after the system has reached the steady state. The first event is recorded if it happens before a time T after the start of the record and the second event happens up to T afterwards (so at most $2T$ after the start).

Alternatively, we can also choose to start to record from the point in time when the lasers are turned on, but then a large time is required to compensate for the initial dynamics to reach the same normalisation as the steady state case.

9.4.2 Intensity Correlation Functions

The zero-delay correlation functions

$$g_{ab}^{(2)}(0) = \frac{\langle \hat{a}^\dagger \hat{b}^\dagger \hat{b} \hat{a} \rangle_{SS}}{\langle \hat{a}^\dagger \hat{a} \rangle_{SS} \langle \hat{b}^\dagger \hat{b} \rangle_{SS}}. \tag{9.12}$$

can be obtained from solving the master equation to the steady state once and give us a rough idea of how the correlation functions behave for a certain selection of parameters. Some results are given in Fig. 9.9 for a variety of parameter sets.

Our expectations for the light emitted from the cavity are that the two

autocorrelation functions should still display sub-Poissonian photon statistics and be antibunched, since the situation is virtually the same as in [126] for one of the modes and there is no reason the newly added mode should behave any different. The crosscorrelations between the two modes, on the other hand, we expect to show super-Poissonian statistics due to the atom ideally traversing the level structure in clockwise fashion and thus emitting photons into the cavity in alternation. As we can see in Figs. 9.9 and 9.10 these expectations are mostly met. We can also observe that the autocorrelation functions show excess fluctuations $g^{(2)}(\tau) > 1$ for intermediate time delays τ (Fig. 9.10). This can be understood as the fact that after a time of the order of the average round trip, time observing a photon from the same mode is more likely. This effect could already be observed in [126] and disappears as the detuning is decreased or the laser strength is increased, but becomes more prominent with the higher cavity coupling. The crosscorrelations show both antibunching for very small time delays and bunching after that initial rise.

The only time we can see a departure from this behaviour is when we approach resonance or when the driving laser intensity becomes very strong, as can be seen in the second row of Figs. 9.9 and 9.11. Then, there is no more sub-Poissonian statistics of the autocorrelation. For comparison, in the experiment [126] all fields were blue-detuned by at least $2\pi \times 9$ MHz. For low detunings this can be remedied to some degree by increasing the cavity linewidth κ to ensure that the photons leave the cavity fast enough to suppress reexcitation processes from the cavity, as illustrated by the bottom plot in Fig. 9.9.

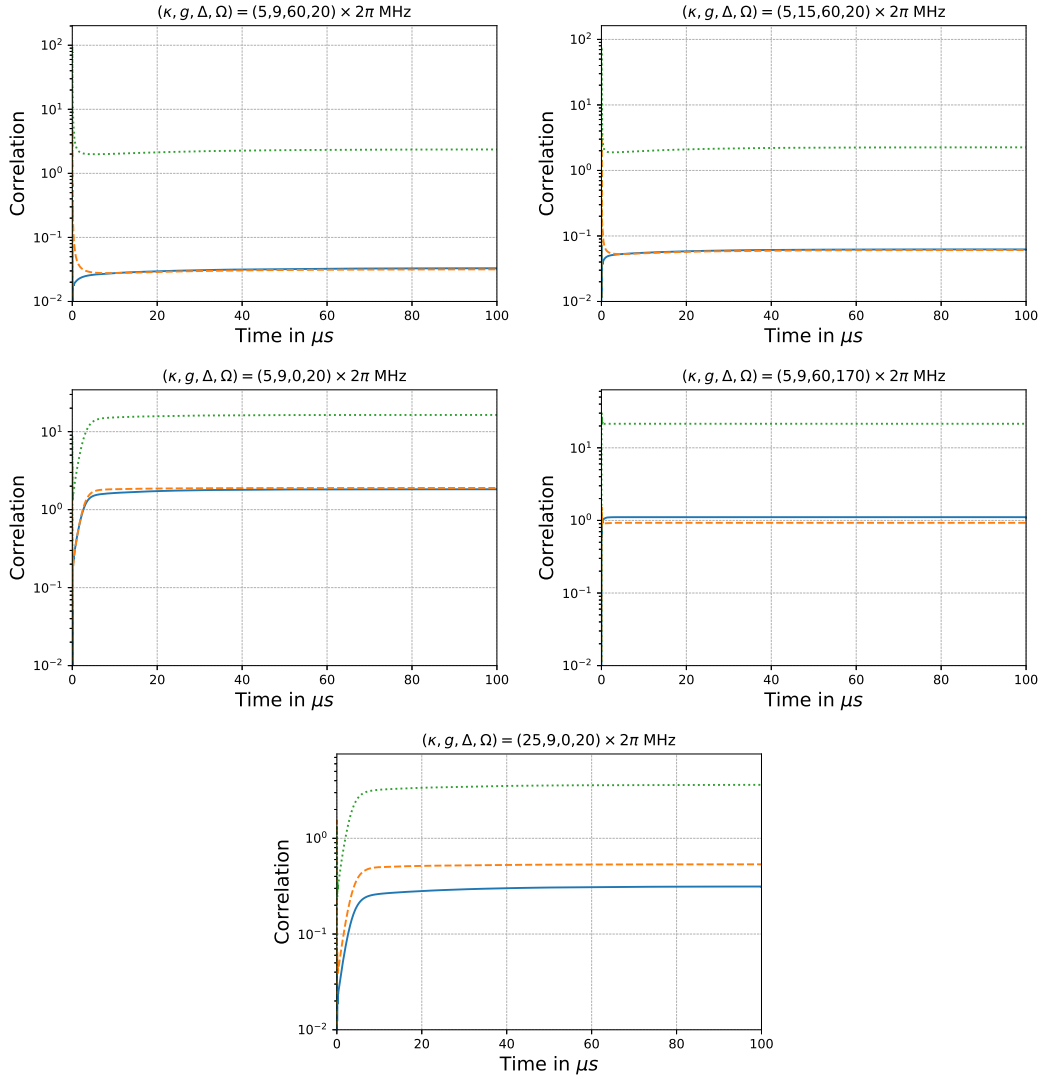

Figure 9.9: Zero-delay correlation functions $g^{(2)}_{aa}(0)$ (solid blue), $g^{(2)}_{bb}(0)$ (dashed orange) and $g^{(2)}_{ab}(0)$ (dotted green) as a function of time obtained from the master equation.

We can also observe an asymmetry between the two crosscorrelations, which can be explained by the two processes putting photons into the two cavities happening at different rates, i.e., $\Omega_{44'}g_{34'} > \Omega_{33'}g_{43'}$ (using the relative hyperfine transition strengths [50], explicit values for these parameters will be derived at a later stage). So for a given time delay, it is more likely to observe a photon in mode $\hat{b}$ after having observed in mode $\hat{a}$ than the other way around. This directly translates to $g^{(2)}_{ab}(\tau) > g^{(2)}_{ba}(\tau)$ for the crosscorrelation functions.

The peak in the crosscorrelation function also gives us an idea of the characteristic time of one half of a round trip. It is also worth noting that the time scale τ over which the correlation functions become coherent ($g^{(2)}(\tau) \to 1$) is approximately the same. When the autocorrelation functions are affected by excess fluctuations, they will converge before reaching 1.

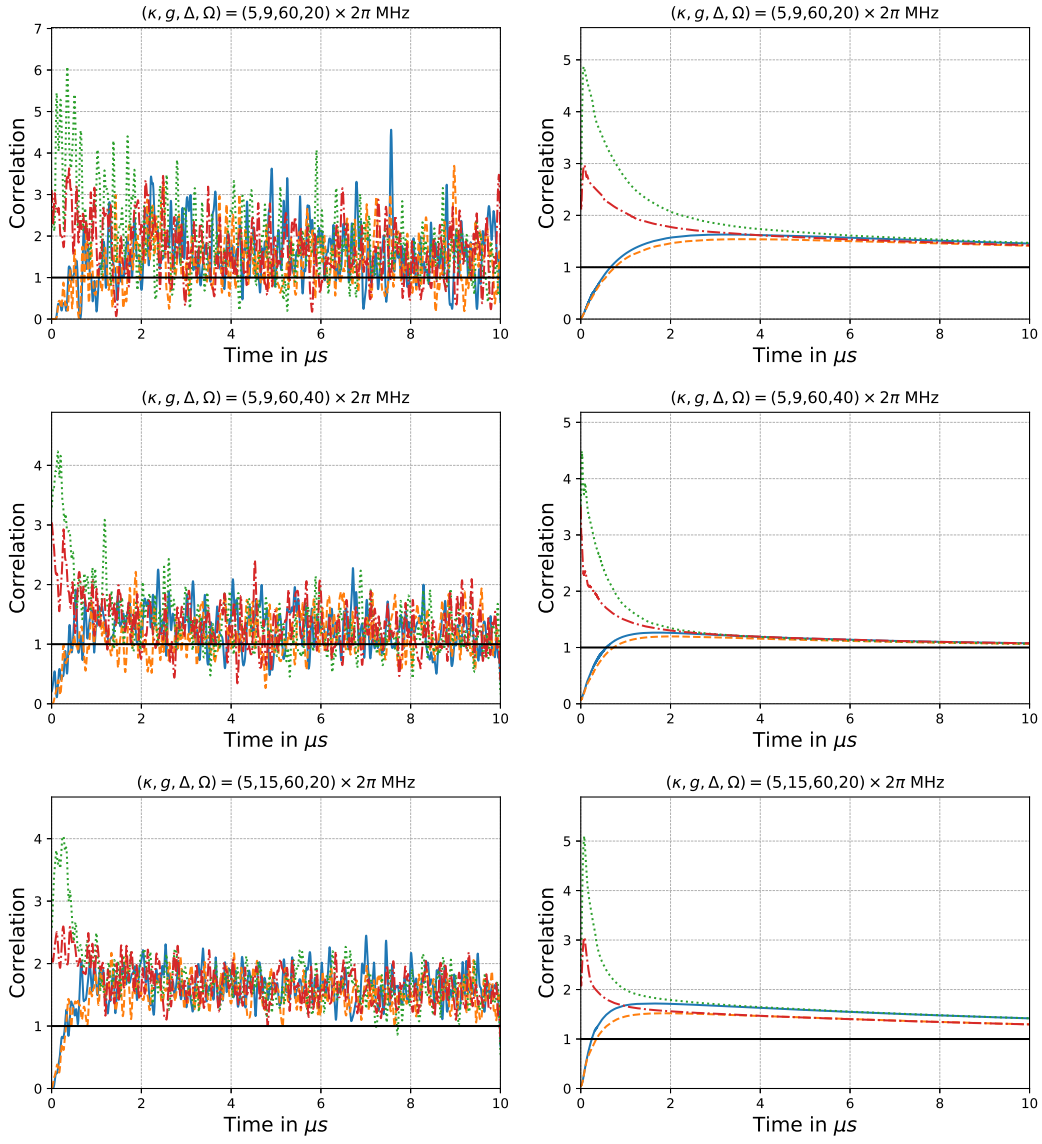

Figure 9.10: Intensity correlation functions $g^{(2)}_{aa}(\tau)$ (blue solid), $g^{(2)}_{bb}(\tau)$ (orange dashed), $g^{(2)}_{ab}(\tau)$ (green dotted) and $g^{(2)}_{ba}(\tau)$ (red dash-dotted) obtained from photon counting simulations and from solving the master equation.

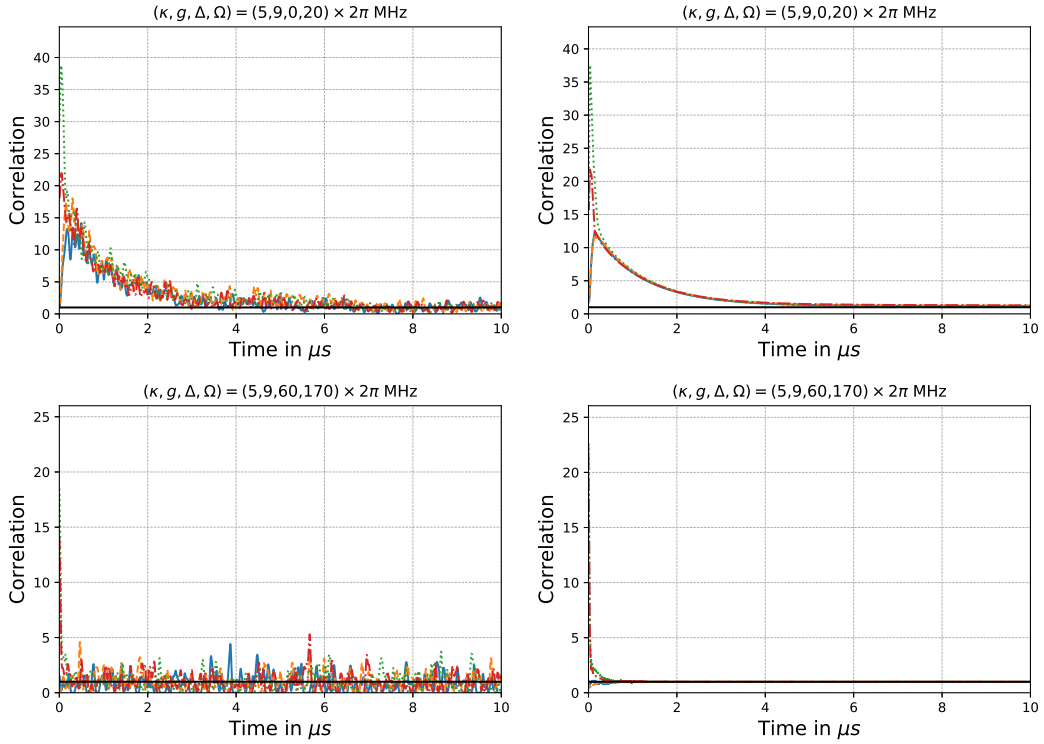

Figure 9.11: Intensity correlation functions $g^{(2)}_{aa}(\tau)$ (blue solid), $g^{(2)}_{bb}(\tau)$ (orange dashed), $g^{(2)}_{ab}(\tau)$ (green dotted) and $g^{(2)}_{ba}(\tau)$ (red dash-dotted) obtained from photon counting simulations and from solving the master equation.

9.4.3 Violation of Cauchy-Schwarz Inequalities

We take now a closer look at the quantum signatures that are a little more difficult to spot than sub-Poissonian photon statistics and antibunching, i.e., the violation of the other classical Cauchy-Schwarz inequalities that we introduced back in Sec. 4.6. The trajectories are supposed to average to the same result as the master equation. Therefore, we use the zero-delay results from the master equation solution (horizontal lines) for comparison in the plots of this Subsection, because the result from the trajectory simulation have not converged enough.

In Fig. 9.12 we take a look at the condition $|g^{(2)}(\tau)-1| < |g^{(2)}(0)-1|$ for the autocorrelation functions. In the main parameter regime of interest (high detuning and low driving), when there is antibunching this is never really

violated (see first row of Fig. 9.12). In the results from quantum trajectories there are occasional violations, but this is not backed up by the master equation solution and can be attributed to the noisiness of the trajectories. Even outside this regime, the zero-delay autocorrelation function $g^{(2)}(0)$ stays quite close to 1 or at least grows very slowly for high driving and/or low detuning, but $g^{(2)}(\tau)$ can reach quite large values for small time delays, which leads to a substantial violation of that particular Cauchy-Schwarz relation (see second row Fig. 9.12 for a low detuning example).

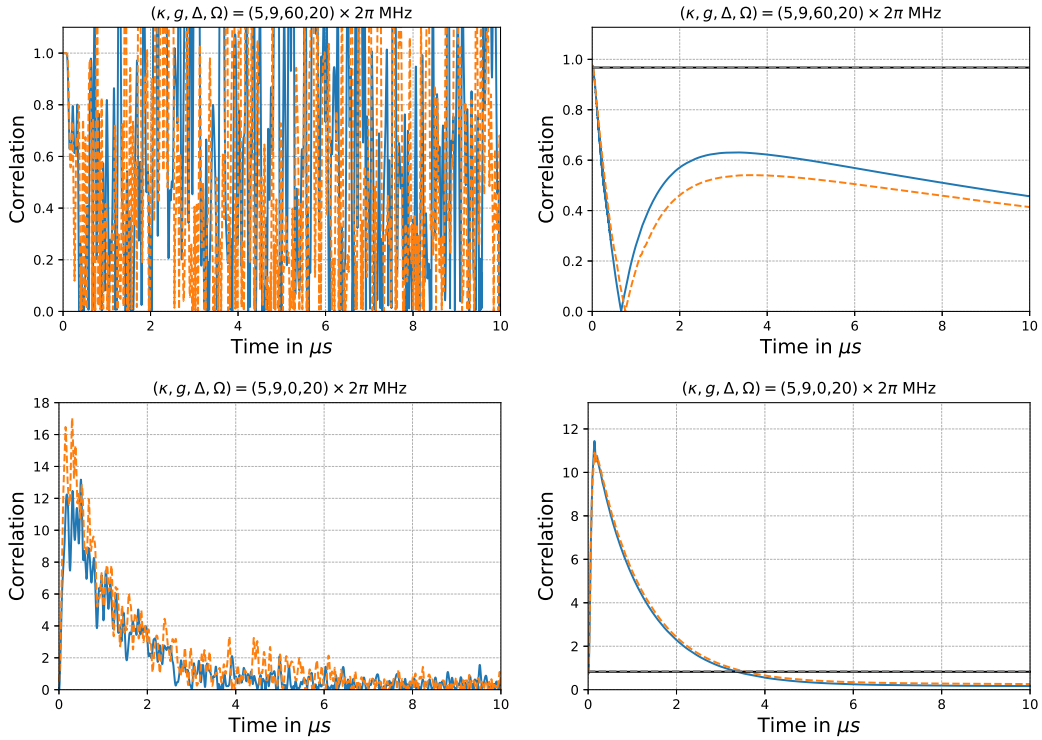

Figure 9.12: $|g^{(2)}_{aa}(\tau)-1|$ (solid blue) and $|g^{(2)}_{bb}(\tau)-1|$ (dashed orange) computed from 500 quantum trajectories (left) and from the steady state solution of the master equation (right). The horizontal lines represent $|g^{(2)}_{aa}(0)-1|$ (black solid) and $|g^{(2)}_{bb}(0)-1|$ (grey dashed).

Owing to the existence of the second cavity mode and the concomitant existence of a crosscorrelation in this scheme, we now can observe an additional quantum signature of the light based on it.

The strongest of all these quantum signatures is the violation of $[g^{(2)}_{ab}(\tau)]^2 \leq g^{(2)}_{aa}(0)g^{(2)}_{bb}(0)$, which usually occurs by a margin of several orders of magnitude,

as can be seen in Fig. 9.13. Sub-Poissonian statistics clearly also contribute to breaking this inequality, but even if those were not present, e.g., in the regime of strong driving, the excess fluctuations of the crosscorrelation would make sure that the inequality still no longer holds (see second row of Fig. 9.13). If the autocorrelations are sufficiently sub-Poissonian $|g^{(2)}_{aa}(0)g^{(2)}_{bb}(0)| < 1$ the inequality is violated at all times, else the violation just persists for small time delays. Since we already observed that $g^{(2)}(\tau) \leq g^{(2)}(0)$ for both autocorrelation functions, we can check whether $[g^{(2)}_{ab}(\tau)]^2 \leq g^{(2)}_{aa}(\tau)g^{(2)}_{bb}(\tau)$ holds, which is a more restrictive condition fields that already obey $g^{(2)} < 1$, so potentially a way to quantify the degree of violation. This inequality, however, is only violated for small time delays.

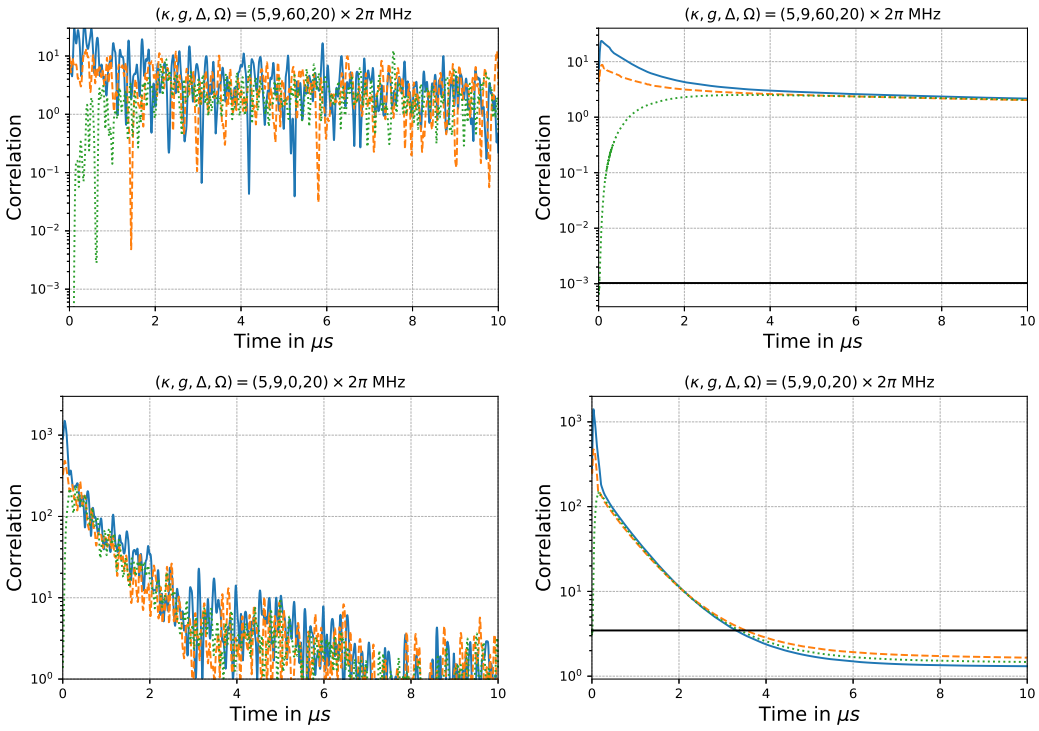

Figure 9.13: $[g^{(2)}_{ab}(\tau)]^2$ (solid blue), $[g^{(2)}_{ba}(\tau)]^2$ (dashed orange) and $g^{(2)}_{aa}(\tau)g^{(2)}_{bb}(\tau)$ (green dotted)) computed from 500 quantum trajectories (left) and from the steady state solution of the master equation (right). The horizontal line represents $g^{(2)}_{aa}(0)g^{(2)}_{bb}(0)$.

Finally, we have the condition $|g^{(2)}_{ab}(\tau)-1|^2 \leq (g^{(2)}_{aa}(0)-1)(g^{(2)}_{bb}(0)-1)$ for crosscorrelation functions in Fig. 9.14. This appears to be mainly violated for

small time delays and only occasionally for larger ones. Again, larger driving strengths and lower detunings remove the violation.

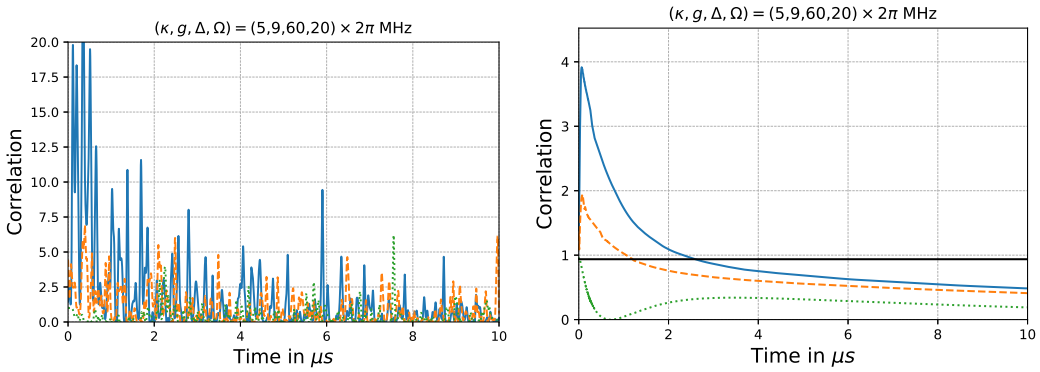

Figure 9.14: $|g^{(2)}_{ab}(\tau)-1|^2$ (solid blue), $|g^{(2)}_{ba}(\tau)-1|^2$ (dashed orange) and $(g^{(2)}_{aa}(\tau)-1)(g^{(2)}_{bb}(\tau)-1)$ (dotted green) computed from 500 quantum trajectories (left) and from the steady state solution of the master equation (right). The horizontal line represents $(g^{(2)}_{aa}(0)-1)(g^{(2)}_{bb}(0)-1)$.

It should also be noted that while we lose quantum signatures such as sub-Poissonian photon statistics in the limit of high driving, the other ones still appear and for those related to $|g^{(2)}(\tau)-1|$ are even amplified.

9.5 4-state Model

The full model as it is, is fine to do quantum trajectories, but solving the master equation is quite resource- and time-consuming, especially if we were to perform quantum regression or to do parameter sweeps. Therefore, in this section, we would like to see whether we can come up with a simpler model that can reproduce some of the results that we have so far.

9.5.1 Version I

In the initial theoretical studies of the one-atom laser experiment [129] the full model was reduced to an effective 4-state model. We may do the same by, first, ignoring the far off-resonant excited states $F' = 2$ and $F' = 5$ and, second, remove the Zeeman sublevelstructure of the $F' = 3$ and $F' = 4$ states. Here

the effective coupling strengths are obtained by taking the squared average of the dipole transition elements:

$$\begin{aligned} g_{F,F'} &= g\sqrt{\frac{1}{2\min(F,F')+1}\sum_{m_F=-F}^{F}|\langle F,m_F|\mu_0|F',m_F\rangle|^2} \\ \Omega_{F,F'} &= \frac{\Omega}{2}\sqrt{2\frac{1}{F+F'}\sum_{m_F=-F}^{F}|\langle F,m_F|\mu_{\pm1}|F',m_F\pm1\rangle|^2} \\ \gamma_{F,F'} &= \gamma\sqrt{\frac{\sum_{m_F=-F}^{F}|\langle F,m_F|\mu_0|F',m_F\rangle|^2}{\sum_F\sum_{m_F=-F}^{F}|\langle F,m_F|\mu_0|F',m_F\rangle|^2}} \end{aligned} \tag{9.13}$$

which yields

$$\begin{aligned} \{g_{33'},g_{34'},g_{43'},g_{44'}\} &= \{\frac{1}{2\sqrt{2}},\frac{\sqrt{5}}{2\sqrt{14}},\frac{1}{2\sqrt{6}},\frac{\sqrt{7}}{6\sqrt{2}}\}g \\ \{\Omega_{33'},\Omega_{34'},\Omega_{43'},\Omega_{44'}\} &= \{\frac{\sqrt{7}}{4\sqrt{6}},\frac{\sqrt{5}}{4\sqrt{7}},\frac{1}{4\sqrt{3}},\frac{\sqrt{7}}{8\sqrt{2}}\}\Omega \\ \{\gamma_{33'},\gamma_{43'},\gamma_{34'},\gamma_{44'}\} &= \{\frac{3}{4},\frac{1}{4},\frac{5}{12},\frac{7}{12}\}\gamma. \end{aligned} \tag{9.14}$$

In reality, the atom never really is in an equal superposition of all the hyperfine states, but in between jumps it trends towards quasi-steady-states, which are roughly equal superpositions (if the driving strengths are equal) of all the odd or all the even Zeeman sublevels, so that on average this should be a sensible approximation. Indeed, the master equation solution shows an equal population of the Zeeman sublevels apart from the edge states, which tend to be more populated, but not by a large margin. Incidentally, in resonance the Zeeman sublevels of $F = 4$ with odd m_F and those of $F = 3$ with even m_F are one to two orders of magnitude less populated than their neighbours. The

effective 4-state Hamiltonian reads

$$\begin{aligned}\hat{\mathcal{H}} &= \delta|3\rangle\langle 3|+\Delta|3'\rangle\langle 3'|+(\Delta+\omega_{3'4'})|4'\rangle\langle 4'| \\ &+e^{-i\delta t}(\Omega_{33'}|3\rangle\langle 3'|+\Omega_{34'}|3\rangle\langle 4'|)+H.c. \\ &+e^{i\delta t}(\Omega_{43'}|4\rangle\langle 3'|+\Omega_{44'}|4\rangle\langle 4'|)+H.c. \\ &+\hat{a}^\dagger(g_{43'}|4\rangle\langle 3'|+g_{44'}|4\rangle\langle 4'|)+H.c. \\ &+\hat{b}^\dagger(g_{33'}|3\rangle\langle 3'|+g_{34'}|3\rangle\langle 4'|)+H.c..\end{aligned} \tag{9.15}$$

The master equation changes to

$$\begin{aligned}\dot{\hat{\rho}} &= -i\Big[\hat{\mathcal{H}},\hat{\rho}\Big]+\kappa\mathcal{D}[\hat{a}]\hat{\rho}+\kappa\mathcal{D}[\hat{b}]\hat{\rho} \\ &+\frac{\gamma_{33'}}{2}\mathcal{D}[|3\rangle\langle 3'|]\hat{\rho}+\frac{\gamma_{43'}}{2}\mathcal{D}[|4\rangle\langle 3'|]\hat{\rho} \\ &+\frac{\gamma_{44'}}{2}\mathcal{D}[|4\rangle\langle 4'|]\hat{\rho}+\frac{\gamma_{34'}}{2}\mathcal{D}[|3\rangle\langle 4'|]\hat{\rho}.\end{aligned} \tag{9.16}$$

9.5.2 Version II

In the Hamiltonian dynamics in Eq. (9.15) half of the transitions are processes detuned by Δ and the other half is detuned by $\Delta+\omega_{3'4'}$, such as the transition going with $g_{33'}$, $g_{44'}$, $\Omega_{43'}$ and $\Omega_{34'}$, which we shall ignore in the following. This allows us to get rid of any explicit time dependence after rotating about $\hat{U} = e^{-i\delta(|3\rangle\langle 3|-|4'\rangle\langle 4'|)t}$:

$$\begin{aligned}\hat{\mathcal{H}} &= \Delta|3'\rangle\langle 3'|-\Delta|4'\rangle\langle 4'| \\ &+\Omega_{33'}|3\rangle\langle 3'|+H.c. \\ &+\Omega_{44'}|4\rangle\langle 4'|+H.c. \\ &+\hat{a}^\dagger g_{43'}|4\rangle\langle 3'|+H.c. \\ &+\hat{b}^\dagger g_{34'}|3\rangle\langle 4'|+H.c..\end{aligned} \tag{9.17}$$

Now that the more off-resonant processes have been eliminated, it is clear to see that in these Hamiltonian dynamics, photons are put into the modes in an

alternating fashion and never in succession into the same mode.

9.5.3 Comparison of the Models

Let us start by comparing the atomic populations and cavity mode populations for a single trajectory and the Master equation solutions. We restrict ourselves here to a high detuning and low driving, as beyond that the simpler models should not hold anymore. On first sight, the 4-state models appear much more regular, whereas the trajectory of the full model may stay in the same state for prolonged periods in which fewer photons are observed, as can be seen in Figs. 9.15-9.16. This seems to coincide with the time before the steady state is reached, which is longer than in the 4-state models, which makes sense since there is much less going on in these. The overall lower cavity populations can be explained by the fact that in the full model the atom is also being pumped into dark states, which slows down the process of putting photons into the cavities, as was argued in [129]. In the 4-state models, these dark states do not occur.

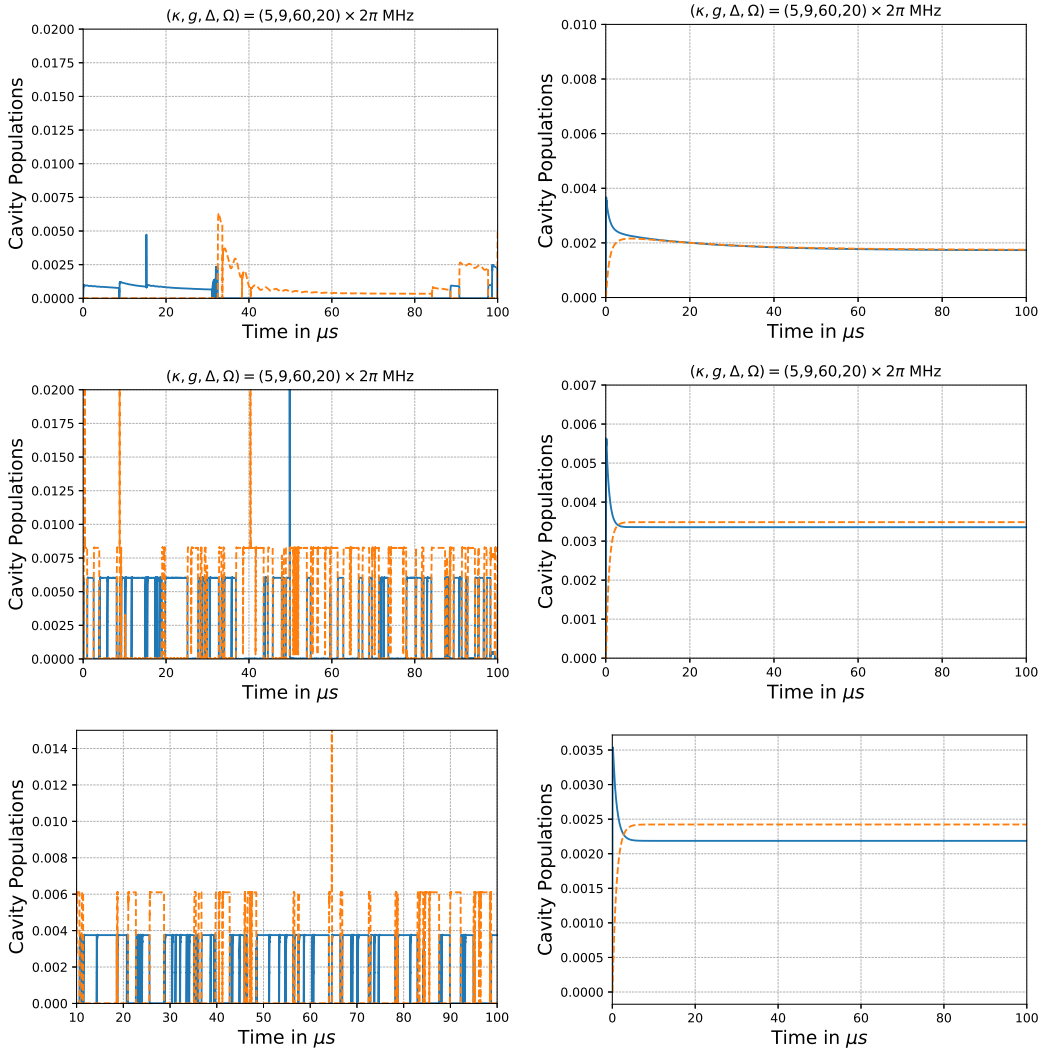

Figure 9.15: Cavity mode populations from a single trajectory (left column) and the ensemble average from the master equation (right column) for the full model (top row), the 4-state model (middle row) and the simplified 4-state model (bottom row). The parameters were set to $\{g, \kappa, \Omega, \Delta\} = \{9, 5, 20, 60\}$ in units of $2\pi\times$MHz.

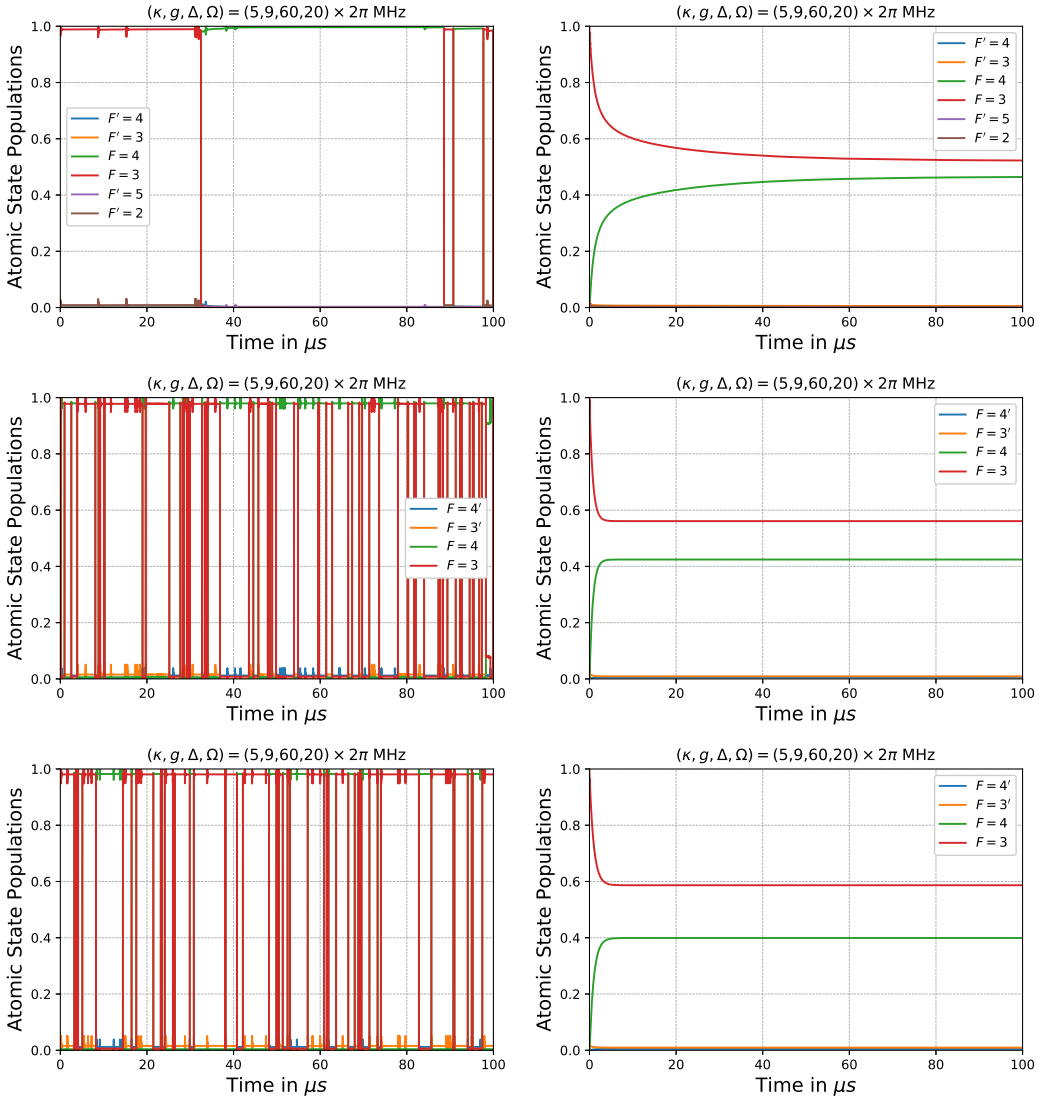

Figure 9.16: Atomic state populations from a single trajectory (left column) and the ensemble average from the master equation (right column) for the full model (top row), the 4-state model (middle row) and the simplified 4-state model (bottom row). The parameters were set to $\{g, \kappa, \Omega, \Delta\} = \{9, 5, 20, 60\}$ in units of $2\pi\times$MHz.

Even though our three models can reach results that can quantitatively differ quite a bit, as we just saw, when it comes to the photon statistics from the effective model displayed in Fig. 9.17, they are in qualitative agreement with Fig. 9.10. This of course speaks for the approximations made, when it comes to isolating the main dynamics of the system. The magnitudes of the

intensity correlation functions are quite a bit lower and the time scales slower than those in Fig. 9.10, also there are no excess fluctuations in Fig. 9.17. The origin of this discrepancy, should again be connected to the dark states, which the 4-state models do not have. Their slowing effect on the dynamics should cause slower time scales, which in turn leads to fewer photons in the cavity modes and thus decreased crosscorrelation functions.

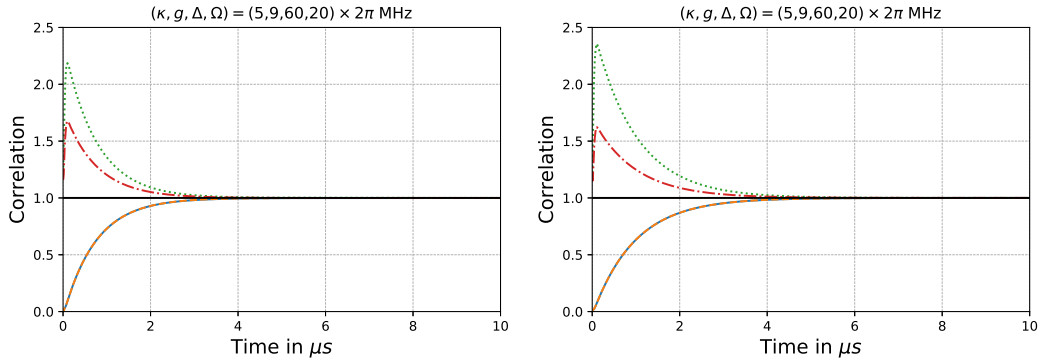

Figure 9.17: Intensity correlation functions $g^{(2)}_{aa}(\tau)$ (blue solid), $g^{(2)}_{bb}(\tau)$ (orange dashed), $g^{(2)}_{ab}(\tau)$ (green dotted) and $g^{(2)}_{ba}(\tau)$ (red dash-dotted) for Version I (left) and II (right) of the 4-state model. The parameters were set to $\{g, \kappa, \Omega, \Delta\} = \{9, 5, 20, 60\}$ in units of $2\pi\times$MHz.

9.5.4 Ramp of the Laser Intensity

Using the 4-state model, with off-resonant processes eliminated in Eq. (9.15), we ramp up both Rabi frequencies and look at the change in intracavity photon number (directly proportional to the output photon flux) in Fig. 9.18. Similar to the original one-atom laser, we observe an immediate onset in the photon number in Fig. 9.18. A further increase in the driving strength leads to a drop-off in the intracavity photon number; it has been argued that this is due to the laser-induced Autler-Townes splitting pushing the transitions further away from resonance [126]. The more exact condition describing the lasing threshold is the ratio of the photon flux from cavity decay and fluorescence,

$$\mathcal{T}_a = \frac{2\kappa\langle\hat{a}^\dagger\hat{a}\rangle}{\gamma_{43'}\langle\hat{\rho}_{3'3'}\rangle}, \tag{9.18}$$

and

$$\mathcal{T}_b = \frac{2\kappa\langle\hat{b}^\dagger\hat{b}\rangle}{\gamma_{34'}\langle\hat{\rho}_{4'4'}\rangle}. \tag{9.19}$$

Lasing is deemed to occur if $\mathcal{T} > 1$. As can be seen in Fig. 9.19 both ratios are larger than one from the outset, so there is no lasing threshold. The ratio decreases as the laser strength increases because the excited state populations and the associated effective spontaneous emission rates grow faster than the cavity photon numbers. A lower detuning leads to an increased output photon flux, but also causes the ratios to decay faster, as this also increases excited state populations. Note that this is different from the full model, where getting closer to resonance makes dark states start to play a more significant role.

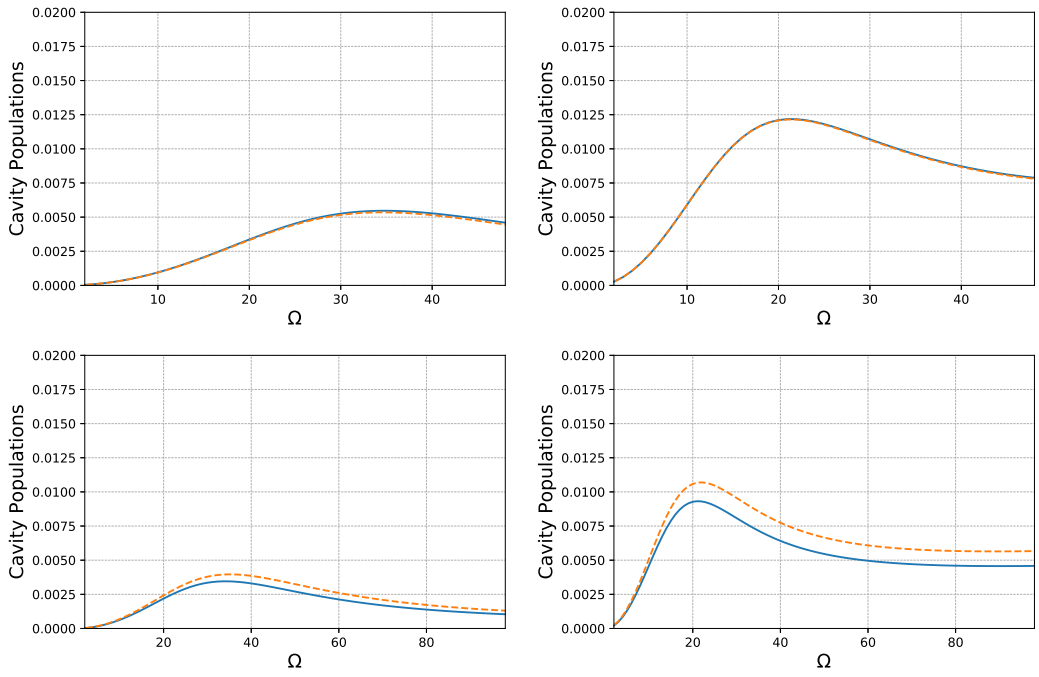

Figure 9.18: Intracavity photon numbers $\langle\hat{a}^\dagger\hat{a}\rangle$ (solid blue) and $\langle\hat{b}^\dagger\hat{b}\rangle$ (dashed orange) as a function of driving strength Ω in units of $2\pi\times$MHz. $\{g, \kappa, \gamma, \Delta\} = \{9, 5, 5.2227, 60\}$ in units of $2\pi\times$MHz on the left and $\{g, \kappa, \gamma, \Delta\} = \{9, 5, 5.2227, 20\}$ on the right. The top row shows version I and the bottom row version II of the 4-state model.

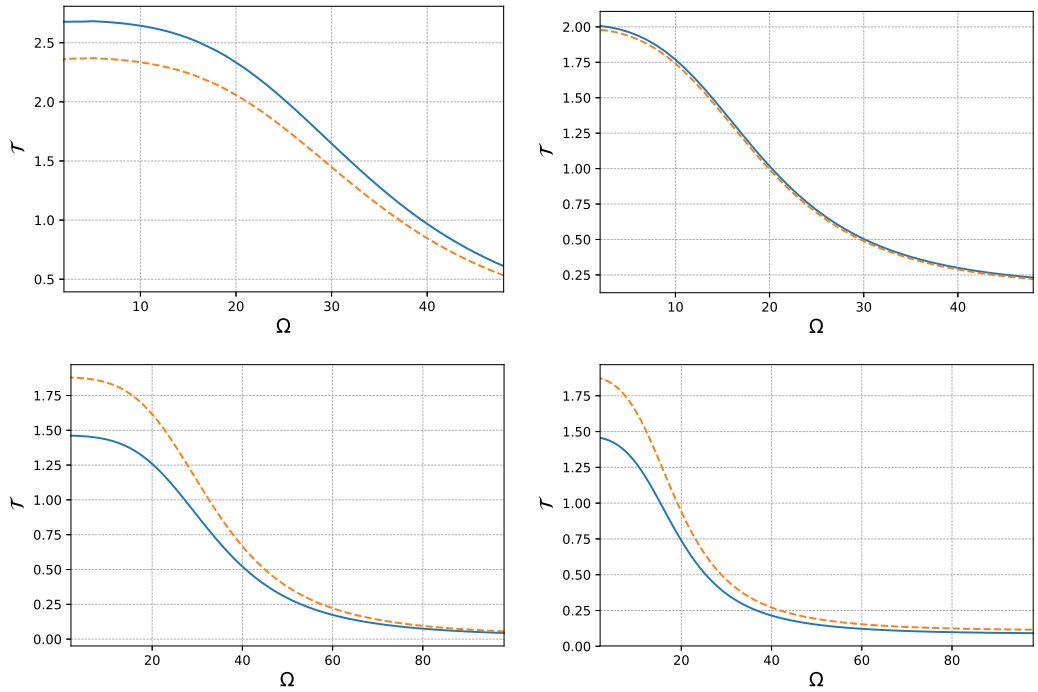

Figure 9.19: $\mathcal{T}_a$ (solid blue) and $\mathcal{T}_b$ (dashed orange) as a function of driving strength Ω in units of $2\pi\times$MHz. $\{g, \kappa, \gamma, \Delta\} = \{9, 5, 5.2227, 60\}$ in units of $2\pi\times$MHz on the left and $\{g, \kappa, \gamma, \Delta\} = \{9, 5, 5.2227, 20\}$ on the right. The top row shows version I and the bottom row version II of the 4-state model.

As we ramp up the driving strength, we also track the zero-delay intensity correlation function. In Fig. 9.20 we can observe that the sub-Poissonian statistics of the autocorrelation functions vanish and that the super-Poissonian statistics of the crosscorrelation functions become more pronounced as the laser strength increases. Both effects can be explained by increasing the coupling, making it more likely to observe two photons close in time. Closer to resonance, we actually also observe sub-Poissonian statistics of the crosscorrelation for weak fields. A possible explanation for this feature is that after a photon has been put in a cavity mode by an atomic deexcitation, if the field is too weak to make the atom progress sufficiently fast through to the excited state ($\Omega_{33'} < g_{34'}$ or $\Omega_{44'} < g_{43'}$), the atom is more likely to undergo vacuum Rabi oscillations. This would delay the emission of the next photon and thus lead to a decreased crosscorrelation.

As we have already seen, the 4-state models do not catch all the intricacies

of the full model and thus this can also only give us a general idea for how the correlation functions behave for different field strengths. Some features shown in Fig. 9.20, such as the excess fluctuations in the autocorrelation functions in the high-field limit for a finite detuning, we have seen in the full model, albeit at different values. A drastic decrease of the bunching of the crosscorrelation for decreasing laser intensities can also be seen; whether it goes all the way down to 1 or even below as the curves with lower detuning suggest, is unclear due to the dynamics becoming extremely slow and thus it taking longer and longer to reach the steady state.

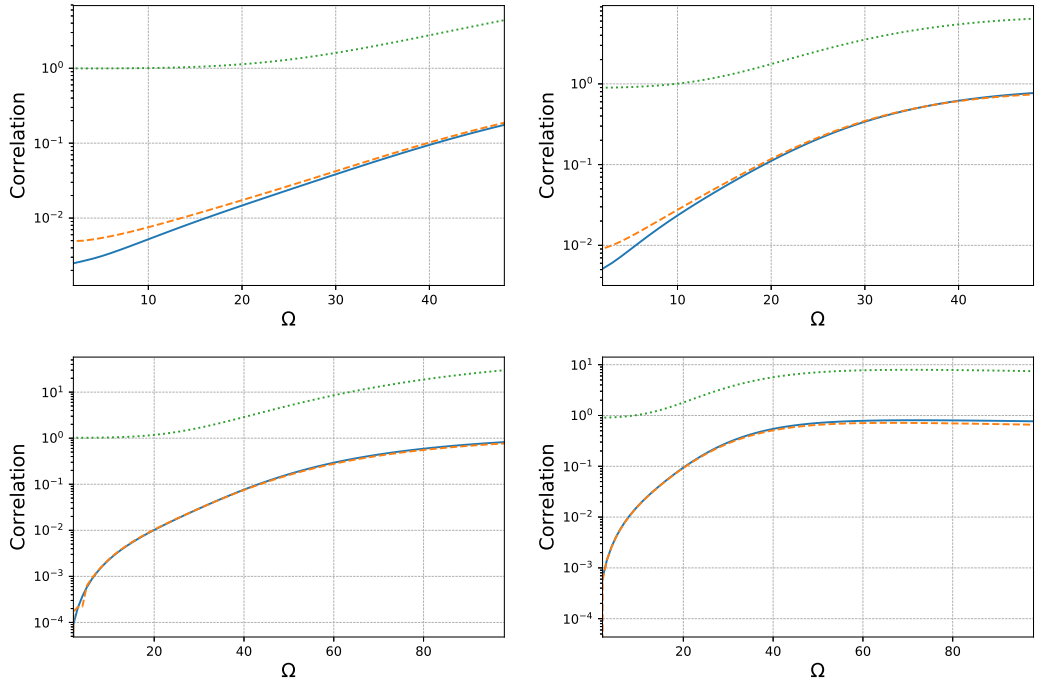

Figure 9.20: Correlation functions $g^{(2)}_{aa}(0)$ (blue solid), $g^{(2)}_{bb}(0)$ (orange dashed) and $g^{(2)}_{ab}(0)$ (green dotted) as a function of the driving strength Ω in units of $2\pi\times$MHz. $\{g, \kappa, \gamma, \Delta\} = \{9, 5, 5.2227, 60\}$ in units of $2\pi\times$MHz on the left and $\{g, \kappa, \gamma, \Delta\} = \{9, 5, 5.2227, 20\}$ on the right. The top row shows version I and the bottom row version II of the 4-state model.

9.6 Conclusions and Outlook

To recapitulate, we have performed a preliminary investigation of a novel one-atom laser system, in which the atom couples strongly to two cavity modes.

We have given an overview of the dynamics and observed a variety of different quantum signatures in the output light. An experimental realisation in nanofibre cavity QED is likely to be achieved soon, at which point some of the theoretical predictions might be verified, either qualitatively or quantitatively.

Part IV

Cavity-mediated Many-body Quantum Dynamics with Spin-F Atoms

Chapter 10

Generation of Spin Cat States in an engineered Dicke model

10.1 Introduction

A so-called "cat state" is a quantum superposition of two quasi-classical states, in analogy to Schrödinger's original Gedankenexperiment [130]. As well as this fundamental physics aspect, such states are especially interesting for the field of quantum metrology as they allow for quantum-enhanced measurements [38]. Hence, there is considerable interest in the generation of such states, particularly in the context of light fields and of spin angular momentum in atomic ensembles [107, 131–137]. Cat states of light involving quasi-classical states of large average photon number are notoriously difficult to produce because of their extreme sensitivity to even very small losses in propagation and in optical elements. Spin angular momentum states of atoms, however, offer better possibilities for mesoscopic or macroscopic cat states due to the generally long lifetimes (and coherence times) of the involved spin states, which are typically stable ground hyperfine states.

Nevertheless, the preparation of large-sized spin cat states is still very challenging, as decoherence still scales with the size of the system (i.e., the magnitude of the total spin), and evolution that produces a cat state in general requires a collective (all-to-all) interaction amongst the atoms. Such dynamics is

offered by small, tightly-confined ("single-mode") spinor atomic Bose-Einstein condensates, but the time scales involved are slow as a result of the relatively weak atom-atom interaction strength, and particle losses are difficult to avoid.

An alternative, and increasingly prevalent means of implementing collective atom-atom interactions is via the platform of cavity quantum electrodynamics (cavity QED), whereby a cavity light field facilitates the exchange of excitation between atoms, i.e., atom-atom interactions are mediated by the cavity field, and are effectively infinite range in nature. Prominent amongst examples of such cavity-mediated collective atomic interactions is the Dicke model [138, 139].

Here, we explore two alternative ways of preparing cat states of two maximal spin projections using recently implemented effective Dicke models: first for trapped ions [140, 141] and then for atom ensembles with cavity-mediated Raman transitions [65, 71].

The chapter is organised as follows: we start in Section 10.2 by introducing a somewhat general, open Dicke model for N particles. By considering a dispersive limit of this model, we show how one can obtain a particular, effective dynamics – the so-called one-axis twisting Hamiltonian – that is known to generate cat states. With damping, the one-axis twisting dynamics is modified and we derive the non-Hermitian time evolution of the spin wave function by changing to a convenient (rotated) basis. We also introduce the fidelity and quantum Fisher information as measures to quantify the success of our scheme in preparing cat states. Then, in Sections 10.3 and 10.4 we take a closer look at the two physical systems – trapped ions and atoms in a cavity – in which our scheme could potentially be put into practice. For each of these systems, we examine the influence of the most relevant decoherence mechanisms on cat-state generation using our scheme. We then consider the requirements that these decoherence mechanisms put on potential experimental values of the key parameters, enabling us to gauge the feasibility of our scheme.

In Section 10.4 we additionally explore quantum jump trajectories, heralded by photon emissions from the cavity, which generate "kitten" states (cat states of smaller spin amplitude) in a random fashion. We close with our conclusions in Section 10.5.

10.2 One-Axis Twisting Dynamics

10.2.1 Engineering from a Dicke model

We consider an ensemble of N identical spinor particles (of total spin $S = Ns$, where s is the spin of each particle) coupled to a, for now unspecified, bosonic mode, which is in equilibrium with a thermal reservoir of mean excitation number $\bar{\mathfrak{n}}$, and subject to decay at a rate κ. The master equation for the system density operator $\hat{\rho}$ is ($\hbar = 1$)

$$\dot{\hat{\rho}} = -i\Big[\hat{H}, \hat{\rho}\Big] + \kappa(\bar{\mathfrak{n}}+1)\mathcal{D}[\hat{a}]\hat{\rho} + \kappa\bar{\mathfrak{n}}\mathcal{D}[\hat{a}^\dagger]\hat{\rho}, \tag{10.1}$$

where $\hat{a}$ represents the bosonic mode annihilation operator, and the Lindblad superoperator is given by

$$\mathcal{D}[\hat{O}]\hat{\rho} = 2\hat{O}\hat{\rho}\hat{O}^\dagger - \hat{\rho}\hat{O}^\dagger\hat{O} - \hat{O}^\dagger\hat{O}\hat{\rho}. \tag{10.2}$$

For the Hamiltonian, we assume a generalised form of the Dicke model,

$$\hat{H} = \omega\hat{a}^\dagger\hat{a} + \omega_0\hat{J}_z + \frac{\lambda_-}{\sqrt{2S}}\Big(\hat{a}\hat{J}_+ + \hat{a}^\dagger\hat{J}_-\Big) + \frac{\lambda_+}{\sqrt{2S}}\Big(\hat{a}\hat{J}_- + \hat{a}^\dagger\hat{J}_+\Big). \tag{10.3}$$

This is expressed in terms of the collective spin operators which are sums of the spin operators of the individual spinors $\hat{S}^{(n)}_{\{x,y,z,\pm\}}$

$$\hat{J}_{\{x,y,z,\pm\}} = \sum_n^N \hat{S}^{(n)}_{\{x,y,z,\pm\}}. \tag{10.4}$$

In the dispersive limit ($|\omega| \gg \omega_0, \lambda_\pm$, albeit more generally valid for $\sqrt{\omega^2+\kappa^2} \gg \omega_0, \lambda_\pm$) we can adiabatically eliminate the bosonic mode to obtain a master

equation for the reduced density operator of the collective spin in the form

$$\begin{aligned}\dot{\hat{\rho}} = &-i\Big[\hat{H},\hat{\rho}\Big]+\frac{\kappa(\bar{\mathfrak{n}}+1)}{2S(\omega^2+\kappa^2)}\mathcal{D}[\lambda_-\hat{J}_-+\lambda_+\hat{J}_+]\hat{\rho}\\ &+\frac{\kappa\bar{\mathfrak{n}}}{2S(\omega^2+\kappa^2)}\mathcal{D}[\lambda_-\hat{J}_++\lambda_+\hat{J}_-]\hat{\rho},\end{aligned} \tag{10.5}$$

with the Hamiltonian

$$\begin{aligned}\hat{H} = &\left[\omega_0-\frac{\omega(2\bar{\mathfrak{n}}+1)(\lambda_-^2-\lambda_+^2)}{2S(\omega^2+\kappa^2)}\right]\hat{J}_z\\ &-\frac{\omega}{2S(\omega^2+\kappa^2)}\Big[(\lambda_-+\lambda_+)^2\hat{J}_x^2+(\lambda_--\lambda_+)^2\hat{J}_y^2\Big].\end{aligned} \tag{10.6}$$

Now, for the purposes of this Chapter, the original Dicke model system is itself assumed to have been "engineered" and that the parameters ω, ω_0, and $\lambda_\pm$ are effective parameters that are typically comparable in (energy) scale, but can be tuned as desired. So, in particular, we may choose $\lambda_+ = \lambda_- = \lambda$ and $\omega_0 = 0$ in Eqs. (10.5-10.6) to give

$$\dot{\hat{\rho}} = -i\Big[\hat{H},\hat{\rho}\Big]+\Gamma\mathcal{D}[\hat{J}_x]\hat{\rho}, \tag{10.7}$$

with the one-axis twisting Hamiltonian [142],

$$\hat{H} = -\Lambda\hat{J}_x^2, \tag{10.8}$$

where

$$\Lambda = \frac{2\lambda^2\omega}{S(\omega^2+\kappa^2)} \tag{10.9}$$

and

$$\Gamma = \frac{2\lambda^2\kappa(2\bar{\mathfrak{n}}+1)}{S(\omega^2+\kappa^2)} \overset{\omega\neq 0}{\equiv} \frac{\kappa(2\bar{\mathfrak{n}}+1)}{\omega}\Lambda. \tag{10.10}$$

For the remainder of this Chapter ω and Λ are assumed, without loss of generality, to be positive.

Our choice of parameters ($\lambda_+ = \lambda_- = \lambda$ and $\omega_0 = 0$) leads to the elimination of the two terms proportional to $\hat{S}_z$ and $\hat{S}_y^2$. The former term would introduce dephasing between the superposition components, while the latter would add a separate, distinct one-axis twisting to the dynamics.

10.2.2 Time evolution of the wave function

The one-axis twisting Hamiltonian (10.8) is known to generate spin cat states, that is, coherent superpositions of the angular momentum eigenstates $|S, S\rangle_z$ and $|S, -S\rangle_z$. For finite Γ, we can consider a quantum trajectory treatment of (10.7) and generalise this Hamiltonian evolution to that of the non-Hermitian effective Hamiltonian [43, 44]

$$\hat{\mathcal{H}} = -(\Lambda+i\Gamma)\hat{J}_x^2. \tag{10.11}$$

In the two systems that we will be looking at, it turns out that either $\Gamma \approx 0$ (trapped ions) or that, for finite Γ (cavity QED), the quantum jumps associated with the quantum trajectory picture correspond to photon emissions from a cavity, which could be monitored to facilitate a conditional evolution. We note also the possibility $\Lambda = 0$ and $\Gamma > 0$, e.g., when $\omega = 0$. In this case, the Hamiltonian can lead to novel entangled-state cycles of collective spin states or to probabilistic preparation of the state $|S, 0\rangle_x$ [143].

Since the Hamiltonian (10.11) depends only on $\hat{J}_x$, it will be convenient at times to change from the basis of $\hat{S}_z$ eigenstates to the basis spanned by those

of $\hat{S}_x$ through

$$|S,m'\rangle_z = \sum_{m=-S}^{S} D^S_{m,m'}\Big(-\frac{\pi}{2}\Big)|S,m\rangle_x, \tag{10.12}$$

where the subscript on the ket indicates in which basis the collective spin state is, and $D^S_{m,m'}$ are the elements of the Wigner D matrix [144],

$$\begin{aligned} D^S_{m,m'}(\beta) = &\sum_{k=0}^{S+m}(-1)^{k-m'+m} \\ &\times \frac{\sqrt{(S+m')!(S-m')!(S+m)!(S-m)!}}{k!(S+m'-k)!(S-m-k)!(k+m-m')!} \\ &\times \left(\cos\frac{\beta}{2}\right)^{2S-2k+m'-m}\left(\sin\frac{\beta}{2}\right)^{2k-m'+m}, \end{aligned} \tag{10.13}$$

where the sum runs over all non-negative factorial arguments. From now on we can simplify the notation, as we always consider the case $\beta = -\frac{\pi}{2}$ and all sums over m are from $-S$ to S. In particular (from the representation as a spin coherent state) we have

$$D^S_{m,S}(-\frac{\pi}{2}) = 2^{-S}\sqrt{\binom{2S}{S+m}}. \tag{10.14}$$

We always start with an initial Dicke state with maximal orientation in z-direction,

$$|\psi(0)\rangle = |S,S\rangle_z. \tag{10.15}$$

which can be easily achieved by pumping all the spinors to their highest spin state. During the evolution with (10.11) the norm of the wave function decays

due to the non-Hermiticity; the renormalised wave function at a time t is given by

$$\begin{aligned} |\psi(t)\rangle &= \frac{e^{-i\hat{\mathcal{H}}t}|\psi(0)\rangle}{||e^{-i\hat{\mathcal{H}}t}|\psi(0)\rangle||} \\ &= \frac{\sum_m D^S_{m,S} e^{i\Lambda m^2 t} e^{-\Gamma m^2 t}|S,m\rangle_x}{\sqrt{\sum_m e^{-2\Gamma m^2 t}(D^S_{m,S})^2}}. \end{aligned} \tag{10.16}$$

10.2.3 Fidelity and Quantum Fisher Information

Throughout this chapter, we will use the fidelity, F, and Quantum Fisher Information (QFI) [145] (with respect to the generator $\hat{S}_z$), $\mathcal{F}[\hat{S}_z]$, as figures of merit. The former is a metric for the closeness of the actual quantum state, as described by the density operator $\hat{\rho}$, to the target state $|\Psi\rangle$, and the latter for its quantum metrological usefulness. They are computed in their most general form through

$$\mathrm{F} = \left(\mathrm{Tr}\sqrt{\sqrt{|\Psi\rangle\langle\Psi|}\hat{\rho}\sqrt{|\Psi\rangle\langle\Psi|}}\right)^2 \tag{10.17}$$

and

$$\mathcal{F}[\hat{J}_z] = 2\sum_{k,k'} \frac{(\lambda_k - \lambda_{k'})^2}{\lambda_k + \lambda_{k'}} \left|\langle e_k|\hat{J}_z|e_{k'}\rangle\right|^2, \tag{10.18}$$

where λ_k and $|e_k\rangle$ are the eigenvalues and eigenvectors of $\hat{\rho}$, respectively. In the case of a pure state $\hat{\rho} = |\psi\rangle\langle\psi|$ these simplify to

$$\mathrm{F} = |\langle\Psi|\psi\rangle|^2 \tag{10.19}$$

and

$$\mathcal{F}[\hat{J}_z] = 4\Big(\langle \hat{J}_z^2\rangle - \langle \hat{J}_z\rangle^2\Big). \tag{10.20}$$

10.2.4 No-jump trajectory: Cat State

Free evolution of the initial state subject to the effective Hamiltonian (10.11) up to a time $t = \pi/(2\Lambda)$ gives the state

$$\begin{aligned}
e^{-i\hat{\mathcal{H}}t}|\psi(0)\rangle &= \sum_m D^S_{m,S} e^{i\frac{\pi}{2}m^2} e^{-\frac{\pi\Gamma}{2\Lambda}m^2}|S,m\rangle_x \\
&= \sum_{m\ \text{even}} D^S_{m,S} e^{-\frac{\pi\Gamma}{2\Lambda}m^2}|S,m\rangle_x \\
&+ i\sum_{m\ \text{odd}} D^S_{m,S} e^{-\frac{\pi\Gamma}{2\Lambda}m^2}|S,m\rangle_x \\
&= \sum_{m\ \text{even}} \frac{1}{2}\big(D^S_{m,S} + (-1)^S D^S_{m,-S}\big) e^{-\frac{\pi\Gamma}{2\Lambda}m^2}|S,m\rangle_x \\
&+ i\sum_{m\ \text{odd}} \frac{1}{2}\big(D^S_{m,S} - (-1)^S D^S_{m,-S}\big) e^{-\frac{\pi\Gamma}{2\Lambda}m^2}|S,m\rangle_x \\
&= \sum_{m} \frac{1}{2}\big(D^S_{m,S} + (-1)^S D^S_{m,-S}\big) e^{-\frac{\pi\Gamma}{2\Lambda}m^2}|S,m\rangle_x \\
&+ i\sum_{m} \frac{1}{2}\big(D^S_{m,S} - (-1)^S D^S_{m,-S}\big) e^{-\frac{\pi\Gamma}{2\Lambda}m^2}|S,m\rangle_x \\
&- \sum_{m\ \text{odd}} \frac{1}{2}\underbrace{\big(D^S_{m,S} + (-1)^S D^S_{m,-S}\big)}_{=0} e^{-\frac{\pi\Gamma}{2\Lambda}m^2}|S,m\rangle_x \\
&- i\sum_{m\ \text{even}} \frac{1}{2}\underbrace{\big(D^S_{m,S} - (-1)^S D^S_{m,-S}\big)}_{=0} e^{-\frac{\pi\Gamma}{2\Lambda}m^2}|S,m\rangle_x \\
&= \frac{1+i}{2}\sum_m D^S_{m,S} e^{-\frac{\pi\Gamma}{2\Lambda}m^2}|S,m\rangle_x \\
&\quad + (-1)^S\frac{1-i}{2}\sum_m D^S_{m,-S} e^{-\frac{\pi\Gamma}{2\Lambda}m^2}|S,m\rangle_x
\end{aligned} \tag{10.21}$$

where in multiple places we have used

$$D^S_{m,S} = (-1)^{S-m} D^S_{m,-S}. \tag{10.22}$$

After proper normalisation of the state we have

$$\begin{aligned} |\psi(t=\frac{\pi}{2\Lambda})\rangle = & \frac{\frac{1+i}{2}\sum_m D^S_{m,S} e^{-\frac{\pi\Gamma}{2\Lambda}m^2}|S,m\rangle_x}{\sqrt{\sum_m e^{-\frac{\pi\Gamma}{\Lambda}m^2}(D^S_{m,S})^2}} \\ & + \frac{(-1)^S\frac{1-i}{2}\sum_m D^S_{m,-S} e^{-\frac{\pi\Gamma}{2\Lambda}m^2}|S,m\rangle_x}{\sqrt{\sum_m e^{-\frac{\pi\Gamma}{\Lambda}m^2}(D^S_{m,S})^2}}. \end{aligned} \tag{10.23}$$

In the case of vanishing decay ($\Gamma = 0$) this reduces to

$$\begin{aligned} |\Psi\rangle &= \frac{1+i}{2}\sum_m D^S_{m,S}|S,m\rangle_x + (-1)^S\frac{1-i}{2}\sum_m D^S_{m,-S}|S,m\rangle_x \\ &= \frac{1+i}{2}|S,S\rangle_z + (-1)^S\frac{1-i}{2}|S,-S\rangle_z, \end{aligned} \tag{10.24}$$

i.e., a spin cat state. More generally, the cat state occurs at times $\Lambda t = \frac{\pi}{2}$ mod 2π, while at times $\Lambda t = \frac{3\pi}{2}$ mod 2π one obtains another spin cat state with a different relative phase,

$$|\Psi'\rangle = \frac{1+i}{2}|S,S\rangle_z + (-1)^{S+1}\frac{1-i}{2}|S,-S\rangle_z. \tag{10.25}$$

Note that if the initial state is instead $|S,-S\rangle_z$, then one obtains $|\Psi'\rangle$ at $\Lambda t = \frac{\pi}{2}$ mod 2π.

From the overlap between $|\psi(t)\rangle$ and the target state $|\Psi\rangle$ at time $t =$

$\pi/(2\Lambda)$,

$$\langle\Psi|\psi(t=\frac{\pi}{2\Lambda})\rangle=\frac{\sum_m e^{-\frac{\pi\Gamma}{2\Lambda}m^2}(D^S_{m,S})^2}{\sqrt{\sum_m e^{-\frac{\pi\Gamma}{\Lambda}m^2}(D^S_{m,S})^2}}, \tag{10.26}$$

we obtain the fidelity as

$$\mathrm{F}=\frac{\left[\sum_m e^{-\frac{\pi\Gamma}{2\Lambda}m^2}(D^S_{m,S})^2\right]^2}{\sum_m e^{-\frac{\pi\Gamma}{\Lambda}m^2}(D^S_{m,S})^2}, \tag{10.27}$$

while the QFI is computed to be

$$\begin{aligned}\mathcal{F}[\hat{S}_z]=&\,4\frac{\sum_{m,k,l} D^S_{m,S}D^S_{k,S}D^S_{m,l}D^S_{k,l}e^{-\frac{\pi\Gamma}{\Lambda}(m^2+k^2)}i^{k^2-m^2}l^2}{\sum_m e^{-\frac{\pi\Gamma}{\Lambda}m^2}(D^S_{m,S})^2}\\&-4\left|\frac{\sum_{m,k,l} D^S_{m,S}D^S_{k,S}D^S_{m,l}D^S_{k,l}e^{-\frac{\pi\Gamma}{2\Lambda}(m^2+k^2)}i^{k^2-m^2}l}{\sum_m e^{-\frac{\pi\Gamma}{\Lambda}m^2}(D^S_{m,S})^2}\right|^2.\end{aligned} \tag{10.28}$$

In Fig. 10.1 we show the temporal evolution of the populations of the various states of interest, i.e., the states $|S,S\rangle_z$ and $|S,-S\rangle_z$, and the target state $|\Psi\rangle$, for two values of the total spin S and for $\Gamma=0$ and $\Gamma>0$. It is clear that a higher spin makes the system more fragile to finite dissipation, although more so with regard to the fidelity than to the QFI (we will look at this in more detail in Section IV). Note that the revival of the QFI at $\Lambda t=\frac{3\pi}{2}$ corresponds to generation of the state $|\Psi'\rangle$.

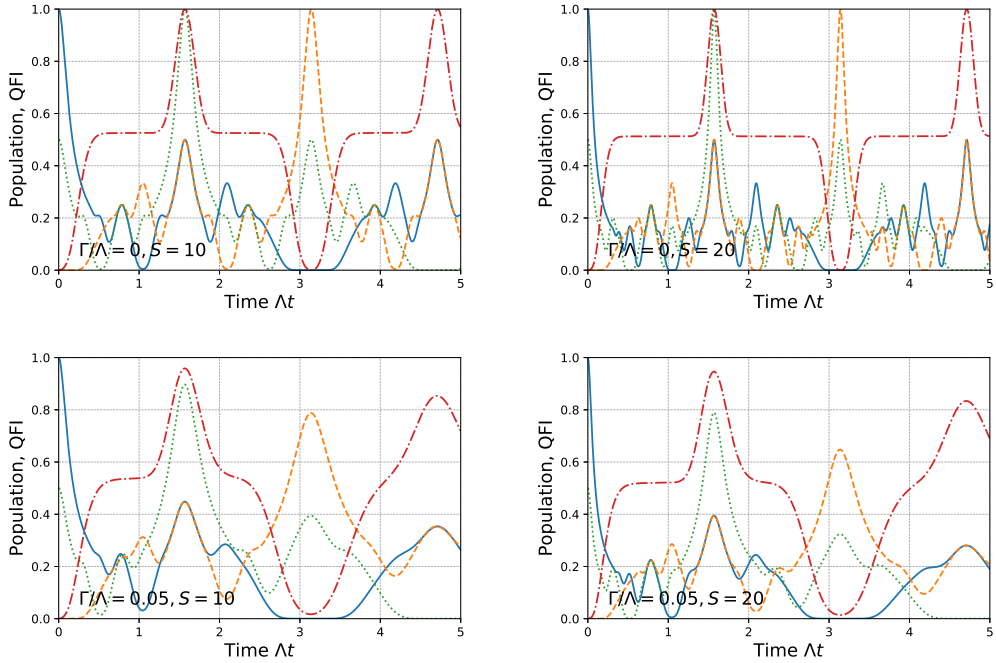

Figure 10.1: Master equation simulations of the QFI (red dash-dotted) and the populations of $|S, S\rangle_z$ (blue solid), $|S, -S\rangle_z$ (orange dashed) and $|\Psi\rangle$ (green dotted) over time for spin $S = 10$ (left column) and $S = 20$ (right column), with $\frac{\Gamma}{\Lambda} = 0$ (top row) and $\frac{\Gamma}{\Lambda} = 0.05$ (bottom row). The QFI is plotted relative to the theoretical maximum, $4S^2$.

10.3 Trapped-Ion Framework

10.3.1 Implementation

For this framework we follow the proposal of [140] in which the spinors are two-level ions, with transition frequency ω_{TS}, confined in a trap of frequency ν, and the harmonic oscillator mode corresponds to the centre-of-mass vibrational mode of the ions. The ions are driven by two lasers (sidebands), one red-detuned and one blue-detuned from the transition frequency, with bare frequencies $\omega_{\pm}$ and Rabi frequencies $\Omega_{\pm}$. In the Lamb-Dicke regime, i.e., $\eta\sqrt{2\bar{\mathfrak{n}}+1} \ll 1$, where η is the Lamb-Dicke parameter and $\bar{\mathfrak{n}}$ is the mean phonon number in the centre-of-mass mode, it can be shown that the system

is described by an effective Dicke model with parameters given by [140]

$$\begin{aligned} \omega &= \nu + \frac{\omega_- - \omega_+}{2}, \\ \omega_0 &= \omega_{\mathrm{TS}} - \frac{\omega_- + \omega_+}{2}, \\ \lambda_\pm &= \frac{\sqrt{2S}\,\Omega_\pm \eta}{2}. \end{aligned} \tag{10.29}$$

For our purposes, we require that $\omega_\pm = \omega_{\mathrm{TS}} \pm \nu + \delta_\pm$ with the offsets to the sidebands, $\delta_\pm$, chosen to satisfy $\delta_+ = -\delta_- = -\delta$, so that $\omega = \delta$ and $\omega_0 = 0$. We also assume that $\Omega_+ = \Omega_- = \Omega$.

10.3.2 Damping and Dephasing

Heating rates in ion traps are typically very small, while advanced cooling schemes (for example, using electromagnetically induced transparency [146]) are expected to enable cooling close to the ground state, corresponding to $\bar{\mathfrak{n}} \approx 0$. Hence, within the trapped-ion framework it is reasonable to assume that $\Gamma \simeq 0$ and to neglect this source of damping.

The dominating decoherence process is usually dephasing originating from voltage fluctuations that propagate to the trap frequency, magnetic field and laser frequency [147]. We use the following Master equation

$$\dot{\hat{\rho}} = -i\Big[\hat{H}, \hat{\rho}\Big] + \frac{\epsilon}{2} \sum_n^N \mathcal{D}[\hat{S}_z^{(n)}]\hat{\rho}, \tag{10.30}$$

where ϵ is the dephasing rate.

The dynamics in (10.30) are invariant under permutation of the identical ions and can therefore be modelled in a Dicke state basis [148, 149]. Hence, we use the Permutational Invariant Quantum Solver (PIQS) [149] to solve the master equation. Fig. 10.2 plots the fidelity and the QFI as a function of the dephasing rate ϵ. Again the overall trend is a decrease in these two quantities, however, in the limit of very strong dephasing the system essentially

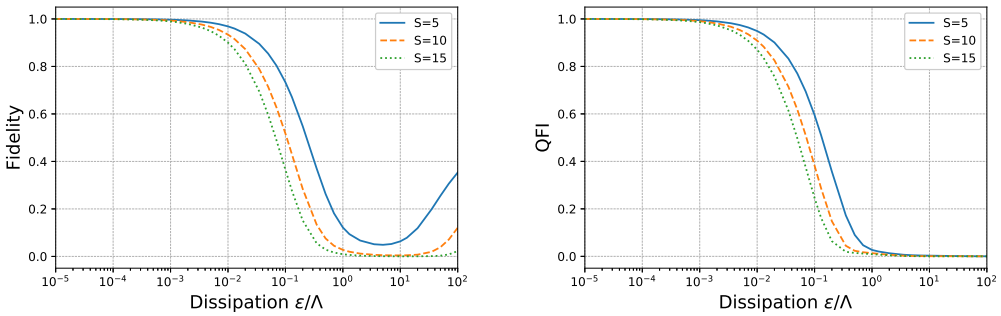

Figure 10.2: Fidelity (left) and QFI (right) as a function of the strength of dissipation $\frac{\epsilon}{\Lambda}$ at the time $\Lambda t = \frac{\pi}{2}$. The QFI is plotted relative to the theoretical maximum, $4S^2$.

gets trapped in the state $|S, S\rangle_z$ and the larger the dephasing the slower the leakage out of that state. This explains why we see the fidelity go up again for increasing dephasing rate ϵ, as the overlap between the cat state and $|S, S\rangle_z$ is large (the fidelity goes to $|\langle\Psi|\psi\rangle|^2 = \frac{1}{2}$ in the limit of infinite ϵ), even though the QFI goes to zero.

10.3.3 Possible Experimental Parameters

For a specific experimental configuration, we can consider trapped $^{40}Ca^+$ ions that are driven on the $S_{1/2} \leftrightarrow D_{5/2}$ quadrupole transition [150]. This transition has a very small natural linewidth, which allows us to ignore spontaneous emission in what follows, especially since the lasers are also detuned from the transition by roughly the trap frequency ($\Delta = \omega_\pm - \omega_{TS} = \pm\nu \mp \delta$).

Let us consider an ensemble of $N = 20$ ions ($S = 10$) in a trap of frequency $\nu/2\pi = 3$ MHz and Lamb-Dicke parameter $\eta = 0.05$. With $\Omega/2\pi = 300$ kHz, we have $\lambda/2\pi = 34$ kHz. The effective coupling strength in the one-axis twisting Hamiltonian is given, for the proposed ion system, by

$$\Lambda = \frac{\Omega^2\eta^2}{\delta}, \tag{10.31}$$

so selecting $\delta/2\pi = 300$ kHz ($\gg \lambda$) yields $\Lambda/2\pi = 750$ Hz. Looking at Fig. 10.2, we see that to achieve a fidelity in excess of 0.9 requires a dephasing rate

$\epsilon/\Lambda \lesssim 0.02$, or $1/\epsilon \gtrsim 11$ ms, which appears within reach of recent experiments with strings of $^{40}Ca^{+}$ ions [151].

10.4 Cavity QED Framework

10.4.1 Implementation

For this framework, we consider an ensemble of atoms trapped inside an optical cavity and undergoing Raman transitions between selected hyperfine-ground-state levels. The Raman transitions are driven by the cavity field and auxiliary laser fields, as depicted in Fig. 10.3. Such schemes have been used in experimental realisations of the Dicke model and implement either effective spin-1/2 [152] or spin-1 [65] atoms. Note that using the scheme of [65] one could also implement larger effective spins per atom by using other hyperfine levels (e.g., spin-2 for $F = 2$ in ^{87}Rb) or atomic species (e.g., spin-3 or spin-4 for ^{133}Cs). Note also that the spin-1/2 implementation is also feasible using the clock states (rather than the stretched states, as depicted in Fig. 10.3) of ^{87}Rb or ^{133}Cs [153]. However, for the spin-1/2 realisation an additional term, proportional to $\hat{S}_z\hat{a}^\dagger\hat{a}$, appears in the effective Hamiltonian (the effect of which, however, becomes small for large enough detunings of the fields), and the tuning of laser frequencies and driving strengths requires somewhat more care.

For the spin-1 realisation in ^{87}Rb the parameters of the effective Dicke model take the specific forms

$$\begin{aligned} \omega &= \omega_c - \frac{\omega_- + \omega_+}{2} + \frac{Ng^2}{3\Delta}, \\ \omega_0 &= \omega_z - \frac{\omega_- - \omega_+}{2} + \frac{\Omega_-^2 - \Omega_+^2}{24\Delta}, \\ \lambda_\pm &= \frac{\sqrt{N} g \Omega_\pm}{12\Delta}, \end{aligned} \tag{10.32}$$

where ω_c and $\omega_\pm$ are the frequencies of the cavity mode and $\sigma_\pm$-polarised laser field, respectively, $\Omega_\pm$ the Rabi frequencies of the laser fields, g the single-

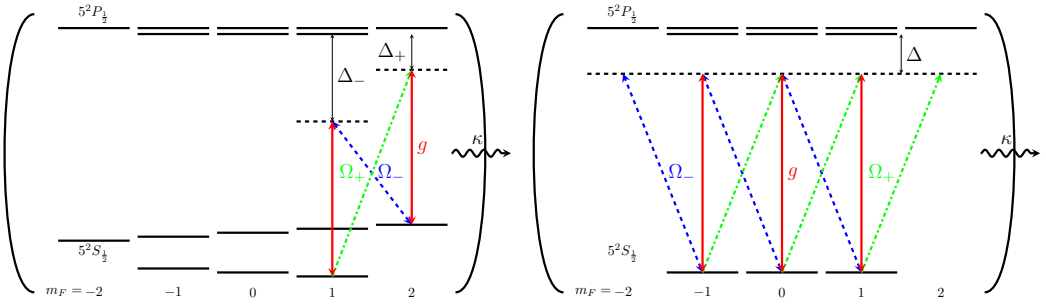

Figure 10.3: Atomic level configurations and excitation schemes for spin-$\frac{1}{2}$ (left) and spin-1 (right) realisations of the Dicke model in optical cavity QED with ^{87}Rb atoms.

atom-cavity coupling strength, ω_z the Zeeman splitting of the $F = 1$ atomic levels, and Δ the detuning of the lasers and cavity mode from the excited state manifold.

One-axis twisting engineered from cavity dynamics but with off-resonant Raman transitions have been studied before in the context of spin squeezing [154–156].

10.4.2 Cavity Decay: No-Jump Evolution

The normalisation factor in Eq. (10.16),

$$||e^{-i\hat{\mathcal{H}}t}|\psi(0)\rangle|| = \sqrt{\sum_m e^{-2\Gamma m^2 t}(D^S_{m,S})^2}, \tag{10.33}$$

gives us the probability $P(t)$ that no jump (no photon emission) has occurred up to a time t through

$$P(t) = ||e^{-i\hat{\mathcal{H}}t}|\psi(0)\rangle||^2 = \sum_m e^{-2\Gamma m^2 t}(D^S_{m,S})^2. \tag{10.34}$$

Since the occurrence of a jump or not leads to two very distinct behaviours, it makes sense to take a closer look at the probability of there being no jump up

until a time $t = \pi/(2\Lambda)$,

$$P(t = \frac{\pi}{2\Lambda}) = \sum_m e^{-\frac{\pi\Gamma}{\Lambda}m^2} (D^S_{m,S})^2, \tag{10.35}$$

for reasons that will become evident in the next section. A certain level of dissipation can be tolerated without considerably increasing the possibility of a jump, but that level clearly decreases with increasing total spin, as shown in Fig. 10.4, where $P(t = \pi/(2\Lambda))$ is plotted as a function of Γ/Λ for varying values of S.

Note that if no jump has occurred after a sufficiently long time (i.e., $2\Gamma t \gg 1$), then the system will be projected into the state $|S, 0\rangle_x$, as this is the only component for which the probability amplitude does not decay. This explains why, in Fig. 10.4, the probability curves level out at constant, finite values for $\Gamma/\Lambda \gtrsim 1$. However, the likelihood of there being no jump decreases gradually with increasing spin length [143].

Focusing still on the case in which no jump occurs, Fig. 10.5 shows the fidelity and QFI of the prepared quantum state as a function of the spin length S and the dissipation rate Γ. Interestingly, the QFI is significantly more robust than the fidelity with respect to increasing spin length. For example, at $\Gamma/\Lambda = 10^{-2}$ the fidelity drops from ~ 1 to ~ 0.8 with an increase of S from 10 to 100, whereas the QFI remains within 1% of the theoretical maximum $4S^2$. The

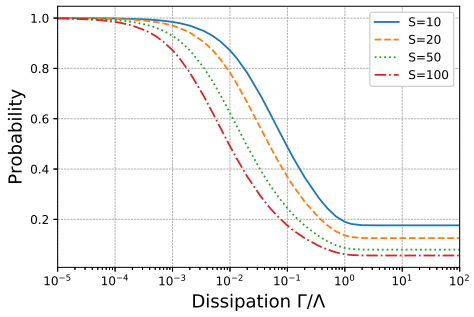

Figure 10.4: Probability of there being no jump until a time $t = \pi/(2\Lambda)$ as a function of the dissipation Γ/Λ for a selection of different spin lengths.

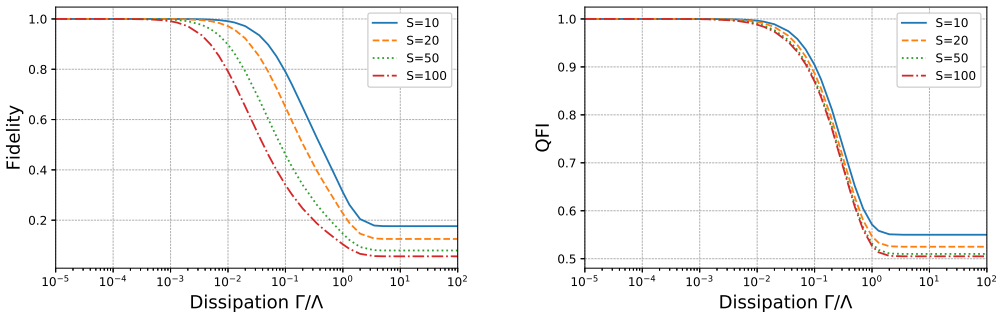

Figure 10.5: Fidelity (left) and QFI (right) as a function of the strength of dissipation Γ/Λ at the time $t = \pi/(2\Lambda)$ given that no jump has occurred. The QFI is plotted relative to the theoretical maximum, $4S^2$.

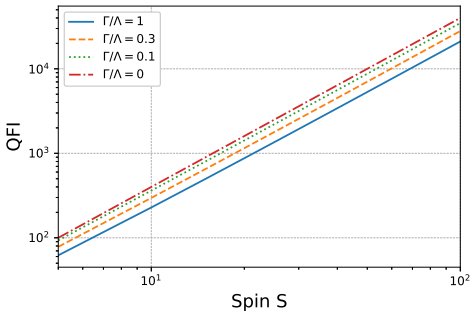

Figure 10.6: QFI of the quantum state at $t = \pi/(2\Lambda)$, given no jump has occurred, as a function of the spin length S for a selection of dissipation strengths Γ/Λ. The line for $\Gamma/\Lambda = 0$ corresponds to the limit $4S^2$, while the line for $\Gamma/\Lambda = 1$ corresponds approximately to the limit $2S^2+2S$.

fidelity and QFI both level out at constant values once $\Gamma/\Lambda \gtrsim 3-5$ and this appears largely independent of the spin length S.

The optimal scaling of the QFI is quadratic: $4S^2$. For increasing Γ/Λ the QFI obviously decreases, and this is further illustrated in Fig. 10.6, where we plot the QFI as a function of spin length S for several values of Γ/Λ. We can in fact compute a lower bound for the QFI scaling in the absence of a jump, since we know that for sufficiently large Γ/Λ (i.e., $\gtrsim 1$) the system ends up in the state $|S, 0\rangle_x$, for which the QFI scales as $2S^2+2S$. This is still quadratic, and still clearly better than the scaling of standard quantum-limit states. This only slightly lesser scaling of the QFI means that $|S, 0\rangle_x$ has similar potential for use in quantum metrology to the cat state considered earlier.

10.4.3 Spontaneous Emission

In the cavity QED framework, off-resonant excitation of atomic excited states by the Raman lasers leads to residual spontaneous emission that affects all atoms individually. In the atomic ground state manifold, the effects of this can be modelled by local dephasing ($\hat{S}_z^{(n)}$), excitation ($\hat{S}_+^{(n)}$), or deexcitation ($\hat{S}_-^{(n)}$), with the (no-jump) master equation modified to

$$\dot{\hat{\rho}} = -i\Big[\hat{\mathcal{H}}, \hat{\rho}\Big] + \frac{\gamma_{\text{eff}}}{2} \sum_n^N \Big(\mathcal{D}[\hat{S}_z^{(n)}]\hat{\rho} + \mathcal{D}[\hat{S}_+^{(n)}]\hat{\rho} + \mathcal{D}[\hat{S}_-^{(n)}]\hat{\rho} \Big), \tag{10.36}$$

where for simplicity we assume that the local effects all occur at the effective rate γ_{eff}.

Again we can use the permutational invariance of the system, as described earlier and, also for simplicity, we consider just spin-1/2 atoms. With regard to the effects of spontaneous emission, we do not expect a significant difference between the spin-1/2 and spin-1 cases.

In practice, we include both evolution with the collective and individual decay operators at the same time by performing in each time step a short evolution with the collective term followed by a short evolution with PIQS,

$$\hat{\rho}(t+\delta t) = e^{(\mathcal{L}_\Lambda + \mathcal{L}_{\gamma_{\text{eff}}})\delta t} \Big[e^{-\Gamma \hat{J}_x^2 \delta t} \hat{\rho}(t) e^{-\Gamma \hat{J}_x^2 \delta t} \Big], \tag{10.37}$$

where $\mathcal{L}_\Lambda$ corresponds to the Hermitian part of the Hamiltonian and $\mathcal{L}_{\gamma_{\text{eff}}}$ is the Liouvillian operator corresponding to the second line of (10.36). Note that due to the way in which PIQS separates the collective and local effects, it turns out that doing the whole evolution with the local effects and afterwards overlaying the evolution of the collective effects show the same final results.

Numerical results for the fidelity and QFI as a function of the dissipative rate $\gamma_{\text{eff}}/\Lambda$ are shown in Fig. 10.7. Single-particle processes mix subspaces of different spin lengths, which increases the number of spin states available to the system and hence the size of the basis required for simulations. This means

that our results are generally restricted to smaller spin lengths S. As can be seen in Fig. 10.7, the fidelity and QFI both show a greater sensitivity to $\gamma_{\text{eff}}/\Lambda$ than to Γ/Λ, with the QFI now dropping off with $\gamma_{\text{eff}}/\Lambda$ in a similar fashion to the fidelity. To maintain high values of the QFI clearly requires $\gamma_{\text{eff}}/\Lambda < 10^{-2}$. We note also that both the fidelity and the QFI go to zero once $\gamma_{\text{eff}}/\Lambda \gtrsim 1$.

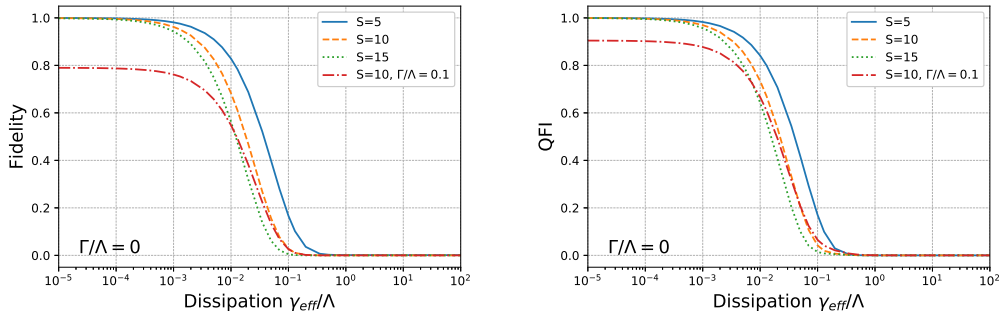

Figure 10.7: Fidelity (left) and QFI (right) as a function of the strength of dissipation $\gamma_{\text{eff}}/\Lambda$ at the time $t = \pi/(2\Lambda)$, given that no jump (cavity photon emission) has occurred when $\Gamma > 0$. The QFI is plotted relative to the theoretical maximum, $4S^2$.

10.4.4 Possible Experimental Parameters

Considering the spin-1 realisation of the Dicke model with ^{87}Rb, the effective one-axis twisting parameter in the limit $\omega \gg \kappa$ is

$$\Lambda = \frac{g^2}{72\omega}\frac{\Omega^2}{\Delta^2}, \tag{10.38}$$

and $\Gamma = (\kappa/\omega)\Lambda$. Meanwhile, the effective rate of atomic spontaneous emission due to off-resonant excitation of the excited hyperfine level $5^2P_{1/2}$ is estimated to be

$$\gamma_{\text{eff}} \simeq \frac{\gamma}{12}\frac{\Omega^2}{\Delta^2}, \tag{10.39}$$

where γ is the spontaneous emission line width of the $5^2P_{1/2}$ level. Hence, we have $\gamma_{\text{eff}}/\Lambda \simeq 6\gamma\omega/g^2 = (12/C)(\omega/\kappa)$, where $C = 2g^2/(\kappa\gamma)$ is the single-

atom cooperativity. Minimising both Γ/Λ and $\gamma_{\text{eff}}/\Lambda$ therefore puts a very demanding requirement on the cooperativity C. For example, if we consider $\Gamma/\Lambda = \kappa/\omega = 0.1$, then to achieve $\gamma_{\text{eff}}/\Lambda = 10^{-3}$ would require $C = 120,000$. So, perhaps not unsurprisingly, it is very difficult to ensure Hamiltonian-dominated evolution in this cavity-QED-based scheme whilst also protecting the well-known fragility of the mesoscopic superposition states from the effects of spontaneous emission.

Finally, we must note also that fluctuations in the number of atoms (i.e., in S) can be relevant in these cavity QED experiments with cold atoms [34], since Λ is in principle dependent on atom number through the dependence of ω on the term $Sg^2/(3\Delta)$ (and also since for spin-1/2 particles the fluctuations will lead to non-integer S). So, fluctuations in atom number will in principle cause fluctuations in Λ and hence also in the preparation time. However, as long as the detuning of the cavity mode from the lasers, $\omega_c - \omega_\pm$, is sufficiently large, and thus dominates over the term $Sg^2/(3\Delta)$ in the expression for ω, then the effect of atom number fluctuations should be minimal.

Of course, for the typical numbers of atoms that we consider here, another possibility would be a well-controlled number of atoms held in an array of optical tweezers, with each tweezer containing one atom, which is certainly a viable technology nowadays [157, 158]. (Similarly, in a trapped-ion configuration, the number of ions can be precisely determined.) In the spin-1/2 case, this would also solve the issue of having an even number of atoms to ensure an integer value of S, which all of our results assume. However, the spin-1 realisation of the Dicke model also offers a simple solution to this issue, as the total spin necessarily takes an integer value.

10.4.5 Preparation of the Dicke state $|S,0\rangle_x$

A more promising target for the cavity QED framework is in fact preparation of the Dicke state $|S,0\rangle_x$, which still shows a quadratic scaling of the QFI with spin length ($2S^2+2S$).

As we saw earlier, with increasing spin length the probability to have no photon emission decreases with increasing Γ or for large t, but there is still

always a finite probability of having no cavity emissions, which in the absence of spontaneous emission heralds the preparation of the state $|S,0\rangle_x$. A simple formula for this probability can be obtained using Stirling's approximation ($S! \approx S^S e^S \sqrt{2\pi S}$) as [143]

$$P_{m=0} = (D^S_{0,S})^2 \approx \frac{1}{\sqrt{\pi S}}. \tag{10.40}$$

So, the rate of decrease with S is actually somewhat slow; e.g., for $S = 30$ the probability is still 10%. Note also that, as we shall see in the next Section, if a photon emission does occur, then it triggers an ongoing sequence of photon emissions. So, in practice, the distinction between preparation (no photon emission) and non-preparation (continual photon emission) of the state $|S,0\rangle_x$ in any particular run of the experiment should be clear.

For this alternative target state, the preparation can be entirely dissipative in nature; that is, we can simply set $\omega = 0$ (so $\Lambda = 0$) and the rate at which the state is prepared is then determined by

$$\Gamma = \frac{g^2}{72\kappa}\frac{\Omega^2}{\Delta^2}. \tag{10.41}$$

In particular, the $m \neq 0$ components of the initial state decay like $e^{-m^2\Gamma t}$. Meanwhile, to avoid the effects of spontaneous emission we now only require $\gamma_{\text{eff}}/\Gamma = 12/C \ll 1$. Microcavity experiments with ^{87}Rb atoms can already achieve $C \gtrsim 300$ [3] corresponding to $\gamma_{\text{eff}}/\Gamma \lesssim 0.04$, while nanocavity experiments show promise of much larger cooperativities [6].

In Fig. 10.8 it can be seen that the fidelity and QFI are considerably impacted by spontaneous emission. The preparation of the Dicke state does not require a specific time. Thus, fidelity and QFI at low dissipation rates $\gamma_{\text{eff}}/\Gamma$ may be sacrificed for better results at higher rates by choosing smaller times, effectively trading stronger decay of the $m \neq 0$ components of the initial state for less time being exposed to spontaneous emission. For an efficient state preparation results $\gamma_{\text{eff}}/\Gamma \sim 10^{-2}$ would be required.

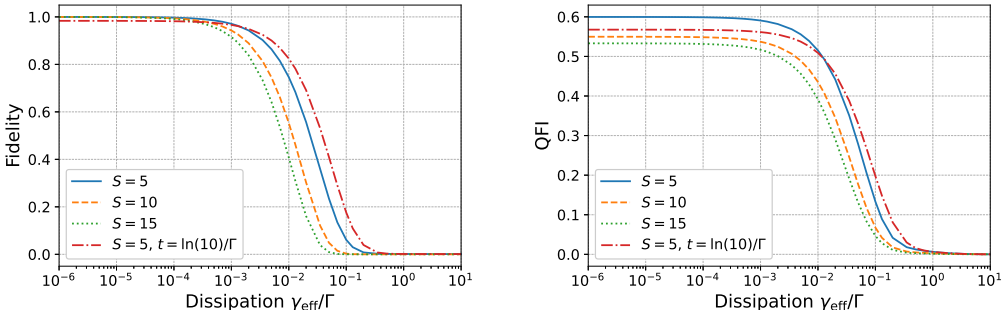

Figure 10.8: Fidelity to the state $|S,0\rangle_x$ (left) and QFI (right) as a function of the relative strength of the two dissipations $\gamma_{\text{eff}}/\Gamma$ at the time $t = 2\ln(10)/\Gamma$ (and $t = \ln(10)/\Gamma$), given that no jump (cavity photon emission) has occurred when $\Gamma > 0$. The QFI is plotted relative to the theoretical maximum, $4S^2$.

10.4.6 Jump trajectory: Entangled-State Cycles

Let us assume that the cavity-mediated dynamics dominates over effects associated with spontaneous emission. By realising that

$$D^S_{-m,S} = D^S_{m,S}, \tag{10.42}$$

we can rewrite the wave function (10.16) as

$$\begin{aligned} |\psi(t)\rangle &= \frac{\sum_m D^S_{m,S} e^{i\Lambda m^2 t} e^{-\Gamma m^2 t} |S,m\rangle_x}{\sqrt{\sum_m e^{-2\Gamma m^2 t} (D^S_{m,S})^2}} \\ &= \frac{D^S_{0,S}|S,0\rangle_x + \sum_{m=1}^{S} D^S_{m,S} e^{-\Gamma m^2 t}\sqrt{2}|\chi^+_S(m)\rangle}{\sqrt{\sum_m e^{-2\Gamma m^2 t} (D^S_{m,S})^2}}, \end{aligned} \tag{10.43}$$

where $|\chi^{\pm}_S(m)\rangle$ are the "kitten" states

$$|\chi^{\pm}_S(m)\rangle = \frac{e^{i\Lambda m^2 t}}{\sqrt{2}}(|S,m\rangle_x \pm |S,-m\rangle_x). \tag{10.44}$$

These are just cat states in a different basis, "smaller" (for $m < S$) than those considered earlier, but for which the QFI (relative to the generator $\hat{J}_x$) still scales like $4m^2$. Hence, even with the occurrence of a jump in the dynamics, a highly entangled and potentially useful state can still be generated. In particular, once a jump happens, the jump operator, being proportional to $\hat{J}_x$, makes it so that the $m = 0$ component of the initial state vanishes and the $|\chi_S^{\pm}(m)\rangle$ states change their relative phase by π:

$$\hat{J}_x|\chi_S^{\pm}(m)\rangle = m|\chi_S^{\mp}(m)\rangle. \tag{10.45}$$

The system then, after some time, settles probabilistically into one of S possible cycles of jumps each cycle corresponding to a different pair $|\chi_S^{\pm}(m)\rangle$ (with an overall probability of $2(D^S_{m,S})^2$ for a given m) and the jumps between these two states of a given pair $|\chi_S^{+}(m)\rangle$ and $|\chi_S^{-}(m)\rangle$ continue *indefinitely*.

We can determine in which cycle the system has settled by observing the rate at which photons are emitted, as this rate depends quadratically on m, i.e.,

$$\langle\chi_S^{\pm}(m)|\hat{J}_x^2|\chi_S^{\pm}(m)\rangle = m^2. \tag{10.46}$$

In Fig. 10.9 we show a couple of examples of such jump trajectories. In particular, we plot the overlaps of the system state $|\psi(t)\rangle$ with the various eigenstates of $\hat{J}_x$. We see clearly how jumps lead to a relative sign change between the components $|S, \pm m\rangle_x$, and also how the frequency of jumps increases with increasing m.

The particular cycle in which the system ends up is random, but is in general strongly influenced by the time at which the first jump happens. An early jump may increase the relative amplitude of a higher-m cycle above that of some lower ones, and therefore steer the system towards a higher-m cycle, while the longer the first jump takes to happen, the more likely it is for lower-m cycles to be established, since only these remain with significant amplitudes.

Note that the highest-m cycles rarely appear, since their amplitudes are so suppressed that even an immediate jump would not make them significant. In fact, for j immediate jumps, the relative amplitudes of the states $|S, m\rangle_x$ become

$$m^j 2^{-S} \sqrt{\binom{2S}{S+m}} \approx \frac{m^j}{\sqrt{\pi S}} e^{-\frac{m^2}{S}}, \tag{10.47}$$

which makes little difference for the largest m.

Once one m-cycle starts to dominate it is unlikely for the system to evolve to another cycle, as the dominant cycle determines the probability of jumps and hence the frequency (but this is not impossible, as can be seen in Fig. 10.9 (bottom), where the system transitions from being a higher-m cycle to the $m = 2$-cycle after a small period of less frequent jumps). One essentially sees a positive feedback loop relationship between the jump frequency and the population of a specific entangled-state cycle.

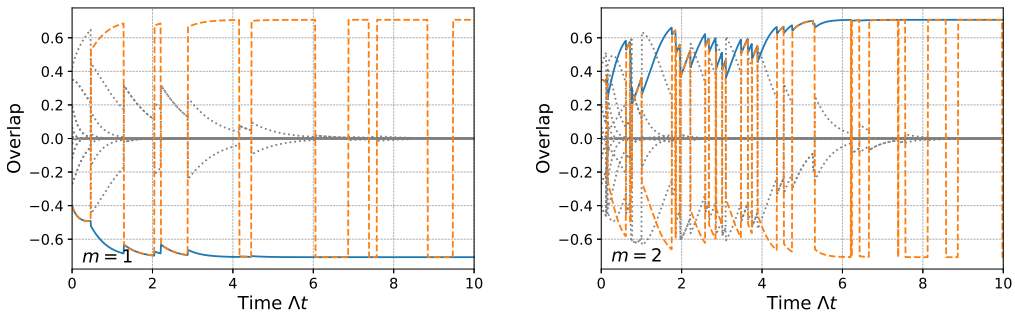

Figure 10.9: Monte Carlo simulations of the overlap of the system state with the eigenstates of $\hat{S}_x$. We plot $\langle\psi(t)|S, m\rangle_x$ (solid blue) and $\langle\psi(t)|S, -m\rangle_x$ (dashed orange) for the m-value that corresponds to the final, surviving entangled-state cycle, and the remaining overlaps (dotted grey) as a function of time for single trajectories of spin $S = 10$, with $\Gamma/\Lambda = 0.5$. The two trajectories show a cycle with $m = 1$ (left) and $m = 2$ (right). Note that we have removed the phase factor $e^{i\Lambda m^2 t}$ from all of the overlaps.

10.4.7 Steering a kitten state to a cat state

Since the entangled-state cycles with high m correspond to cat states we would like to increase the chance of landing in one of those. We propose here two ideas of for that might be implemented.

Because of the aforementioned positive feedback loop, we explore now the implementation of a $\hat{J}_x$ quantum gate that we could then apply to the spin state as an impulse train (of period T) of the form

$$\hat{J}_x \sum_j \delta(t - jT), \qquad \Lambda T \ll 1. \tag{10.48}$$

The spin matrices would have to be implemented through non-Hamiltonian techniques due to their non-unitary nature.

We have two options for how to apply it:

The first option is to apply these pulses intermittently during most of the evolution, ensuring that the system does not probabilistically evolve into another cycle. This ensures that always the right cycle is hit, but both Hamiltonians acting at the same time might introduce some errors if the pulse time is not short enough.

The second option is to just apply the pulses prior to the one axis twisting Hamiltonian. This means that if the system can still probabilistically evolve into another cycle, but especially if we only care about the highest cycle, this probability can be highly suppressed by applying the quantum gate a sufficiently high number of times.

An exemplary trajectory of the second option can be found in Fig. 10.10. To ensure a transition to the highest entangled-state cycle, the quantum gate has to be applied enough times so that the $|S, S\rangle_x$-component dominates the initial superposition, i.e.,

$$\frac{\langle \chi_S^{\pm}(m)|\hat{J}_x^j|\psi(0)\rangle}{\langle \psi(0)|\hat{J}_x^j|\psi(0)\rangle} = \frac{D^S_{S,S} S^j}{\sqrt{\sum_m \left(D^S_{m,S} m^j\right)^2}} \xrightarrow{j\to\infty} 1. \tag{10.49}$$

This means that in theory, applying $\hat{J}_x$ an infinite amount should also generate a spin cat state and what we are effectively doing is enhancing the overlap between the initial state and the spin cat state. We then let the system settle itself into that cat state.

Besides $\hat{J}_x$ another way to generalise the Pauli spin matrix $\hat{\sigma}_x$ to higher dimensions, thinking about it more in terms of a NOT-gate, is the shift matrix

$$\hat{U} = |S, S\rangle_x\langle S, -S|_x + \sum_{m=-S+1}^{S} |S, m-1\rangle_x\langle S, m|_x. \tag{10.50}$$

Such a quantum gate has been implemented for the orbital angular momenta of a photon [159–161]. In our case, the initial application of this operator in the eigenbasis of $\hat{J}_x$ would allow us to shift the high populations of the low m entangled-state cycles to the high m entangled-state cycles.

Let us consider the case of an integer spin, with an odd number of Dicke states, and the system being in the mth entangled-state cycle (again verifiable from the frequency of photon emissions) before we apply the shift matrix S (or $S+1$) times There is the additional issue that the superposition ends up being made up of two components from two different entangled-state cycles, e.g.,

$$|\psi_{\text{integer}}\rangle = \frac{1}{\sqrt{2}}(|S, S-m\rangle_x \pm |S, -S-1+m\rangle_x), \tag{10.51}$$

which will most likely still be a mesoscopic superposition if S is sufficiently large, since high m are strongly suppressed. Because these two components induce jumps at vastly different rates ($\propto m^2$), the state will become biased and in the long run only one component will survive, meaning this is another way to prepare Dicke states.

Even though the rest of the chapter is exclusive to integer spins, the present effect is not, so let us also take a look at a half-integer spin. In that case we

have to apply the operator $\frac{2S+1}{2}$ times to obtain

$$|\psi_{\text{half-integer}}\rangle = \frac{1}{\sqrt{2}}(|S, S-m\rangle_x \pm |S, -S+m\rangle_x). \tag{10.52}$$

Examples of trajectories for integer and half-integer spin are depicted in Fig. 10.10.

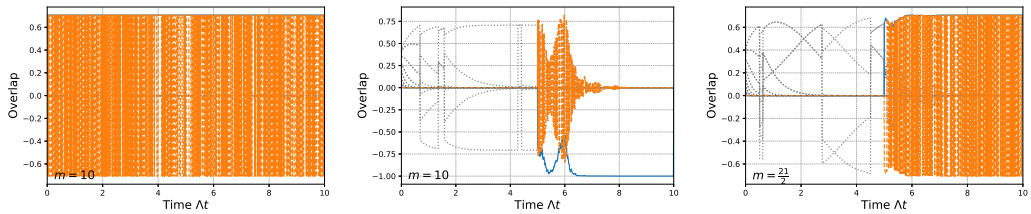

Figure 10.10: Monte Carlo simulations of the overlap (computed as described prior) of the eigenstates of $\hat{J}_x$. We plot $|S, m\rangle_x$ (solid blue), $|S, -m\rangle_x$ (dashed orange) that make up the final (here the highest, i.e. $m = S$) entangled-state cycle and the rest (dotted grey) as a function of time for single trajectories of spin $S = 10$, $\frac{\Gamma}{\Lambda} = 0.5$. The three trajectories show a cycle with $m = 10$ induced by applying $\hat{J}_x$ 100 times at the start (left) or $S = 10$ times (middle), and a cycle with $S = \frac{21}{2}$ obtained by applying $\hat{U}$ $(S+\frac{1}{2})$ times (right) at a time $\Lambda t = 5$.

10.5 Conclusions and Outlook

To summarise, we have proposed a scheme for generating spin cat states using an engineered Dicke model. The scheme could be implemented in two different physical systems: trapped ions and cavity QED. Each comes with their own benefits: the trapped ion variant is more robust against decoherence, while the cavity QED case has the option to generate alternative states such as kitten states and the state $|S, 0\rangle_x$, both of which are identifiable from the cavity output (photon flux).

One could also think about using a cavity Q-switch [162] once a photon has been detected to change from a high quality factor Q cavity to a low Q one to increase Γ and therefore the speed at which the entangled-state cycles is reached.

Part V

Back Matter

Chapter 11

Conclusions and Outlook

Let us discuss the main results from this thesis, starting with Chapters 7 and 8 and the on-demand generation of optical N-photon states. We are convinced that our proposed schemes offer very realistic (and topical, in the context of fibre-integrated micro- and nanophotonic platforms) means to achieve a deterministic N-photon source, which is an outstanding problem in experimental quantum optics. The solution to this issue will offer exciting applications, attracting particular attention from the quantum optics, quantum computing, and quantum communication communities. The cavity QED parameters that we use are either taken directly from, or are very similar to, the parameters in state-of-the-art experiments. The use of the entire atomic level structure in a single-atom cavity QED system to achieve the desired behaviour is also innovative and of general interest to the fields of quantum optics and atomic physics. The truly deterministic nature of the scheme, and the fact that it does not rely on temporal control of fields, sets it apart from virtually all other competing proposals for N-photon sources in the optical regime. We also demonstrated the possibility for an efficient and faithful reduction of the full dynamics of an alkali atom coupled to a cavity mode to that of a simple Tavis-Cummings (or anti-Tavis-Cummings) model for a spin-F system. This enables an effective superradiant behaviour of the composite system, even though only a single atom is involved, which constitutes a significant novelty. Some open questions remain when it comes to the quantum tomography, more specifically the

temporal filtering. We saw that at times the filtering and thus the state reconstruction fail, even though the photon counting results confirm that the desired Fock state was realised. This seems to be linked to the filter function possessing high-frequeny components for a particular atom/laser configurations. Future project ideas include studying this more extensively, its origin, and possible ramifications for experimental implementations. During our investigation we definitely noticed how choosing a filter not based on the amplitude correlation function, e.g., based on the output photon flux or atomic correlation functions, would also lead to respectable results. So, whether our choice is the optimal one remains to be seen. The observation of rotated Wigner functions in the resonant case also sparks the question whether such an effect should be present in the far-detuned case as well, and was ignored through the approximation via a Tavis-Cummings model, since that by itself cannot create such an effect. One could investigate this by including the lower hyperfine state Tavis-Cummings model, e.g., for ^{87}Rb, a sum of the $F = 1$ and $F = 2$ versions (with one of them being detuned by an additional amount ω_{HF}) plus additional off-resonant Raman process ($\propto \frac{g^2\Omega^2}{\omega_{HF}^2\Delta^2}$). In the end this rate and the coupling in the additional Tavis-Cummings model end up being much smaller, which with the additional low population of $F = 1$ should make that effect very small, as even in resonance it is unnoticeable most of the time. Input-output simulations of the full model confirm this.

In Chapter 9 we have given a brief overview of the dynamics of this novel two-mode cavity QED system. We presented foundations for the theoretical description and showed how the output light exhibits quantum signatures such as antibunching or the violation of the Cauchy-Schwarz Inequalities. However, the chapter is probably the most open-ended of this thesis. Regarding the one-atom laser, we have started exploring possible venues towards time-bin-entangled photons [163, 164]. The idea here is to start with a superposition of the two ground states and no photons in either of the two cavity modes, i.e., $|3\rangle|0\rangle_a|0\rangle_b+|4\rangle|0\rangle_a|0\rangle_b$, and to transfer that superposition to a superposition where one photon is put in each cavity mode, e.g., $|4\rangle|1\rangle_a|0\rangle_b+|3\rangle|0\rangle_a|1\rangle_b$ with a pulsed laser sequence. If this process is repeated and the photons escape the cavity, we have $|3\rangle|0\rangle_a|0\rangle_b|\omega_a\rangle_1|\omega_b\rangle_2+|4\rangle|0\rangle_a|0\rangle_b|\omega_b\rangle_1|\omega_a\rangle_2$, where

the subscript 1 or 2 indicates the order in which the photons exit the system and a and b from which mode they came. After disentangling the atom with a microwave $\pi/2$-pulse, we should observe some energy-time entanglement, $|3\rangle|0\rangle_a|0\rangle_b(|\omega_b\rangle_1|\omega_a\rangle_2-|\omega_a\rangle_1|\omega_b\rangle_2)+|4\rangle|0\rangle_a|0\rangle_b(|\omega_b\rangle_1|\omega_a\rangle_2+|\omega_a\rangle_1|\omega_b\rangle_2)$, a state that would violate the following steering inequality: $\Delta(\omega_1+\omega_2)\Delta(t_2-t_1) \geq 1$. Stimulated Raman adiabatic passage (STIRAP) [165] in its traditional form is not really feasible, since the system does not have a dark state (effective model Version II). We started investigating possible laser pulse sequences using quantum optimal control methods [166], but generating these superpositions with high fidelity so far hinged on treating the system as a closed system.

Another idea is to include the quantised trap motion of the atom into our models, might make it possible to combine the cyclic evolution of the system with cavity-assisted cooling of the motion [167]. This could help stabilise the experimental setup.

Chapter 10 represents a potential solution to the problem of generating entangled states in large ensembles of atoms. That one-axis twisting has the potential to create cat states was known before, but the novel engineering of it from a Dicke model creates a distinct model, where the non-jump part of the dissipative evolution also takes the form of one axis-twisting. Again, we examined parameter regimes from state-of-the-art cavity and trapped ion experiments. From these two, the trapped ions end up being more promising because of the vanishing collective noise from heating and the manageable single-particle dephasing. Here, however, the spin cat state production is restricted to trapped-ion experiments, while the cooperativities required for a cavity QED implementation still lie in the (hopefully near) future. The cavity QED setup has the benefit of offering a potential fail-safe to fall back onto a smaller cat state in case of a photodetection. The usefulness and potential manipulation of the entangled-state cycles remains speculative. Future directions could be to look more closely at them, in which case one would have to start looking into how single-particle decoherence processes affect these. Since single-particle operators jump between different Dicke subspaces, entangled-states cycles should be superpositions made up of Dicke states from different

subspaces. Other than that, the decay and pumping of individual spins would shift the magnetic quantum number of the two components of the kitten state by the same amount, thus creating superpositions of different m which decay at different speeds, or even potentially removing it if $m = \pm S$.

The aim of this thesis is to propose and examine a series of schemes dedicated to the generation of exotic quantum states both in light and atomic ensembles. While doing so, we built on the pioneering work on engineered Dicke models in cavity quantum electrodynamics systems and added to that by extending it to more atomic species and levels. Between the effective Lindblad operator formalism, the permutational quantum solver and input-output theory for quantum pulses, this thesis also experiments with some novel methods from the world of quantum optics. The ideas that we developed in this thesis put forth some exciting future directions, the biggest being their potential experimental implementation. The realisation of the one-atom-laser with two cavity modes is already a work in progress [128]. The big variety in and relative simplicity that our work on N-photon pulses offer should also make it appealing in this respect, and indeed the Hoogerland group at the University of Auckland is already proposing an experiment.

Bibliography

[1] J. Johansson, P. Nation, and F. Nori, "QuTiP: An open-source Python framework for the dynamics of open quantum systems," Computer Physics Communications **183**, 1760 – 1772 (2012).

[2] J. Johansson, P. Nation, and F. Nori, "QuTiP 2: A Python framework for the dynamics of open quantum systems," Computer Physics Communications **184**, 1234 – 1240 (2013).

[3] R. Gehr, J. Volz, G. Dubois, T. Steinmetz, Y. Colombe, B. L. Lev, R. Long, J. Estève, and J. Reichel, "Cavity-Based Single Atom Preparation and High-Fidelity Hyperfine State Readout," Phys. Rev. Lett. **104**, 203602 (2010).

[4] F. Haas, J. Volz, R. Gehr, J. Reichel, and J. Estève, "Entangled States of More Than 40 Atoms in an Optical Fiber Cavity," Science **344**, 180–183 (2014).

[5] G. Barontini, L. Hohmann, F. Haas, J. Estève, and J. Reichel, "Deterministic generation of multiparticle entanglement by quantum Zeno dynamics," Science **349**, 1317 (2015).

[6] J. D. Thompson, T. Tiecke, N. P. de Leon, J. Feist, A. Akimov, M. Gullans, A. S. Zibrov, V. Vuletić, and M. D. Lukin, "Coupling a single trapped atom to a nanoscale optical cavity," Science **340**, 1202–1205 (2013).

[7] T. Tiecke, J. D. Thompson, N. P. de Leon, L. Liu, V. Vuletić, and

M. D. Lukin, "Nanophotonic quantum phase switch with a single atom," Nature **508**, 241 (2014).

[8] P. Samutpraphoot, T. Đorđević, P. L. Ocola, H. Bernien, C. Senko, V. Vuletić, and M. D. Lukin, "Strong Coupling of Two Individually Controlled Atoms via a Nanophotonic Cavity," Phys. Rev. Lett. **124**, 063602 (2020).

[9] S.-H. Tan and P. P. Rohde, "The resurgence of the linear optics quantum interferometer-recent advances & applications," Reviews in Physics **4**, 100030 (2019).

[10] S. Slussarenko and G. J. Pryde, "Photonic quantum information processing: A concise review," Applied Physics Reviews **6**, 041303 (2019).

[11] F. Flamini, N. Spagnolo, and F. Sciarrino, "Photonic quantum information processing: a review," Reports on Progress in Physics **82**, 016001 (2018).

[12] J. L. O'Brien, A. Furusawa, and J. Vučković, "Photonic quantum technologies," Nature Photonics **3**, 687 (2009).

[13] P. Kok, W. J. Munro, K. Nemoto, T. C. Ralph, J. P. Dowling, and G. J. Milburn, "Linear optical quantum computing with photonic qubits," Reviews of Modern Physics **79**, 135 (2007).

[14] H. J. Kimble, "The quantum internet," Nature **453**, 1023–1030 (2008).

[15] J. L. O'brien, "Optical quantum computing," Science **318**, 1567–1570 (2007).

[16] L. Krivitsky and V. Volkov, "The role of photon statistics in visual perception," in *Quantum Photonics: Pioneering Advances and Emerging Applications*, edited by R. W. Boyd, S. G. Lukishova, and V. N. Zadkov (Springer International Publishing, Cham, 2019) pp. 207–237.

[17] N. Sim, M. F. Cheng, D. Bessarab, C. M. Jones, and L. A. Krivitsky, "Measurement of Photon Statistics with Live Photoreceptor Cells," Phys. Rev. Lett. **109**, 113601 (2012).

[18] N. M. Phan, M. F. Cheng, D. A. Bessarab, and L. A. Krivitsky, "Interaction of Fixed Number of Photons with Retinal Rod Cells," Phys. Rev. Lett. **112**, 213601 (2014).

[19] P. I. Sia, A. N. Luiten, T. M. Stace, J. P. M. Wood, and R. J. Casson, "Quantum biology of the retina," Clinical & Experimental Ophthalmology **42**, 582–589 (2014).

[20] K. K. Sabapathy and C. Weedbrook, "ON states as resource units for universal quantum computation with photonic architectures," Phys. Rev. A **97**, 062315 (2018).

[21] M. H. Michael, M. Silveri, R. T. Brierley, V. V. Albert, J. Salmilehto, L. Jiang, and S. M. Girvin, "New Class of Quantum Error-Correcting Codes for a Bosonic Mode," Phys. Rev. X **6**, 031006 (2016).

[22] L. Hu, Y. Ma, W. Cai, X. Mu, Y. Xu, W. Wang, Y. Wu, H. Wang, Y. Song, C.-L. Zou, S. M. Grivin, L.-M. Duan, and L. Sun, "Quantum error correction and universal gate set operation on a binomial bosonic logical qubit," Nature Physics **15**, 503–508 (2019).

[23] Y. Yamamoto and H. A. Haus, "Preparation, measurement and information capacity of optical quantum states," Rev. Mod. Phys. **58**, 1001–1020 (1986).

[24] C. M. Caves and P. D. Drummond, "Quantum limits on bosonic communication rates," Rev. Mod. Phys. **66**, 481–537 (1994).

[25] S. Slussarenko, M. M. Weston, H. M. Chrzanowski, L. K. Shalm, V. B. Verma, S. W. Nam, and G. J. Pryde, "Unconditional violation of the shot-noise limit in photonic quantum metrology," Nature Photonics **11**, 700–703 (2017).

[26] J.-W. Pan, Z.-B. Chen, C.-Y. Lu, H. Weinfurter, A. Zeilinger, and M. Żukowski, "Multiphoton entanglement and interferometry," Rev. Mod. Phys. **84**, 777–838 (2012).

[27] T. Nagata, R. Okamoto, J. L. O'Brien, K. Sasaki, and S. Takeuchi, "Beating the standard quantum limit with four-entangled photons," Science **316**, 726–729 (2007).

[28] M. W. Mitchell, J. S. Lundeen, and A. M. Steinberg, "Super-resolving phase measurements with a multiphoton entangled state," Nature **429**, 161–164 (2004).

[29] L. Pezzé and A. Smerzi, "Ultrasensitive Two-Mode Interferometry with Single-Mode Number Squeezing," Phys. Rev. Lett. **110**, 163604 (2013).

[30] R. A. Campos, C. C. Gerry, and A. Benmoussa, "Optical interferometry at the Heisenberg limit with twin Fock states and parity measurements," Phys. Rev. A **68**, 023810 (2003).

[31] M. J. Holland and K. Burnett, "Interferometric detection of optical phase shifts at the Heisenberg limit," Phys. Rev. Lett. **71**, 1355–1358 (1993).

[32] Y. Kawaguchi and M. Ueda, "Spinor Bose-Einstein condensates," Physics Reports **520**, 253–381 (2012).

[33] D. M. Stamper-Kurn and M. Ueda, "Spinor Bose gases: Symmetries, magnetism, and quantum dynamics," Rev. Mod. Phys. **85**, 1191–1244 (2013).

[34] E. J. Davis, G. Bentsen, L. Homeier, T. Li, and M. H. Schleier-Smith, "Photon-Mediated Spin-Exchange Dynamics of Spin-1 Atoms," Phys. Rev. Lett. **122**, 010405 (2019).

[35] M. Landini, N. Dogra, K. Kroeger, L. Hruby, T. Donner, and T. Esslinger, "Formation of a Spin Texture in a Quantum Gas Coupled to a Cavity," Phys. Rev. Lett. **120**, 223602 (2018).

[36] K. C. Stitely, S. J. Masson, A. Giraldo, B. Krauskopf, and S. Parkins, "Superradiant switching, quantum hysteresis, and oscillations in a generalized Dicke model," Phys. Rev. A **102**, 063702 (2020).

[37] K. C. Stitely, A. Giraldo, B. Krauskopf, and S. Parkins, "Nonlinear semiclassical dynamics of the unbalanced, open Dicke model," Phys. Rev. Research **2**, 033131 (2020).

[38] L. Pezzè, A. Smerzi, M. K. Oberthaler, R. Schmied, and P. Treutlein, "Quantum metrology with nonclassical states of atomic ensembles," Rev. Mod. Phys. **90**, 035005 (2018).

[39] R. Hudson, "When is the Wigner quasi-probability density non-negative?" Reports on Mathematical Physics **6**, 249–252 (1974).

[40] U. Chabaud, P.-E. Emeriau, and F. Grosshans, "Witnessing Wigner Negativity," Quantum **5**, 471 (2021).

[41] J. Garrison and R. Chiao, *Quantum Optics*, Oxford Graduate Texts (OUP Oxford, 2008).

[42] J. Evers, "Quantum optics lecture notes," (2016).

[43] H. Carmichael, *An Open Systems Approach to Quantum Optics*, Bd. 18 (Springer Berlin Heidelberg, 1993).

[44] K. Mølmer, Y. Castin, and J. Dalibard, "Monte Carlo wave-function method in quantum optics," J. Opt. Soc. Am. B **10**, 524–538 (1993).

[45] R. Dum, P. Zoller, and H. Ritsch, "Monte Carlo simulation of the atomic master equation for spontaneous emission," Phys. Rev. A **45**, 4879–4887 (1992).

[46] M. Lax, "Formal Theory of Quantum Fluctuations from a Driven State," Phys. Rev. **129**, 2342–2348 (1963).

[47] C. Foot, *Atomic Physics*, Oxford Master Series in Physics (OUP Oxford, 2004).

[48] E. Arimondo, M. Inguscio, and P. Violino, "Experimental determinations of the hyperfine structure in the alkali atoms," Rev. Mod. Phys. **49**, 31–75 (1977).

[49] D. A. Steck, "Rubidium 87 D line data," (2019).

[50] D. A. Steck, "Cesium D line data," (2019).

[51] M. Scully and M. Zubairy, *Quantum Optics* (Cambridge University Press, 1997).

[52] M. Fox, *Quantum Optics: An Introduction*, Oxford Master Series in Physics (OUP Oxford, 2006).

[53] C. W. Gardiner and M. J. Collett, "Input and output in damped quantum systems: Quantum stochastic differential equations and the master equation," Phys. Rev. A **31**, 3761–3774 (1985).

[54] P. Berman, *Cavity Quantum Electrodynamics*, Advances in Atomic, Molecular, and Optical Physics: Supplement 2 (Academic Press, 1994).

[55] H. Yokoyama and K. Ujihara, *Spontaneous Emission and Laser Oscillation in Microcavities*, Laser & Optical Science & Technology (Taylor & Francis, 1995).

[56] P. Rice and H. Carmichael, "Single-atom cavity-enhanced absorption. I. Photon statistics in the bad-cavity limit," IEEE Journal of Quantum Electronics **24**, 1351–1366 (1988).

[57] R. Loudon, "Non-classical effects in the statistical properties of light," Reports on Progress in Physics **43**, 913–949 (1980).

[58] D. Walls and G. Milburn, *Quantum Optics*, Springer Study Edition (Springer Berlin Heidelberg, 1995).

[59] S. V. Polyakov, C. W. Chou, D. Felinto, and H. J. Kimble, "Temporal Dynamics of Photon Pairs Generated by an Atomic Ensemble," Phys. Rev. Lett. **93**, 263601 (2004).

[60] S. L. Mielke, G. T. Foster, and L. A. Orozco, "Nonclassical Intensity Correlations in Cavity QED," Phys. Rev. Lett. **80**, 3948–3951 (1998).

[61] K. Hepp and E. H. Lieb, "On the superradiant phase transition for molecules in a quantized radiation field: the Dicke maser model," Annals of Physics **76**, 360–404 (1973).

[62] K. Rzażewski, K. Wódkiewicz, and W. Żakowicz, "Phase Transitions, Two-Level Atoms, and the A^2 Term," Phys. Rev. Lett. **35**, 432–434 (1975).

[63] F. Dimer, B. Estienne, A. S. Parkins, and H. J. Carmichael, "Proposed realization of the Dicke-model quantum phase transition in an optical cavity QED system," Phys. Rev. A **75**, 013804 (2007).

[64] Z. Zhang, C. H. Lee, R. Kumar, K. J. Arnold, S. J. Masson, A. L. Grimsmo, A. S. Parkins, and M. D. Barrett, "Dicke-model simulation via cavity-assisted Raman transitions," Phys. Rev. A **97**, 043858 (2018).

[65] Z. Zhiqiang, C. H. Lee, R. Kumar, K. J. Arnold, S. J. Masson, A. S. Parkins, and M. D. Barrett, "Nonequilibrium phase transition in a spin-1 Dicke model," Optica **4**, 424–429 (2017).

[66] F. Brennecke, R. Mottl, K. Baumann, R. Landig, T. Donner, and T. Esslinger, "Real-time observation of fluctuations at the driven-dissipative Dicke phase transition," Proceedings of the National Academy of Sciences **110**, 11763–11767 (2013).

[67] K. Baumann, R. Mottl, F. Brennecke, and T. Esslinger, "Exploring Symmetry Breaking at the Dicke Quantum Phase Transition," Phys. Rev. Lett. **107**, 140402 (2011).

[68] J. Klinder, H. Keßler, M. Wolke, L. Mathey, and A. Hemmerich, "Dynamical phase transition in the open dicke model," Proceedings of the National Academy of Sciences **112**, 3290–3295 (2015).

[69] D. Nagy, G. Kónya, G. Szirmai, and P. Domokos, "Dicke-Model Phase Transition in the Quantum Motion of a Bose-Einstein Condensate in an Optical Cavity," Phys. Rev. Lett. **104**, 130401 (2010).

[70] K. Baumann, C. Guerlin, F. Brennecke, and T. Esslinger, "Dicke quantum phase transition with a superfluid gas in an optical cavity," Nature **464**, 1301–1306 (2010).

[71] S. J. Masson, M. D. Barrett, and S. Parkins, "Cavity QED Engineering of Spin Dynamics and Squeezing in a Spinor Gas," Phys. Rev. Lett. **119**, 213601 (2017).

[72] S. J. Masson, "Many-body cavity QED : the Dicke model, phase transitions, and engineering of multipartite entangled atomic states," (2019), PhD thesis, University of Auckland.

[73] F. Reiter and A. S. Sørensen, "Effective operator formalism for open quantum systems," Phys. Rev. A **85**, 032111 (2012).

[74] M. G. Raymer and I. A. Walmsley, "Temporal modes in quantum optics: then and now," Physica Scripta **95**, 064002 (2020).

[75] K. Vogel and H. Risken, "Determination of quasiprobability distributions in terms of probability distributions for the rotated quadrature phase," Phys. Rev. A **40**, 2847–2849 (1989).

[76] H. P. Yuen and V. W. Chan, "Noise in homodyne and heterodyne detection," Optics Letters **8**, 177–179 (1983).

[77] H. J. Carmichael, *Statistical methods in quantum optics 2: Non-classical fields* (Springer Science & Business Media, 2009).

[78] Z. Hradil, "Quantum-state estimation," Phys. Rev. A **55**, R1561–R1564 (1997).

[79] A. I. Lvovsky, "Iterative maximum-likelihood reconstruction in quantum homodyne tomography," Journal of Optics B: Quantum and Semiclassical Optics **6**, S556–S559 (2004).

[80] A. H. Kiilerich and K. Mølmer, "Input-Output Theory with Quantum Pulses," Phys. Rev. Lett. **123**, 123604 (2019).

[81] C. W. Gardiner, "Driving a quantum system with the output field from another driven quantum system," Phys. Rev. Lett. **70**, 2269–2272 (1993).

[82] H. J. Carmichael, "Quantum trajectory theory for cascaded open systems," Phys. Rev. Lett. **70**, 2273–2276 (1993).

[83] C. S. Muñoz, E. Del Valle, A. G. Tudela, K. Müller, S. Lichtmannecker, M. Kaniber, C. Tejedor, J. Finley, and F. Laussy, "Emitters of N-photon bundles," Nature Photonics **8**, 550 (2014).

[84] E. Waks, E. Diamanti, and Y. Yamamoto, "Generation of photon number states," New Journal of Physics **8**, 4 (2006).

[85] S. Krapick, B. Brecht, H. Herrmann, V. Quiring, and C. Silberhorn, "On-chip generation of photon-triplet states," Optics Express **24**, 2836–2849 (2016).

[86] M. G. Moebius, F. Herrera, S. Griesse-Nascimento, O. Reshef, C. C. Evans, G. G. Guerreschi, A. Aspuru-Guzik, and E. Mazur, "Efficient photon triplet generation in integrated nanophotonic waveguides," Opt. Express **24**, 9932–9954 (2016).

[87] K. A. Fischer, L. Hanschke, J. Wierzbowski, T. Simmet, C. Dory, J. J. Finley, J. Vučković, and K. Müller, "Signatures of two-photon pulses from a quantum two-level system," Nature Physics **13**, 649–654 (2017).

[88] M. Khoshnegar, T. Huber, A. Predojević, D. Dalacu, M. Prilmüller, J. Lapointe, X. Wu, P. Tamarat, B. Lounis, P. Poole, *et al.*, "A solid state source of photon triplets based on quantum dot molecules," Nature Communications **8**, 1–8 (2017).

[89] J. Loredo, C. Antón, B. Reznychenko, P. Hilaire, A. Harouri, C. Millet, H. Ollivier, N. Somaschi, L. De Santis, A. Lemaître, *et al.*, "Generation of non-classical light in a photon-number superposition," Nature Photonics **13**, 803–808 (2019).

[90] K. R. Brown, K. M. Dani, D. M. Stamper-Kurn, and K. B. Whaley, "Deterministic optical Fock-state generation," Phys. Rev. A **67**, 043818 (2003).

[91] A. González-Tudela, V. Paulisch, D. E. Chang, H. J. Kimble, and J. I. Cirac, "Deterministic Generation of Arbitrary Photonic States Assisted by Dissipation," Phys. Rev. Lett. **115**, 163603 (2015).

[92] A. González-Tudela, V. Paulisch, H. J. Kimble, and J. I. Cirac, "Efficient Multiphoton Generation in Waveguide Quantum Electrodynamics," Phys. Rev. Lett. **118**, 213601 (2017).

[93] V. Paulisch, M. Perarnau-Llobet, A. González-Tudela, and J. I. Cirac, "Quantum metrology with one-dimensional superradiant photonic states," Phys. Rev. A **99**, 043807 (2019).

[94] V. S. C. Canela and H. J. Carmichael, "Bright Sub-Poissonian Light through Intrinsic Feedback and External Control," Phys. Rev. Lett. **124**, 063604 (2020).

[95] M. Uria, P. Solano, and C. Hermann-Avigliano, "Deterministic Generation of Large Fock States," Phys. Rev. Lett. **125**, 093603 (2020).

[96] M. Hofheinz, E. Weig, M. Ansmann, R. C. Bialczak, E. Lucero, M. Neeley, A. O'Connell, H. Wang, J. M. Martinis, and A. Cleland, "Generation of Fock states in a superconducting quantum circuit," Nature **454**, 310 (2008).

[97] S. P. Premaratne, F. Wellstood, and B. Palmer, "Microwave photon Fock state generation by stimulated Raman adiabatic passage," Nature Communications **8**, 14148 (2017).

[98] C. Sayrin, I. Dotsenko, X. Zhou, B. Peaudecerf, T. Rybarczyk, S. Gleyzes, P. Rouchon, M. Mirrahimi, H. Amini, M. Brune, J.-M. Raimond, and S. Haroche, "Real-time quantum feedback prepares and stabilizes photon number states," Nature **477**, 73–77 (2011).

[99] A. S. Parkins, P. Marte, P. Zoller, and H. J. Kimble, "Synthesis of arbitrary quantum states via adiabatic transfer of Zeeman coherence," Phys. Rev. Lett. **71**, 3095–3098 (1993).

[100] A. S. Parkins, P. Marte, P. Zoller, O. Carnal, and H. J. Kimble, "Quantum-state mapping between multilevel atoms and cavity light fields," Phys. Rev. A **51**, 1578–1596 (1995).

[101] A. Gogyan, S. Guérin, C. Leroy, and Y. Malakyan, "Deterministic production of n-photon states from a single atom-cavity system," Phys. Rev. A **86**, 063801 (2012).

[102] A. Gogyan and Y. Malakyan, "Deterministic quantum state transfer between remote atoms with photon-number superposition states," Phys. Rev. A **98**, 052304 (2018).

[103] K. M. Birnbaum, A. S. Parkins, and H. J. Kimble, "Cavity QED with multiple hyperfine levels," Phys. Rev. A **74**, 063802 (2006).

[104] Z. Zhiqiang, C. H. Lee, R. Kumar, K. Arnold, S. J. Masson, A. Parkins, and M. Barrett, "Nonequilibrium phase transition in a spin-1 Dicke model," Optica **4**, 424–429 (2017).

[105] S. J. Masson and S. Parkins, "Rapid Production of Many-Body Entanglement in Spin-1 Atoms via Cavity Output Photon Counting," Phys. Rev. Lett. **122**, 103601 (2019).

[106] J. H. Eberly, "Superradiance Revisited," American Journal of Physics **40**, 1374–1383 (1972).

[107] T. Chalopin, C. Bouazza, A. Evrard, V. Makhalov, D. Dreon, J. Dalibard, L. A. Sidorenkov, and S. Nascimbene, "Quantum-enhanced sensing using non-classical spin states of a highly magnetic atom," Nature Communications **9**, 4955 (2018).

[108] C. Law and J. Eberly, "Synthesis of arbitrary superposition of Zeeman states in an atom," Optics Express **2**, 368–371 (1998).

[109] W. Happer, "Optical Pumping," Rev. Mod. Phys. **44**, 169–249 (1972).

[110] S. Kato and T. Aoki, "Strong Coupling between a Trapped Single Atom and an All-Fiber Cavity," Phys. Rev. Lett. **115**, 093603 (2015).

[111] R. Reimann, W. Alt, T. Kampschulte, T. Macha, L. Ratschbacher, N. Thau, S. Yoon, and D. Meschede, "Cavity-Modified Collective Rayleigh Scattering of Two Atoms," Phys. Rev. Lett. **114**, 023601 (2015).

[112] D. M. Greenberger, M. A. Horne, and A. Zeilinger, "Going Beyond Bell's Theorem," arXiv e-prints , arXiv:0712.0921 (2007).

[113] Y. Mu and C. M. Savage, "One-atom lasers," Phys. Rev. A **46**, 5944–5954 (1992).

[114] C. Ginzel, H.-J. Briegel, U. Martini, B.-G. Englert, and A. Schenzle, "Quantum optical master equations: The one-atom laser," Phys. Rev. A **48**, 732–738 (1993).

[115] T. Pellizzari and H. Ritsch, "Preparation of stationary Fock states in a one-atom Raman laser," Phys. Rev. Lett. **72**, 3973–3976 (1994).

[116] P. Horak, K. M. Gheri, and H. Ritsch, "Quantum dynamics of a single-atom cascade laser," Phys. Rev. A **51**, 3257–3266 (1995).

[117] B. Jones, S. Ghose, J. P. Clemens, P. R. Rice, and L. M. Pedrotti, "Photon statistics of a single atom laser," Phys. Rev. A **60**, 3267–3275 (1999).

[118] G. M. Meyer, M. Löffler, and H. Walther, "Spectrum of the ion-trap laser," Phys. Rev. A **56**, R1099–R1102 (1997).

[119] M. Löffler, G. M. Meyer, and H. Walther, "Spectral properties of the one-atom laser," Phys. Rev. A **55**, 3923–3930 (1997).

[120] S. Y. Kilin and T. Karlovich, "Single-atom laser: Coherent and nonclassical effects in the regime of a strong atom-field correlation," Journal of Experimental and Theoretical Physics **95**, 805–819 (2002).

[121] G. M. Meyer and H.-J. Briegel, "Pump-operator treatment of the ion-trap laser," Phys. Rev. A **58**, 3210–3220 (1998).

[122] G. Meyer, H.-J. Briegel, and H. Walther, "Ion-trap laser," Europhysics Letters **37**, 317 (1997).

[123] T. Pellizzari and H. Ritsch, "Photon statistics of the three-level one-atom laser," Journal of Modern Optics **41**, 609–623 (1994).

[124] K. An, J. J. Childs, R. R. Dasari, and M. S. Feld, "Microlaser: A laser with One Atom in an Optical Resonator," Phys. Rev. Lett. **73**, 3375–3378 (1994).

[125] K. An, R. R. Dasari, and M. S. Feld, "Traveling-wave atom–cavity interaction in the single-atom microlaser," Opt. Lett. **22**, 1500–1502 (1997).

[126] J. McKeever, A. Boca, A. D. Boozer, J. R. Buck, and H. J. Kimble, "Experimental realization of a one-atom laser in the regime of strong coupling," Nature **425**, 268 (2003).

[127] G. Rastelli and M. Governale, "Single atom laser in normal-superconductor quantum dots," Phys. Rev. B **100**, 085435 (2019).

[128] T. Aoki, "Private Communication," (2020), Private Communication.

[129] A. D. Boozer, A. Boca, J. R. Buck, J. McKeever, and H. J. Kimble, "Comparison of theory and experiment for a one-atom laser in a regime of strong coupling," Phys. Rev. A **70**, 023814 (2004).

[130] E. Schrödinger, "Die gegenwärtige Situation in der Quantenmechanik," Naturwissenschaften **23**, 823–828 (1935).

[131] C. Song, K. Xu, H. Li, Y.-R. Zhang, X. Zhang, W. Liu, Q. Guo, Z. Wang, W. Ren, J. Hao, *et al.*, "Generation of multicomponent atomic Schrödinger cat states of up to 20 qubits," Science **365**, 574–577 (2019).

[132] A. Ourjoumtsev, H. Jeong, R. Tualle-Brouri, and P. Grangier, "Generation of optical 'Schrödinger cats' from photon number states," Nature **448**, 784 (2007).

[133] J. R. Friedman, V. Patel, W. Chen, S. Tolpygo, and J. E. Lukens, "Quantum superposition of distinct macroscopic states," Nature **406**, 43 (2000).

[134] A. Facon, E.-K. Dietsche, D. Grosso, S. Haroche, J.-M. Raimond, M. Brune, and S. Gleyzes, "A sensitive electrometer based on a Rydberg atom in a Schrödinger-cat state," Nature **535**, 262 (2016).

[135] D. V. Sychev, A. E. Ulanov, A. A. Pushkina, M. W. Richards, I. A. Fedorov, and A. I. Lvovsky, "Enlargement of optical Schrödinger's cat states," Nature Photonics **11**, 379 (2017).

[136] G. S. Thekkadath, B. A. Bell, I. A. Walmsley, and A. I. Lvovsky, "Engineering Schrödinger cat states with a photonic even-parity detector," Quantum **4**, 239 (2020).

[137] N. Shukla, N. Akhtar, and B. C. Sanders, "Quantum tetrachotomous states: Superposition of four coherent states on a line in phase space," Phys. Rev. A **99**, 063813 (2019).

[138] B. M. Garraway, "The Dicke model in quantum optics: Dicke model revisited," Phil. Trans. R. Soc. A **369**, 1137–1155 (2011).

[139] P. Kirton, M. M. Roses, J. Keeling, and E. G. Dalla Torre, "Introduction to the Dicke Model: From Equilibrium to Nonequilibrium, and Vice Versa," Advanced Quantum Technologies **2**, 1970013 (2019).

[140] I. Aedo and L. Lamata, "Analog quantum simulation of generalized Dicke models in trapped ions," Phys. Rev. A **97**, 042317 (2018).

[141] A. Safavi-Naini, R. J. Lewis-Swan, J. G. Bohnet, M. Gärttner, K. A. Gilmore, J. E. Jordan, J. Cohn, J. K. Freericks, A. M. Rey, and J. J. Bollinger, "Verification of a Many-Ion Simulator of the Dicke Model Through Slow Quenches across a Phase Transition," Phys. Rev. Lett. **121**, 040503 (2018).

[142] M. Kitagawa and M. Ueda, "Squeezed spin states," Phys. Rev. A **47**, 5138–5143 (1993).

[143] A. Chia and A. S. Parkins, "Entangled-state cycles of atomic collective-spin states," Phys. Rev. A **77**, 033810 (2008).

[144] J. Sakurai and J. Napolitano, *Modern Quantum Mechanics* (Cambridge University Press, 2017).

[145] S. L. Braunstein and C. M. Caves, "Statistical distance and the geometry of quantum states," Phys. Rev. Lett. **72**, 3439–3443 (1994).

[146] R. Lechner, C. Maier, C. Hempel, P. Jurcevic, B. P. Lanyon, T. Monz, M. Brownnutt, R. Blatt, and C. F. Roos, "Electromagnetically-induced-transparency ground-state cooling of long ion strings," Phys. Rev. A **93**, 053401 (2016).

[147] H. Häffner, C. F. Roos, and R. Blatt, "Quantum computing with trapped ions," Physics Reports **469**, 155–203 (2008).

[148] Y. Zhang, Y.-X. Zhang, and K. Mølmer, "Monte-Carlo simulations of superradiant lasing," New Journal of Physics **20**, 112001 (2018).

[149] N. Shammah, S. Ahmed, N. Lambert, S. De Liberato, and F. Nori, "Open quantum systems with local and collective incoherent processes: Efficient numerical simulations using permutational invariance," Phys. Rev. A **98**, 063815 (2018).

[150] R. Gerritsma, G. Kirchmair, F. Zähringer, E. Solano, R. Blatt, and C. Roos, "Quantum simulation of the Dirac equation," Nature **463**, 68–71 (2010).

[151] M. Joshi, A. Elben, B. Vermersch, T. Brydges, C. Maier, P. Zoller, R. Blatt, and C. Roos, "Quantum information scrambling in a trapped-ion quantum simulator with tunable range interactions," Phys. Rev. Lett. **124**, 240505 (2020).

[152] Z. Zhiqiang, C. Lee, R. Kumar, K. Arnold, S. Masson, A. Grimsmo, A. Parkins, and M. Barrett, "Dicke-model simulation via cavity-assisted Raman transitions," Physical Review A **97**, 043858 (2018).

[153] E. G. Dalla Torre, J. Otterbach, E. Demler, V. Vuletic, and M. D. Lukin, "Dissipative Preparation of Spin Squeezed Atomic Ensembles in a Steady State," Phys. Rev. Lett. **110**, 120402 (2013).

[154] J. Borregaard, E. Davis, G. S. Bentsen, M. H. Schleier-Smith, and A. S. Sørensen, "One-and two-axis squeezing of atomic ensembles in optical cavities," New Journal of Physics **19**, 093021 (2017).

[155] O. Hosten, R. Krishnakumar, N. J. Engelsen, and M. A. Kasevich, "Quantum phase magnification," Science **352**, 1552–1555 (2016).

[156] A. S. Sørensen and K. Mølmer, "Entangling atoms in bad cavities," Phys. Rev. A **66**, 022314 (2002).

[157] Y. Wang, S. Shevate, T. M. Wintermantel, M. Morgado, G. Lochead, and S. Whitlock, "Preparation of hundreds of microscopic atomic ensembles in optical tweezer arrays," npj Quantum Information **6**, 1–5 (2020).

[158] M. E. Kim, T.-H. Chang, B. M. Fields, C.-A. Chen, and C.-L. Hung, "Trapping single atoms on a nanophotonic circuit with configurable tweezer lattices," Nature communications **10**, 1–8 (2019).

[159] T.-A. Isdrailă, C. Kusko, and R. Ionicioiu, "Cyclic permutations for qudits in d dimensions," Scientific Reports **9**, 6337 (2019).

[160] X. Gao, M. Krenn, J. Kysela, and A. Zeilinger, "Arbitrary d-dimensional Pauli X gates of a flying qudit," Phys. Rev. A **99**, 023825 (2019).

[161] F. Schlederer, M. Krenn, R. Fickler, M. Malik, and A. Zeilinger, "Cyclic transformation of orbital angular momentum modes," New Journal of Physics **18**, 043019 (2016).

[162] C.-Y. Jin, R. Johne, M. Y. Swinkels, T. B. Hoang, L. Midolo, P. J. Van Veldhoven, and A. Fiore, "Ultrafast non-local control of spontaneous emission," Nature Nanotechnology **9**, 886 (2014).

[163] J.-P. W. MacLean, J. M. Donohue, and K. J. Resch, "Direct Characterization of Ultrafast Energy-Time Entangled Photon Pairs," Phys. Rev. Lett. **120**, 053601 (2018).

[164] Y. Mei, Y. Zhou, S. Zhang, J. Li, K. Liao, H. Yan, S.-L. Zhu, and S. Du, "Einstein-Podolsky-Rosen Energy-Time Entanglement of Narrow-Band Biphotons," Phys. Rev. Lett. **124**, 010509 (2020).

[165] N. V. Vitanov, A. A. Rangelov, B. W. Shore, and K. Bergmann, "Stimulated Raman adiabatic passage in physics, chemistry, and beyond," Rev. Mod. Phys. **89**, 015006 (2017).

[166] D. D'Alessandro, *Introduction to Quantum Control and Dynamics*, Chapman & Hall/CRC Applied Mathematics & Nonlinear Science (CRC Press, 2007).

[167] K. Murr, S. Nußmann, T. Puppe, M. Hijlkema, B. Weber, S. C. Webster, A. Kuhn, and G. Rempe, "Three-dimensional cavity cooling and trapping in an optical lattice," Phys. Rev. A **73**, 063415 (2006).